MEASUREMENT OF POLARIZED PROTON - PROTON ELASTIC SCATTERING AT THE RELATIVISTIC HEAVY ION COLLIDER (RHIC)

by

Ivan Koralt
B.S. May 2005, University of Belgrade, Serbia
M.S. May 2009, Old Dominion University

A Dissertation Submitted to the Faculty of
Old Dominion University in Partial Fulfillment of the
Requirements for the Degree of

DOCTOR OF PHILOSOPHY

PHYSICS

OLD DOMINION UNIVERSITY
December 2013

Approved by:

_____
Stephen Bültmann (Director)

_____
Leposava Vušković (Member)

_____
Gail Dodge (Member)

_____
Anatoly Radyushkin (Member)

_____
Tal Ezer (Member)

ABSTRACT

MEASUREMENT OF POLARIZED PROTON - PROTON ELASTIC SCATTERING AT THE RELATIVISTIC HEAVY ION COLLIDER (RHIC)

Ivan Koralt
Old Dominion University, 2013
Director: Dr. Stephen Bültmann

Elastic proton-proton (pp) scattering is one of the most fundamental processes in nature and yet, it is one of the most difficult to describe. There are two interactions involved in this process: electromagnetic (Coulomb) and hadronic (strong) interactions. Underlying exchange mechanisms of these two interactions are the virtual photon and the *Pomeron* exchange, respectively. The difficulty of elastic pp scattering arises from the fact that the nature of the *Pomeron* and its exchange are not well understood and need a theoretical approach, which is still under development.

At the Relativistic Heavy Ion Collider (RHIC) at Brookhaven National Lab (BNL) we are studying the hadronic interaction via the dynamics of high-energy pp collisions using the Solenoidal Tracker At RHIC (STAR) detector. The "Physics With Tagged Forward Protons At STAR" experiment, formerly known as the "$pp2pp$" experiment, is a part of STAR and it successfully conducted measurements of elastic scattering observables by the use of its forward particle detectors, known as Roman pots.

In this dissertation I present the measurement of polarized pp elastic scattering at RHIC. I describe the "$pp2pp$ at STAR" experiment focusing on elastic scattering observables from the data taken in Run9. I report the result of the experimental slope parameter B of the diffractive peak of the elastic cross-section at the center-of-mass energy $\sqrt{s} = 200$ GeV in the four-momentum transfer squared t range $0.006 \leq |t| \leq 0.02$ (GeV/c)^2. I also present data analysis techniques and Monte Carlo simulations developed for the analysis and improvement of the detector performance, correction of the recorded experimental data and an estimate of systematic errors of this measurement.

ACKNOWLEDGEMENTS

I would like to thank my dissertation advisor and my mentor, Dr. Stephen L. Bültmann without whom this research work would not have been possible. I am grateful for his patient guidance, continuous support and help through the years of my graduate school. Stephen, thank you for everything you have ever done for me. Thank you for all your encouragement and for always being very understanding and willing to help. I consider you my real true friend.

I would like to express my deepest gratitude to two wonderful people who tremendously helped me, guided me, and supported me from the first day of my arrival to the United States of America: Dr. Leposava Vušković and Dr. Svetozar Popović. Thank you for always being there for me and for not only teaching me to be a successful scientist, but a better person as well. You are truly my second parents.

My special thanks goes to my fellow graduate student and great friend Dr. Donika Plyku, for persuading me to join "*pp*2*pp* at STAR" team at ODU, for her help in gaining my knowledge on the matter and for all the constructive discussions during our time as graduate students at "*pp*2*pp* at STAR" experiment.

This work could not have been possible without all the help and support from the entire "*pp*2*pp* at STAR" team: Dr. Włodzimierz Guryn, Dr. Kin Yip, Dr. Igor Alekseev, Dr. Dimitri Svirida, Dr. Jeong-Hun Lee, Dr. Leszek Adamczyk, Dr. Janusz Chwastowski, Tomek Obrebski, and Rafał Sikora. My special gratitude goes to Dr. Kin Yip for all the knowledge he unselfishly shared, especially for the help with data analysis and his guidance in the computational part of this work.

I would like to express my gratitude to Dr. Gail Dodge, Dr. Anatoly Radyushkin, Dr. Leposava Vušković and Dr. Tal Ezer for taking part in this work as my graduate committee.

I am thankful to faculty and staff of ODU Physics Department for all their help and support through all the years of my graduate school.

Whatever words of thankfulness I try to use, it would not be enough to express my deepest and most sincere gratitude to the ones closest to me, my family. Thank you for all your unconditional love and support. I dedicate this dissertation to you.

To my parents

TABLE OF CONTENTS

LIST OF TABLES

LIST OF FIGURES

CHAPTER 1

INTRODUCTION

Elastic proton-proton scattering is one of the most fundamental processes in nature and yet, it is one of the most difficult to describe. This difficulty arises from the fact that the coupling constant (α) of Quantum Chromodynamics (QCD) becomes large in the low four-momentum transfer squared $|t|$ region, which makes this process intrinsically non-perturbative. Consequently, the straight forward calculations from perturbative Quantum Chromodynamics (pQCD) become non-applicable for the description of elastic proton-proton scattering at low-$|t|$. Instead, in order to study the dynamics of the low-$|t|$ scattering process in pp elastic collisions, an examination of our understanding of the underlying interactions and the associated exchange mechanisms is needed.

There are two fundamental interactions involved in elastic pp scattering, electromagnetic (Coulomb) and hadronic (strong). While the former can be precisely described by Quantum Electrodynamics (QED), the latter is not well understood and needs a non-pQCD theoretical approach, which is still under development. Theoretical models, available to date, are used to describe the exchange mechanism by approaches that are more or less based upon Regge theory and/or an eikonal formalism. These models put great effort in the attempt to connect Regge and QCD concepts. In Chapter 2 we will discuss some of these models. Also, we will give a description of the kinematics of the diffractive processes, focusing on elastic scattering. Furthermore, Chapter 2 discusses spin-independent observables: total cross-section σ_{tot}, exponential slope parameter B and parameter ρ, in both pp and $p\bar{p}$ scattering experiments. Measurement of these spin-averaged observables at various center of mass system (cms) energies is important in understanding exchange mechanisms that dominate in the diffractive processes at low and high energies, as well as in the description and understanding of the features observed in the behavior of total elastic and differential cross-sections at different energies.

Protons and their interactions can be studied in particle colliders or in fixed target experiments. Facilities, such as the Large Hadron Collider (LHC) at CERN or the Relativistic Heavy Ion Colider (RHIC) at Brookhaven National Lab (BNL)

have experiments that focus on high-energy proton collisions for the study of the dynamics of the scattering processes in both polarized and unpolarized proton beam collisions. Previous pp and $p\bar{p}$ scattering experiments conducted at CERN and FNAL, provided differential and total cross-sections at different cms energies and $|t|$-ranges. The total cross-sections of both pp and $p\bar{p}$ measurements reach minimum values at $\sqrt{s} = 10$ GeV, and show a slow rise towards higher energies. Regge theory, for example, describes this behavior by postulating a *Reggeon* with quantum numbers of the vacuum, in Pomeranchuk theorem called the *Pomeron*. The *Pomeron* is considered a dynamical system, rather than a particle, often described in pQCD as a color singlet combination of two or more gluons. It has mass, no spin and no electric or color charge. Although the *Pomeron* phenomenology is well described in Regge theory, its exact nature remains obscure. Therefore, more measurements are needed in order to guide the theoretical research.

The highest cms energies in pp collisions are achieved by the TOTEM experiment at LHC (CERN), reaching to date 8 TeV with unpolarized beams, and by the Intersecting Storage Ring (ISR) experiments, also at CERN, reaching 20 GeV by colliding polarized beams. The Relativistic Heavy Ion Collider (RHIC), on the other hand, has the unique capability of colliding identical polarized species, like protons, in a previously unexplored cms energy range: $50 \leq \sqrt{s} \leq 500$ GeV. This gives the unique opportunity to study both dynamics and the spin-dependence of pp scattering in previously inaccessible energy and four-momentum transfer squared ranges. The "Physics With Tagged Forward Protons At STAR" experiment at RHIC, formerly known as the "$pp2pp$" experiment is dedicated to the spin-dependent and spin-independent hadronic phenomena at these energies and low-$|t|$ range. Since the beginning of its operation, in the time span of several runs, it successfully conducted the measurements of the spin-dependent and spin-independent observables by the use of its forward detectors, known as Roman pots. Roman pots are cylindrical vessels that house Si micro-strip detectors used for particle detection. These cylindrical vessels are inserted into the beam pipeline to bring silicon detectors as close as possible to the outgoing proton beam, without disturbing the accelerator vacuum. Chapter 3 is dedicated to all experimental aspects of the "Physics With Tagged Forward Protons At STAR".

Chapter 4 is dedicated to the latest data collection period in 2009 (Run9), with transversely polarized proton beams collisions at 200 GeV cms energy. In a four

day dedicated run during the 2009 data taking period, a sample of 33 million elastic triggers was recorded. We present beam tune and overall accelerator performance during this four day dedicated running period.

Chapters 5, 6 and 7 are the core of this work. Chapter 5 covers the detailed description of the procedure followed and the selection criteria used in the extraction of elastic events out of the 33 million elastic triggers, recorded in 2009. The extraction of the nuclear slope parameter B in a combined fit to the differential cross-section, which is the main result of this work, is reported in Chapter 7 and the study of all systematical effects observed in recorded data from 2009 is presented in Chapters 6 and 8. For corrections of certain systematic effects, like a trigger bias, Monte Carlo simulations using the GEANT4 toolkit were developed. We elaborate on both systematic effects and Monte Carlo simulations in detail, also in Chapter 6. Finally, the result of the experimental slope parameter B of the diffractive peak of the elastic cross-section in the t range $0.006 \leq |t| \leq 0.02$ $(\mathrm{GeV/c})^2$ and $\sqrt{s} = 200$ GeV obtained from RHIC Run9 is presented in Chapter 9.

CHAPTER 2

THEORETICAL BACKGROUND

2.1 HADRONIC PROCESSES

Hadronic processes are classified in two distinct classes: *soft processes* and *hard processes* [14].

- *Soft processes* are characterized by one energy scale which is of the order of the hadron size R ($\sim$1 fm). This is the only scale of the process. In general, these processes are characterized by a small momentum transfer ($|t| \sim 1/R^2 \sim$ few hundred MeV^2), cross-section t-dependences of an exponential nature ($d\sigma/dt \sim e^{-R^2|t|}$) and a high suppression of large-$|t|$ events.
  Typical examples of *soft processes* are elastic hadron-hadron scattering and diffractive dissociation.
  The presence of a large length scale (R) makes these processes intrinsically non-perturbative and from the theoretical point of view, perturbative quantum chromodynamics (pQCD) is inadequate for their description. Instead, Reggie theory [15], [16], [17], is used. According to this theory, soft hadronic processes at high energies are universally dominated by the exchange of an enigmatic object, the *Pomeron*.

- *Hard processes* are characterized by two or more energy scales, one of the order of the hadron size R ($\sim$1 fm) and another "*hard*" energy scale with large momentum transfer (of the same order as this scale, $\gtrsim 1$ GeV^2). Typical cross-section dependences on the momentum transfer in *hard processes* are power-like, modulo logarithms.
  The examples of *hard processes* are deep inelastic scattering (the momentum transfer is q^2, the virtuality of the exchanged photon or vector boson) and large-p_T jet production (the momentum squared is $-p_T^2$).
  The high q^2 allows usage of perturbative QCD. However, a part of the process is still non-perturbative in nature and this component is embodied in the

quark-gluon distribution (or fragmentation) functions of hadrons. The so-called "*factorization theorems*" [18] ensure that perturbative and non-perturbative parts are well separated from each other. The latter is universal: it can be extracted from one process and used to predict another one.

In recent years, the interest in finding and investigating hadronic diffractive processes that have both *soft* and *hard* properties at the same time arose, because these processes open up the possibility of studying diffraction (to some extent) in a perturbative framework. In other words, these processes open the possibility for investigating the QCD nature of the *Pomeron*, and more importantly, for translation of Reggie theory (phenomenology of soft phenomena) into the language of QCD, the theory of strong interactions.

2.1.1 HADRONIC DIFFRACTIVE PROCESSES

A general definition of hadronic diffractive processes is formulated as follows:

- *A reaction in which no quantum numbers (other than those of the vacuum) are exchanged between the colliding particles is, at high energies, a diffractive reaction.*

In other words, *diffraction* is the process, asymptotical in nature (falls asymptotically), that takes place whenever the diffused and incident particles have the same quantum numbers.

In the definition above, no quantum number exchange is only necessary, but not a sufficient condition. However, the main advantage of this is because it is simple and general enough to cover all cases:

- *elastic scattering*, when exactly the same incident particles emerge after the collision, Fig. 1(a).

$$1 + 2 \to 1' + 2' \tag{1}$$

- *single diffraction*, when one of the incident particles emerges out of the collision unchanged while the other one gives rise to a final state of particles with the same quantum numbers, Fig. 1(b).

$$1 + 2 \to 1' + X_2 \tag{2}$$

- *double diffraction*, when each incident particle gives rise to a bunch of final particles with exactly the same quantum numbers of the two initial particles, Fig. 1(c).

$$1 + 2 \to X_1 + X_2 \tag{3}$$

An operational definition of the hadronic diffraction processes, equivalent to the one above, is:

- *A diffractive process is characterized by large, non exponentially suppressed, rapidity gap in the final state.*

The requirement of having a large rapidity gap in the final state (a large angular region in which no outgoing particles are detected) is again, not a sufficient condition for characterizing diffraction. There is another condition that needs to be added to this definition and that is a non exponential suppression of the rapidity gaps in the final state. In this way, contamination with non-diffractive events is avoided. True diffraction can be distinguished only asymptotically from non-diffraction contributions, as it is known that the latter decreases with energy.

The theoretical framework for describing diffraction is Reggie theory. This theory provides a bridge between the two definitions from above. It describes hadronic processes at high energies in terms of exchanging "objects" (not particles) called *Reggeons*.

The *Reggeon* with quantum numbers of the vacuum, which dominates asymptotically, is called *Pomeron*. In Regge theory, the exchange of other objects with vacuum quantum numbers is suppressed at high energies. Therefore, the diffractive processes are dominated by the exchange of the *Pomeron*. In the language of Regge theory, "*diffraction*" is equivalent to *Pomeron exchange*.

2.1.2 KINEMATICS

Elastic scattering, Eq. (1) is a special case of a *two body exclusive scattering* process which is given by:

$$1 + 2 \to 3 + 4 \quad (s - channel, \text{Fig. } 2(\text{a})). \tag{4}$$

In elastic scattering, two particles remain unaltered, but they have a different kinematic configuration in the final state, Eq. (1). This type of scattering can be

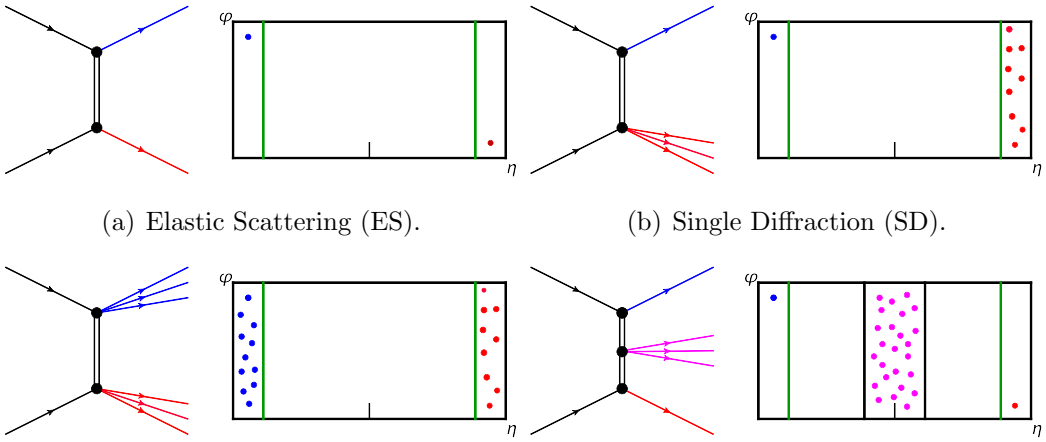

(a) Elastic Scattering (ES). (b) Single Diffraction (SD).

(c) Double Diffraction (DD). (d) Double *Pomeron* Exchange (DPE).

FIG. 1. Diffractive process classes. Left: a Feynman-like diagram showing the nature of the process, with *Pomeron* exchange (the double lines) as an effective description of the diffraction phenomena. Single external lines denote protons, the triple outgoing lines represent proton dissociation. Right: a sample hit map in the pseudorapidity (η) vs. azimuthal angle (φ) space.

described by two independent variables, usually chosen among the three *Mandelstam variables*.

Mandelstam variables are used to describe the interaction of the incoming particles in high-energy scattering processes and to characterize the kinematics of the scattering.

Consider the elastic scattering of two protons in the center of mass (*cms*) system shown in Fig. 2:

Mandelstam variables are represented as:

$$\begin{aligned} s &= (p_1 + p_2)^2 = (p_3 + p_4)^2 \\ t &= (p_1 - p_3)^2 = (p_2 - p_4)^2 \\ u &= (p_1 - p_4)^2 = (p_2 - p_3)^2, \end{aligned} \tag{5}$$

where p_1 and p_2 are the four-momenta of the the two colliding protons, and p_3 and p_4 are the four-momenta of the the two scattered protons, respectively.

Mandelstam variables satisfy the identity:

$$s + t + u = \sum_{i=1}^{4} m_i^2 \tag{6}$$

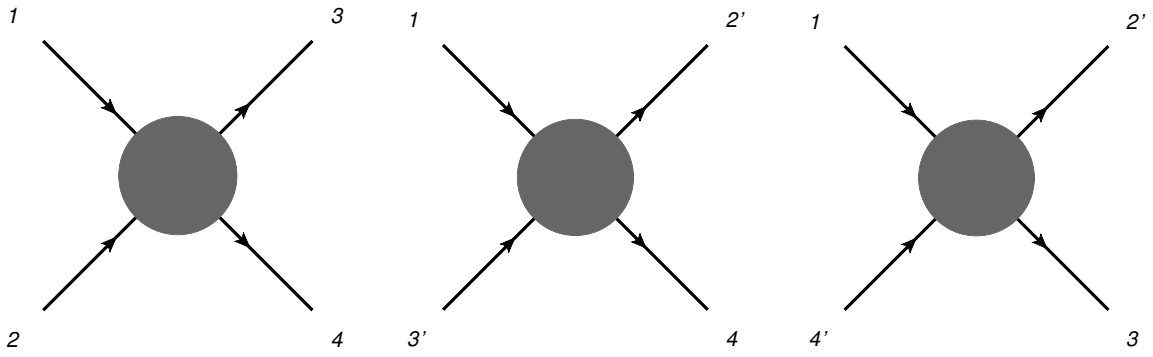

(a) s-channel. (b) t-channel. (c) u-channel.

FIG. 2. Two-body exclusive scattering.

which is easily derived from definitions in Eq. (5) together with energy-momentum conservation: $p_1 + p_2 = p_3 + p_4$, which leads to the conclusion that only two of them are independent. In general, s and t are taken as the two independent *Mandelstam variables*.

In proton-proton elastic scattering, two incoming protons collide and remain intact after the collision. In the center of mass system, by definition we have (assuming particles 1 and 2 are traveling along the z-axis with equal but opposite momenta p_1 and p_2):

$$\boldsymbol{p_1} + \boldsymbol{p_2} = 0, \tag{7}$$

where four-momenta of the particles can be written as:

$$\begin{aligned} p_1 &= (E_1, \boldsymbol{p}) = (E_1, 0, 0, p_z) \\ p_2 &= (E_2, -\boldsymbol{p}) = (E_2, 0, 0, -p_z) \\ p_3 &= (E_3, -\boldsymbol{p'}) = (E_3, \boldsymbol{p}_\perp, p'_z) \\ p_4 &= (E_4, -\boldsymbol{p'}) = (E_4, -\boldsymbol{p}_\perp, -p'_z). \end{aligned} \tag{8}$$

Here p' is the three-momentum of the scattering particles, $p_\perp = |\boldsymbol{p'}| \sin\theta$ is the transverse two-vector momentum, $p_z = |\boldsymbol{p'}| \sin\theta$ and θ is the scattering angle in the *cms* coordinate system. The energies E_1, E_2, E_3, E_4 and momentums p and p' can be expressed in terms of the *Mandelstam variable* $s = (p_1 + p_2)^2$, in the high-energy limit ($s \to \infty$), as:

$$E_1, E_2, E_3, E_4 \simeq \frac{\sqrt{s}}{2} \tag{9}$$

and

$$|\boldsymbol{p}|, |\boldsymbol{p'}| \simeq \frac{\sqrt{s}}{2}. \tag{10}$$

In proton-proton elastic scattering all particles have the same mass, m and the relations between *cms* variables and the *Mandelstam invariants* become much simpler. With respect to the conservation of the four-momentum, the *Mandelstam variables* can be expressed (in *cms* system) as:

$$\begin{aligned} s &= (p_1 + p_2)^2 = 4(p^2 + m^2) \\ t &= (p_1 - p_3)^2 = -2p^2(1 - \sin\theta) = -4p^2 \sin^2(\theta/2). \end{aligned} \tag{11}$$

For very-forward scattering, the scattering angle θ is very small. Therefore, one can approximate the four-momentum transfer squared t as:

$$t \approx -p^2\theta^2. \tag{12}$$

Mandelstam variables are Lorentz scalars because they are dot products of four-vectors. In the case of $s \to \infty$ or $s >> m^2$ (like in this experiment), the scattering angle in the *cms* system θ can be expressed as:

$$\cos\ \theta = 1 + \frac{2t}{s}. \tag{13}$$

Another frequently used kinematic variable is the *rapidity*. This variable is defined (for a particle of energy E and momentum component along z-axis) as:

$$y = \frac{1}{2}\ \ln\ \frac{E + p_z}{E - p_z}. \tag{14}$$

For massless particles ($E \simeq |\boldsymbol{p}|$) *rapidity* is directly related to the scattering angle θ (specifying the direction of motion with respect to the $z - axis$):

$$y = \frac{1}{2}\ \ln\ \frac{1 + \cos\ \theta}{1 - \cos\ \theta} = -\ln\ \tan\frac{\theta}{2}, \tag{15}$$

which is exactly the definition of *pseudorapidity*:

$$\eta \equiv y|_{m=0} = -\ln\ \tan\frac{\theta}{2}. \tag{16}$$

The values of the *pseudorapidity* for the cases of elastic scattering, single diffraction and double diffraction processes is shown in Fig. 1.

2.1.3 SCATTERING AMPLITUDE $f(\theta,\ s)$, DIFFERENTIAL CROSS-SECTION $\frac{d\sigma}{dt}$ AND FORWARD SCATTERING PARAMETERS B, ρ, σ_{tot}

The *differential cross-section* is equal to the square of the scattering amplitude $f(\theta, s)$:

$$\frac{d\sigma}{d\Omega} = |f(\theta, s)|^2, \tag{17}$$

where $d\Omega = d\varphi d(\cos\theta) = 2\pi d(\cos\theta)$ is the element of the solid angle of the scattered particle, independent of the azimuthal angle. By using this relation, the differential cross-section can be expressed in terms of the Mandelstam variable t as:

$$\frac{d\sigma}{dt} = \frac{d\Omega}{dt}\frac{d\sigma}{d\Omega} = 2\pi\frac{d\cos\theta}{dt}\frac{d\sigma}{d\Omega}. \tag{18}$$

By differentiating Eq. (11), with respect to $\sin\theta$ we get:

$$\frac{dt}{d\cos\theta} = 2p^2, \tag{19}$$

and therefore, with respect to Eq. (17),

$$\frac{d\sigma}{dt} = \frac{\pi}{p^2}\frac{d\sigma}{d\Omega} = \frac{\pi}{p^2}|f(\theta, s)|^2. \tag{20}$$

With respect to the optical theorem [19], an invariant scattering amplitude is now introduced:

$$F \equiv \frac{\sqrt{\pi}}{p} f(\theta, s). \tag{21}$$

The optical theorem relates the total cross-section to the imaginary part of the elastic scattering amplitude $f_{el}(t = 0)$ in the case of very forward scattering as:

$$\sigma_{tot} = \frac{4\pi}{p}\mathrm{Im}f_{el}\ (t = 0), \tag{22}$$

where p is the center of mass three momentum of the incident particle. The optical theorem provides a relation between the total cross-section σ_{tot}, the forward differential cross-section, $d\sigma/dt\ (t = 0)$ and the ratio between the real to the imaginary part of the scattering amplitude at $t = 0$, ρ. The forward differential cross-section is given by:

$$\frac{d\sigma}{d\Omega}\Big|_{\theta=0} = |f(t = 0)|^2 = [\mathrm{Re}f(t = 0)]^2 + [\mathrm{Im}f(t = 0)]^2 \tag{23}$$

and the real to the imaginary part of the scattering amplitude, $\rho(t=0)$, as:

$$\rho = \frac{\mathrm{Re}f(s,t=0)}{\mathrm{Im}f(s,t=0)}. \tag{24}$$

Therefore, using the optical theorem, Eq. (22), Eq. (23) and Eq. (20), the forward differential cross-section can be expressed as:

$$\frac{d\sigma}{d\Omega}\Big|_{\theta=0} = \Big(\frac{\sigma_{tot}^2}{16\pi}\Big)(1+\rho^2). \tag{25}$$

Combining equations above, we get a relation between the forward differential cross-section, parameter ρ and total cross-section:

$$\frac{d\sigma}{dt}\Big|_{t=0} = \Big(\frac{\sigma_{tot}^2}{16\pi}\Big)(1+\rho^2) = |F|^2. \tag{26}$$

where $\sigma_{tot}(s) = 4\sqrt{\pi}\mathrm{Im}F(s,t=0)$.

In order to express the differential elastic pp cross-section in terms of the forward scattering parameters σ_{tot}, ρ and B, both contributions from electromagnetic (Coulomb) and hadronic (nuclear) interactions have to be considered. The differential elastic cross-section is related to the invariant scattering amplitudes for the hadronic and the Coulomb interactions according to:

$$\frac{d\sigma_{el}}{dt} = |F_c + F_n|^2. \tag{27}$$

However, due to the fact that F_c and F_n may have a relative phase and if we limit ourselves to the case of elastic scattering, the differential cross-section can be formally represented as:

$$\frac{d\sigma_{el}}{dt} = \frac{1}{16\pi s^2}\big|F_c e^{\pm i\alpha\phi(t)} + F_n\big|^2, \tag{28}$$

where $\pm$ depends on whether we have pp or $p\bar{p}$ collisions, respectively.

F_c can be precisely determined by using Quantum Electrodynamics (QED). From QED, [20],

$$F_c(s,t) = -\sqrt{\pi}sG_E^2(t)\frac{2\alpha}{|t|}, \tag{29}$$

where $G_E(t)$ is the *electromagnetic form factor* of the proton and is equal to

$$G_E(t) = \frac{1}{1+\frac{|t|^2}{\Lambda^2}}, \tag{30}$$

with $\Lambda^2 = 0.71$ GeV^2.

Starting from the relativistic corrected Rutherford scattering cross-section,

$$\frac{d\sigma_c}{d\Omega_{cm}} = \left|\frac{-\alpha G_E^2(t)}{2p\sin^2\frac{\theta}{2}}\right|, \tag{31}$$

with $\alpha \approx \frac{1}{137}$ as the *fine structure constant*, and using Eq. (30) together with the differential cross-section for Coulomb interaction in the form, Eq. (20),

$$\frac{d\sigma_c}{dt} = \pi \left| -G_E^2(t)\frac{2\alpha}{|t|} \right|. \tag{32}$$

On the other hand, there is no exact theoretical approach for the *invariant scattering amplitude of the hadronic interaction, F_n*. However, experiments have shown that at low $|t|$, this amplitude can be well approximated by an exponential function [21]. It can be extracted by using the ratio of the real-to-imaginary parts of the scattering amplitude at $t = 0$, Eq. (24) and the optical theorem, Eq. (22), [19] and it is given in it's empirical form as:

$$F_n = \frac{s(\rho + i)\sigma_{tot} e^{\frac{-B|t|}{2}}}{4\sqrt{\pi}}. \tag{33}$$

By combining Eqs. 29, 33 and 28 the differential elastic cross-section at small-$|t|$ can be expressed in terms of the forward scattering parameters (σ_{tot}, ρ, B) as:

$$\frac{d\sigma_{el}}{dt} = 4\pi\alpha_{em}^2 \frac{G_E^4(t)}{|t|^2} - \alpha_{em}\frac{G_E^2(t)}{|t|}\sigma_{tot}e^{-\frac{Bt}{2}}(\rho + \alpha_{em}\phi) + \frac{1+\rho^2}{16\pi}\sigma_{tot}^2 e^{-B|t|}. \tag{34}$$

Equation 34 represents the dependence of the differential elastic cross-section on the four momentum transfer squared, t. This dependence can be divided into three regions: Coulomb, Coulomb-Nuclear Interference and hadronic region. The Coulomb term dominates in the low-$|t|$ region. In this region, $d\sigma_{el}/dt$ is dominated by a $1/|t|^2$ dependence. As t increases, the relative contribution of the interference term increases. The interference term is proportional to $(\rho + \alpha_{em}\phi)$. The helicity independent Coulomb phase $\delta = \alpha_{em}\phi$ is approximately [22]:

$$\delta = \alpha_{em}\phi = \alpha_{em}\left(\ln\frac{2}{|t|(B + 8/\Lambda^2)} - \gamma\right), \tag{35}$$

where the so called slope-B is the logarithmic derivative of the differential cross-section at $t = 0$ and $\gamma = 0.5772$ is Euler's constant. Finally, in the higher-$|t|$ region, the hadronic term dominates and the elastic differential cross-section falls exponentially with $|t|$.

The low-$|t|$ region, the region where the Coulomb amplitude dominates, is the region where a partial total cross-section in t can be measured by comparing to QED calculation. Total cross-sections are measured both at fixed-target accelerators

and colliders. In the case of fixed-target accelerators, they are measured with the transmission technique where they are determined from the attenuation of the beam after it strikes the target. On the other hand, in colliders, there are two approaches to the measurement of the total cross-section: *Luminosity-independent* and *Luminosity-dependent approach*.

The total cross-section is related to the observed number of elastic and inelastic events via Eq. (36):

$$N_{el} + N_{in} = \mathcal{L}\sigma_{tot}, \tag{36}$$

where N_{el} and N_{in} are numbers of elastic and inelastic events, respectfully. The luminosity $\mathcal{L}$ is often not very well known. Therefore Eq. (36) can not be used for the extraction of the total cross-section σ_{tot}. Instead, it can be related to the elastic scattering rate at $t = 0$ by the use of Eq. (26) via:

$$\left.\frac{dN_{el}}{dt}\right|_{t=0} = \mathcal{L}\left.\frac{d\sigma_{el}}{dt}\right|_{t=0} = \mathcal{L}\frac{1+\rho^2}{16\pi}\sigma_{tot}^2, \tag{37}$$

where ρ is given by Eq. (24) and is small at high energies and does not need to be precisely known. By the use of Eq. (36) in Eq. (37) and eliminating $\mathcal{L}$ we get a luminosity independent formula for the extraction of σ_{tot}:

$$\sigma_{tot} = \frac{16\pi}{1+\rho^2}\frac{(dN_{el}/dt)|_{t=0}}{N_{el}+N_{in}}, \tag{38}$$

where $(dN_{el}/dt)|_{t=0}$ is extrapolated from the measured t-region of nuclear scattering given by:

$$\frac{dN_{el}}{dt} = \left.\frac{dN_{el}}{dt}\right|_{t=0} e^{-Bt}. \tag{39}$$

In the luminosity dependent method, there is another very important factor, the acceptance or efficiency factor, μ, related to the design of the experimental apparatus. Hence, the scattering rate, Eq. (37) becomes:

$$\left.\frac{dN_{el}}{dt}\right|_{t=0} = \mathcal{L}\mu\left.\frac{d\sigma_{el}}{dt}\right|_{t=0}. \tag{40}$$

This method requires measuring scattering in the very-forward region, which is experimentally very challenging. Therefore, the Roman Pot technique (see Section 3) has been very significant for these measurements in the very-forward direction.

The region where Coulomb and hadronic amplitudes have comparable magnitudes

(CNI region, $t \sim 10^{-3}$ GeV^2) is where the measurement of the ρ parameter can be performed. The Coulomb and hadronic amplitudes are equal when:

$$-t_{max} = \sqrt{3}\frac{8\pi\alpha}{\sigma_{tot}}. \tag{41}$$

At $\sqrt{s} = 200$ GeV and pp cross-section of $\sigma_{tot} = 60$ mb, $-t_{max} \approx -2{\cdot}10^{-3}$ GeV$^2/c^2$ and corresponds to a scattering angle of 0.54 mrad. The measurement of the ρ-parameter is related to the real part of the forward scattering amplitude. It is specially related to the energy dependence of the total cross-section which is presented later [5].

Lastly, the t-region where the hadronic amplitude dominates is the region suitable for the extraction of the nuclear slope parameter B in a combined fit to the differential cross-section.

2.2 REGGE THEORY AND THE *POMERON*

In quantum physics, *Regge theory* [23] is the study of the analytic properties of scattering as a function of angular momentum which is not restricted to be an integer value, but instead, it is allowed to take any continuous complex value. Mathematically, it is possible to treat angular momentum as a continuous complex variable and interactions in terms of partial wave amplitudes (an expansion in terms of analytical functions of continuous complex angular momentum variable). Such amplitudes exhibit simple poles, often called *Regge poles*, in the complex angular momentum plane at positions that correspond to particles of definite angular momentum, tracing out a *Regge trajectory*, which may lead to *s-channel* resonances. Each pole contributes to the scattering amplitude a term which behaves asymptotically as:

$$A(s,t) \sim s^{\alpha(t)} \ (s \to \infty,\ t - \text{fixed}). \tag{42}$$

Thus the leading *singularity* (i.e. with the largest real part) in the *t-channel* determines the asymptotic behavior of the scattering amplitude in the *s-channel*. Therefore, one very important application of *Regge theory* is that *Regge poles* in the *t-channel* can be used to predict the form of the amplitude in a high energy, low $|t|$, two-body *s-channel* ractions. When applied to the strong interaction, *Regge theory* provides the only general explanation of the energy behavior of two-body inelastic cross-sections.

Regge theory belongs to the class of so-called *t-channel* models. These models

describe hadronic processes in terms of the *t-channel* exchange of "something". In the simplest version of *t-channel* models, this "something" is a (virtual) *particle*. Due to this, nuclear forces are usually attributed to the exchange of mesons (π, ρ etc.), analogous to the exchange of virtual photons in electro-magnetic interactions of two electrons. However, this becomes inapplicable at high energies due to the violation of the *Froissart-Martin* bound, i.e. violation of unitarity. *Regge theory* overcomes this problem by preserving the idea of the *t-channel* exchange, but describing the strong force not as the exchange of *particles* with definite spin, but rather to the exchange of a *Regge trajectory*. The large *s-limit* of hadronic processes is determined by the exchange of one or more *Regge trajectories* in the *t-channel*. In terms of particle physics language, *Regge trajectories* are often called *Reggeons*.

Exchanging *Reggeons* instead of *particles* leads to scattering amplitudes of the type in Eq. (42), but without violation of the *Froissart-Martin* bound when $\alpha(0) < 1$.

Pomeranchuk (1958) [24] predicted that total cross-sections would approach a constant asymptotic limit. The *Regge trajectory* whose exchange ensures this behavior became known as the *Pomeron*. It is generally supposed that in terms of QCD, the *Pomeron* represents multi-gluon exchange. This very complicated *Regge trajectory* is found to be responsible for the interactions at high energies and small $|t|$.

2.2.1 REGGE TRAJECTORY

In a two-body scattering process in the *t-channel*, $1 + \bar{2} \to \bar{3} + 4$, the scattering amplitude, as a function of s and t, can be expanded in terms of *Legendre polynomials*, $P_l(\sin\theta)$ as:

$$A_{1+\bar{2}\to\bar{3}+4}(s,t) = \sum_{l=0}^{\infty}(2l+1)A_l(s)P_l(\sin\theta), \tag{43}$$

where $A_l(s)$ are the partial wave amplitudes. Using Eq. (13), at low-$|t|$ the previous equation becomes:

$$A_{1+\bar{2}\to\bar{3}+4}(s,t) = \sum_{l=0}^{\infty}(2l+1)A_l(s)P_l(1+\frac{2t}{s}). \tag{44}$$

The corresponding equation in the *s-channel*, $1 + 2 \to 3 + 4$, obtained by

interchanging s and t is given by:

$$A_{1+2\to 3+4}(s,t) = \sum_{l=0}^{\infty}(2l+1)A_l(t)P_l(1+\frac{2s}{t}). \tag{45}$$

As previously mentioned, the Regge pole idea is based on the study of the analytic properties of $A_l(s)$ and allowing the angular momentum l to become a continuous and complex variable, α, on which the amplitude $A_l(s)$ depends: $A_l(s) \to A(\alpha, s)$. Instead of studying the high energy scattering amplitude at finite momentum transfer in the *s-channel*, Regge studied the low scattering amplitude at large momentum transfer squared in the *t-channel*. The crucial step that enables this is the fact that the angular momentum and the scattering angle θ are conjugate to each other.

If we assume that in the complex angular momentum plane (α-plane) an analytical function $A(\alpha, s)$ exists, where $A(\alpha, s) = A_l(s)$ when $l = 0, 1, 2, 3...$, then according to the *Cauchy residue theorem*, the integration has a singularity if the plane is inside the closed curve.

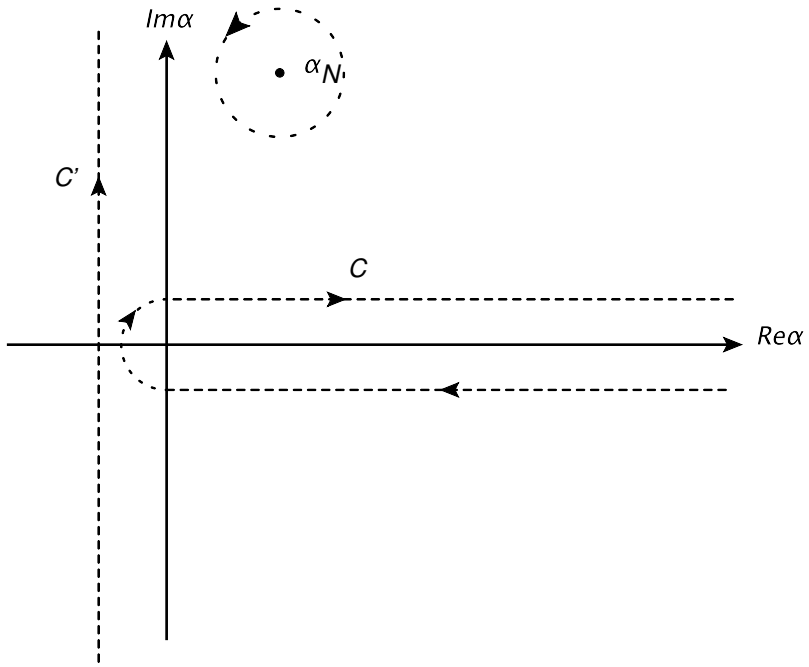

FIG. 3. Sommerfeld-Watson integration contour representation of the scattering amplitude.

By use of the *Sommerfeld-Watson transformation* [25], the wave expansion from the previous equation may be rewritten in the form of a contour integral in the complex angular momentum plane to give:

$$A(s,t) = \frac{1}{2i}\oint\limits_{C} d\alpha(2\alpha+1)\frac{A(\alpha,t)}{\sin(\pi\alpha)}P\Big(\alpha, 1+\frac{2s}{t}\Big), \tag{46}$$

where the contour C surrounds the positive real axis, as shown in the Fig. 3. The function $A(\alpha, s)$ is an analytical continuation of the partial wave amplitudes $A_l(s)$. The denominator $\sin(\pi\alpha)$ vanishes for integer l when $\alpha = l$, giving rise to poles called *Regge poles*. If we set $\alpha = l+\delta$ and take $\delta \to 0$, the residue from the term $1/\sin(\pi\alpha)$, according to the *Cauchy residue theorem*, yields $(-1)^l$. Therefore, the integral leads back to summation from Eq. (45).

The amplitude $A(\alpha,t)$ is unique when $A(\alpha,t) < e^{\pi|\alpha|}$ as $|\alpha| \to \infty$ [26]. Unfortunately, there are contributions to the partial wave amplitudes which alternate in sign (i.e. are proportional to $(-1)^\alpha$). Since the required inequality is violated along the imaginary axis, it is necessary to introduce two analytic functions $A^{(+1)}(\alpha,t)$ and $A^{(-1)}(\alpha,t)$. Therefore, Eq. (46) becomes:

$$A(s,t) = \frac{1}{2i}\oint\limits_{C} d\alpha\frac{(2\alpha+1)}{\sin(\pi\alpha)}\sum_{\eta=\pm1}\frac{(\eta+e^{-i\pi\alpha})}{2}A^{(\eta)}(\alpha,t)P\Big(\alpha, 1+\frac{2s}{t}\Big), \tag{47}$$

where $A^{(+1)}(\alpha,t)$ and $A^{(-1)}(\alpha,t)$ are called *even*- and *odd*-signature partial wave functions and $\eta = \pm 1$ is the signature of that partial wave.

If only simple poles exist (i.e.$A(\alpha,t)$), the contour C can be deformed into contour C' according to [27], which runs parallel to the imaginary axis with $\mathrm{Re}(\alpha) = -1/2$ and closes at infinity. Therefore:

$$\begin{aligned} A(s,t) = \frac{1}{2i}\int\limits_{-\frac{1}{2}-i\infty}^{-\frac{1}{2}+i\infty} d\alpha\Big[\frac{(2\alpha+1)}{\sin(\pi\alpha)}\sum_{\eta=\pm1}\frac{(\eta+e^{-i\pi\alpha})}{2}A^{(\eta)}(\alpha,t)P\Big(\alpha,1+\frac{2s}{t}\Big)\Big] \\ + \sum_{\eta=\pm1}\sum_{n_\eta}\frac{\eta+e^{i\pi\alpha_{n_\eta}(t)}}{2}\frac{\beta_{n_\eta}(t)}{\sin(\pi\alpha_{n_\eta}(t))}P\Big(\alpha_{n_\eta}(t),1+\frac{2s}{t}\Big). \end{aligned} \tag{48}$$

The simple poles $\alpha_{n_\eta}(t)$ are called *even*- and *odd*-signature *Regge poles*, ($\eta \pm 1$ respectfully) and $\beta_{n_\eta}(t)$ are the residues of the poles, multiplied by $\pi(\alpha_{n_\eta}(t)+1)$.

In order to isolate the high energy behavior of the scattering amplitude in the *Regge* region, we investigate the asymptotic behavior of *Legendre* polynomials by

using the crossing symmetry and deforming the contour. In the region of our interest ($s >> t$), *Legendre* polynomials are dominated by the leading term:

$$P_l\Big(1+\frac{2s}{t}\Big) \to \frac{\Gamma(2l+1)}{\Gamma^2(2l+1)}\Big(\frac{s}{2t}\Big)^l, \tag{49}$$

where $\Gamma(x)$ is the *Euler* gamma function. In this limit, the contribution to the right side of Eq. (48) along the contour C' vanishes as $s \to \infty$, so it can be neglected. Thus if we take the distribution from the dominant *Regge* pole, which has the largest value of the real part of $\alpha_{n_\eta}(t)$ we get:

$$A(s,t) \overset{s\to\infty}{\to} \frac{(\eta + e^{-i\pi\alpha})}{2}\beta(t)s^{\alpha(t)}, \tag{50}$$

where $\alpha(t)$ is the position of the leading *Regge* pole at some value t and with signature η. The factors depending on t but not on s have been absorbed into the function $\beta(t)$. Last equation represents the explicit dependence of the high energy amplitude in the *s-channel* on the *Regge* poles in the *t-channel*. The amplitude is a sum of powers of s, with exponents equal to the location of *Regge* poles α_n.

In the *t-channel* process, with positive t, the amplitude has poles which correspond to the exchange of physical particles of mass m_i and spin J_i, where $\alpha(m_i^2) = J_i$. By plotting the spins of low lying mesons against mass squared, Chew and Frautschi [16] noticed that they lie in a straight line. These straight lines are called *Regge trajectories* (see Fig. 4). The *Regge trajectories* are parameterized as:

$$\alpha(t) = \alpha(0) + \alpha' t, \tag{51}$$

where α' represents the slope of the *Regge trajectory* with conventional average value of $\alpha' \simeq 1$.

With respect to Eq. (50), the asymptotic s-dependence of the differential cross-section is given by:

$$\frac{d\sigma}{dt} \propto s^{(2\alpha(0)+2\alpha' t-2)}. \tag{52}$$

The amplitude from Eq. (50) can be viewed as the exchange of an object with complex angular momentum $\alpha(t)$. Although it can't represent a regular particle (due to non integer or half integer angular momentum and dependence on t), it can be viewed as the effective exchange of a whole series of particles lying on the same *Regge trajectory* $\alpha(t)$. This is called the exchange of a *Reggeon*.

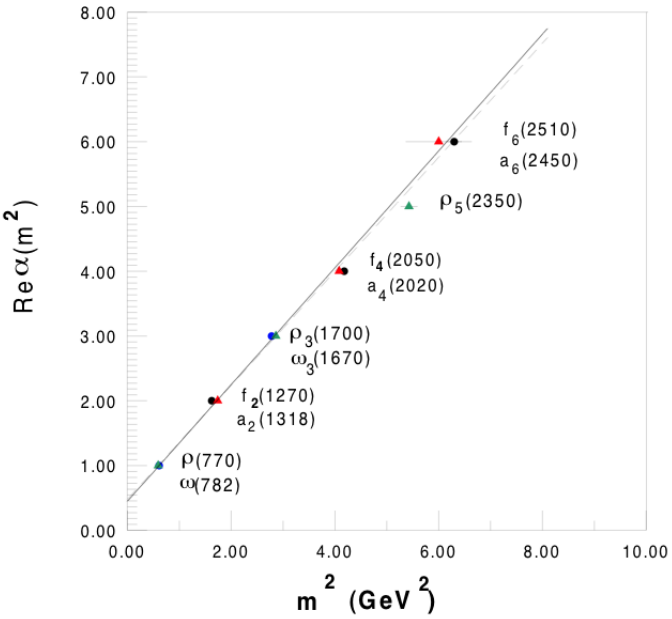

FIG. 4. The Chew-Frautschi plot for mesons, $\alpha(t)$ vs mass squared or t [GeV^2]. Regge trajectories lie in a straight line.

2.2.2 THE *POMERON*

The *Pomeron* as a Regge trajectory

Pomeranchuk [24] showed that under general assumptions, any scattering process in which charge is exchanged has a cross-section that vanishes asymptotically. Following his assumption, Foldy and Piers [28] proved that this particular scattering process must be dominated by the exchange of quantum numbers of the vacuum if its cross-section does not fall with the increase of s.

Using the intercept of the *Regge trajectory*, which dominates a particular scattering process, together with the optical theorem from Eq. (22), we obtain the asymptotic behavior of the total cross-section of that process:

$$\sigma_{tot} \sim \mathrm{Im}A_{1+2\to 3+4}(s, t=0) \sim s^{\alpha(0)-1}, \tag{53}$$

where α is the leading trajectory which can be exchanged in elastic scattering. At high energy all total cross-sections are nearly constant with energy, which in terms of the equation above implies that $\alpha(0) \approx 1$. However, this is not possible for meson

trajectories, which have $\alpha \approx 1/2$, nor of any other presently known trajectories. The trajectory with $\alpha(0) \approx 1$ is called the *Pomeron*, after I. Ya. Pomeranchuk.

It has been proven experimentally that the total cross-section does not vanish asymptotically, but slowly rises with the increase of s (when s reaches the values beyond $\sqrt{s} = 200\text{GeV}$). If this rise is attributed to the exchange of a single *Regge pole*, then the intercept of this *Reggeon* must have $\alpha(0) > 1$ and carrying the quantum numbers of the vacuum.

The precise nature of the *Pomeron* is still obscure. We generally refer to it as a pole. However, it is important to keep in mind that the *Pomeron* may be a much more complex object and empirical construct which describes the diffractive nature of elastic scattering and only simulates the properties of a pole at present.

The *Pomeron* trajectory has the internal quantum numbers of the vacuum, the isospin, strangeness and baryon number are all zero: $I = S = B = 0$. This trajectory is taken to represent the exchange of a virtual particle called the *Pomeron*. Particles with the quantum numbers of the vacuum are difficult to detect, but such particles can exist in QCD as bound states of gluons with $\alpha_{\mathbf{P}}(t = 0) = 1$.

2.2.3 THE *ODDERON*

Another *Regge* trajectory which may play a significant role in high energy scattering is the so-called *Odderon* [29], [30] and [31]. The *Odderon* is the $C = P = -1$ partner of the *Pomeron*. Presently there is no evidence from experimental data of the existence of the *Odderon* at low-$|t|$. Its existence would entail differences between the pp and $p\bar{p}$ asymptotic scattering amplitudes and cross-sections.

2.3 PHENOMENOLOGICAL MODELS OF pp AND $p\bar{p}$ ELASTIC SCATTERING

In order to understand and interpret an increasing number of experimental data of the diffractive process at low-$|t|$, several phenomenological models have been developed. *Regge* approach, described briefly in the previous section, tells us that the exchange of t-channel *reggeons* (with the *Pomeron* as the leading singularity), determines the asymptotic behavior of the cross-sections in the direct s-channel [5]. Other available phenomenological models, that are going to be explained in this section, have been successful, both quantitatively and qualitatively, in the description of various features of the diffraction process, i.e. cross-section energy dependence,

the diffractive slope and diffractive minima in the experimental data, ρ-parameter etc.

In general, the phenomenological models can be divided into two groups, t-channel and s-channel models. The *Regge* model (see Section 2.2), is a prototype of the so-called t-channel models and the optical models, or in other words eikonal models, belong to the class of so-called s-channel models. Both approaches are vastly used in the phenomenological description of the data and both have merits and shortcomings. None, so far, has been able to combine and unify various qualities of these two approaches. Many attempts have been made to construct channel independent model, but none with success.

This section is dedicated to the conceptual reviews of the traditional phenomenological models. Some of these phenomenological models are: Geometrical (Optical) models, proposed by Yang et al [32], [33], and Cheng *et al.* [2], the Impact Picture Model by Bourrely, Soffer and Wu [34], [35], [36], and Multiple Exchange Model by Donnachie and Landshoff [37], [38], [39].

2.3.1 THE GEOMETRICAL MODEL

The geometrical model is based on the idea of diffraction phenomena, borrowed from optics. Although two fields appear distant from each other, the analogy between optical and quantum mechanical diffraction is complete in the case of elastic scattering, where the internal structure of the interacting particles does not come into play. Similarities and differences between optical and hadronic diffraction are nicely presented in [5].

Yang *et al.* [40], [41], [42], [43], use a geometrical model to predict the existence of many diffraction dips in high energy hadron-hadron elastic scattering. In their model, the cross-sections are written following the eikonal formalism [5]. The starting point is the remark that high energy scattering is the shadow of absorption. Accordingly, the interacting hadrons are viewed as extended objects made of hadronic matter flying through each other, Fig. 5. At each point, the interaction is proportional to the local density of hadronic matter, assumed to have a distribution similar to the electric charge distribution [5]. The opacity is taken to be real so that the amplitude is purely imaginary. It is factorized as:

$$\Omega(s,b) = K(s)D(b), \tag{54}$$

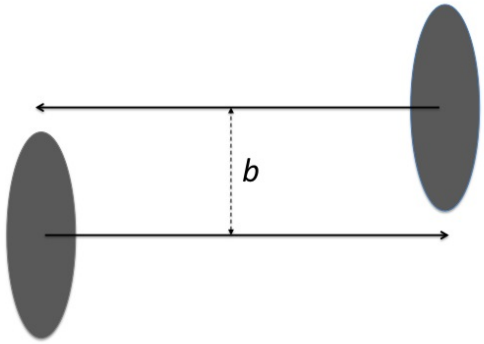

FIG. 5. Two hadrons colliding, at an impact parameter b (not to be confused with forward slope $B(s, t = 0)$). Due to their, near the speed of light velocity, the hadrons are contracted to thin disks. An analysis of the proton-proton cross-section suggests that high-energy protons are black disks.

where $K(s)$ is the energy-dependent quantity and a free parameter of the model, fitted to the σ_{tot} data and $D(b)$ is related to the form factors of the colliding particles and is obtained as follows:

$$D(\boldsymbol{b}) = \int d^2\boldsymbol{b'} T_A(\boldsymbol{b} - \boldsymbol{b'}) T_B(\boldsymbol{b'}), \tag{55}$$

where $T(\boldsymbol{b})$ is related to the charge density $\rho(\boldsymbol{b}, z)$ of the hadron by $T(\boldsymbol{b}) = \int_{-\infty}^{+\infty} dz \rho(\boldsymbol{b}, z)$ and A and B are the two hadrons. By introducing the form factors of A and B hadrons:

$$G_{A,B}(\boldsymbol{q}^2) = \int d^2\boldsymbol{b} e^{-i\boldsymbol{q}\cdot\boldsymbol{b}} T_{A,B}(\boldsymbol{b}), \tag{56}$$

$D(\boldsymbol{b})$, which depends only on $b \equiv |\boldsymbol{b}|$ is given by:

$$D(b) = \int \frac{d^2\boldsymbol{q}}{(2\pi)^2} e^{-i\boldsymbol{q}\cdot\boldsymbol{b}} G_A(\boldsymbol{q}^2) G_B(\boldsymbol{q}^2). \tag{57}$$

An indication of the geometrical model of Yang *et al.* [44] is the appearance of the diffraction pattern in the elastic cross-section with secondary maximum and a sharp minimum. The $|t|$ value of the minimum is proportional to $1/\sigma_{tot}$ and the forward slope $B(s, t = 0)$ to σ_{tot}. This model also provides a connection between

σ_{tot}, the ratio σ_{el}/σ_{tot} and the value of $d\sigma/dt$ at the second maximum, supported by the experimental data. However, the question that has not been answered by the geometrical approach is the s-dependence of the observables.

2.3.2 THE IMPACT PICTURE MODEL

An attempt to incorporate s-dependence derived from a perturbative field-calculation into the geometrical model was made by Bourrely, Soffer and Wu [35], [36], [45]. In their *impact picture model*, the opacity is of the same form as in Eq. (54), apart from an additive subleading term, and the function $K(s)$ is taken from [46], [47], [48]. The asymptotic behavior of the scattering amplitude they found, is:

$$s^{1+\epsilon}\ (\ln s)^{-3/2}, \tag{58}$$

where ϵ is a positive quantity which depends on the theoretical coupling constant. $K(s)$ has the crossing symmetric form of:

$$K(s) = \frac{s^a}{(\ln s)^b} + \frac{u^a}{(\ln u)^b}, \tag{59}$$

where a and b are constants and u is the third Mandelstam variable. The fact that a and b are constants implies that the *Pomeron* is a fixed Regge cut rather than a Regge pole. $D(b)$ is the same as given in Eq. (57). The impact picture model predicts that asymptotically σ_{tot}, σ_{el} and $B(s, t = 0)$ should all increase as $\ln^2 s$ and that the ratio σ_{el}/σ_{tot} should approach $1/2$, which is in agreement with experimental data. A schematic representation of the expanding proton in the impact picture is described with almost completely absorbing (ie. black) proton core which has a radius that grows with $\ln s$ and the peripheral region, which is partially absorbing (i.e. gray) and has a width independent of s (see Fig. 6). A complete account of this theory can be found in [2].

2.3.3 MULTIPLE EXCHANGE MODEL

Processes at high energies and low-$|t|$ are believed to be controlled by single *Pomeron* exchange [38]. The *Pomeron* couples to the quarks like the photon with more or less constant μ-coupling but with a Regge signature factor which gives it an even C-parity, as observed by Landshoff and Polkinghorne [49]. The multiple exchange model for high energy scattering, proposed by Donnachie and Landshoff

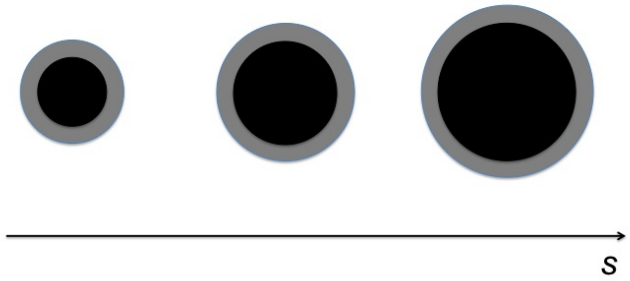

FIG. 6. Schematic representation of expanding proton [2].

[37], is based on the idea that pp and $p\bar{p}$ scattering at high-$|t|$ proceeds via the exchange of three gluons which couple to the proton or antiproton valence quarks, Fig. 7. The amplitude of this process has opposite signs for pp and $p\bar{p}$, which also explains the difference between pp and $p\bar{p}$ data in the dip-shoulder region. This model predicts no secondary minima in pp at high-$|t|$.

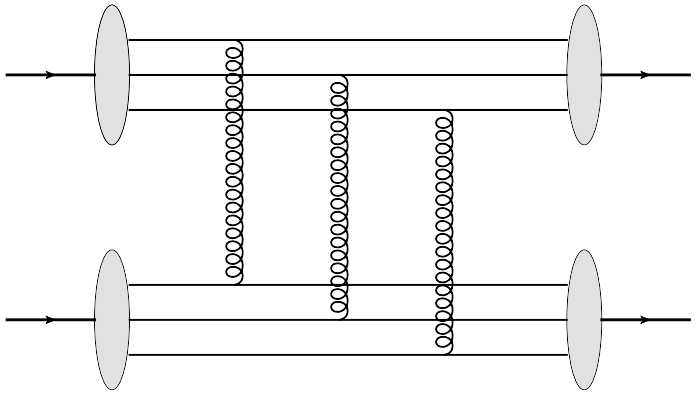

FIG. 7. The triple-gluon exchange in pp and $p\bar{p}$ elastic scattering.

Donnachie and Landshoff use six types of exchanges in their model: Single-*Pomeron* (P) exchange, double-*Pomeron* (PP) exchange, and triple-*Pomeron* (PPP) exchange. Then, *Reggeon* (R) exchange, *Reggeon-Pomeron* (RP) exchange, triple-gluon (ggg) and exchange of a *Pomeron* plus two gluons (Pgg). For details on these exchange mechanisms see Ref. [37].

2.4 OVERVIEW OF pp AND $p\bar{p}$ ELASTIC SCATTERING

Elastic scattering has been studied in pp and $p\bar{p}$ collisions at the CERN Intersecting Storage Ring (ISR), Tevatron at FNAL and RHIC at BNL, see Table 1. At CERN's ISR, the highest *cms* energy in pp collisions is at $\sqrt{s} = 62.8$ GeV with unpolarized beams and at $\sqrt{s} = 20$ GeV with polarized beams. The $p\bar{p}$ collisions have been studied at $\sqrt{s} = 53$ GeV, also at the CERN ISR, and at $\sqrt{s} = 1.8$ TeV at the Tevatron (FNAL). On the other side, RHIC (BNL) provides a unique opportunity to cover a previously unexplored *cms* energy range ($50 - 500$ GeV) for the study of polarized pp collisions.

TABLE 1. Overview of pp and $p\bar{p}$ elastic scattering experiments.

Collider Accelerator Facility	Type of Experiment	Center of Mass Energy $\sqrt{s}$
ISR at CERN	pp collisions (unpolarized)	62.8 GeV
ISR at CERN	pp collisions (polarized)	20 GeV
ISR at CERN	$p\bar{p}$ collisions	53 GeV
Tevatron at FNAL	$p\bar{p}$ collisions	1.8 TeV
RHIC at BNL	pp collisions (polarized)	$50 - 500$ GeV
LHC at CERN	pp collisions (unpolarized)	$7 - 14$ TeV

Physics motivation behind all these experiments is the measurement of both spin-averaged and spin-dependent observables in elastic and inelastic processes:

- **Spin-averaged Observables in Elastic Scattering:** The differential elastic

cross-section $d\sigma_{el}/dt$, the total cross-section σ_{tot}, the nuclear slope parameter B and the ratio of the real to imaginary part of the forward scattering amplitude ρ.

- **Spin-dependent Observables in Elastic Scattering:** The analyzing power A_N, the double spin correlation parameters A_{NN}, A_{SS} and A_{LL} (with transverse and longitudinal beam polarization) and the difference in the total cross-section as a function of initial transverse spin states $\Delta\sigma_T = \sigma_{tot}^{\uparrow\downarrow} - \sigma_{tot}^{\downarrow\uparrow}$.

2.4.1 ELASTIC CROSS-SECTIONS

Elastic events at hadron colliders are identified by the detection of two, back-to-back particles in the final state. The difficulty is that scattering angles, of the order of fractions of mrad, get smaller and smaller with the increase of energy. Hence, detectors need to be placed very close to the beam, inside the beam pipeline. In order to achieve this, a device known as "Roman pot" is used [50]. The detectors are placed into the Roman pots which are normally left in a retracted position so that the beam, when injected, circulates freely inside the beam vacuum pipeline. When the desired energy has been achieved and the beam is stable, the Roman pots are slid into their operational position until the inner detectors are just a few millimeters from the beam. The detectors which are inserted into Roman pots are designed to accept a high particle rate and have good spatial resolution (about 100μm). The types of detectors which are usually inserted into Roman pots are drift chambers, hodoscopes, scintillating fibers or silicon micro-strip detectors (see Section 3.5.1).

Hadron collider experiments usually require the highest possible luminosity and therefore the transverse size of the beam is reduced as much as possible at the interaction point. In this case, the beam size at the detection point for elastically scattered protons is large, the angular beam divergence of the beam is increased and a large fraction of elastically scattered particles are not accessible for detection. Contrary to this, in the case of elastic scattering experiments, the beam size at the interaction point is made relatively large and, consequently, the luminosity is reduced. This is not a problem for elastic scattering experiments since the differential cross-section is large at low-$|t|$. The elastically scattered protons, however, are now well separated from the narrow beam at the detection point.

The ratio of integrated elastic to the total cross-section is known to decrease at

low energies and reach a constant value. The measurements for pp are quite precise, contrary to $p\bar{p}$ data, which are not as accurate, but compatible with the pp data within errors. This constancy is a prediction of the geometrical model (see Section 2.3.1). However, at higher energies, the ratio σ_{el}/σ_{tot} increases with energy (Fig. 8), which is not only a strong argument against this model, but can be also be taken as evidence that hadrons become more and more opaque with the increase of energy. The growth of σ_{el}/σ_{tot} with energy is in agreement with various models such as Cheng and Wu [2] and Bourelly, Soffer and Wu (see Section 2.3.2).

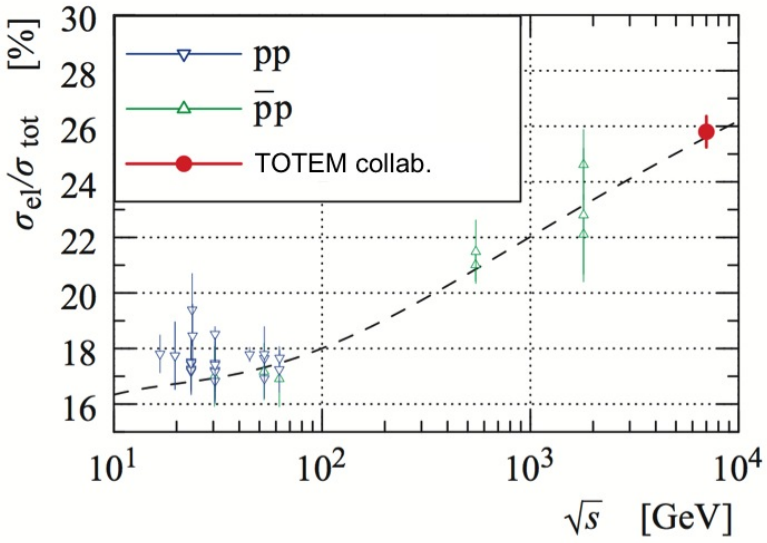

FIG. 8. The ratio of σ_{el}/σ_{tot} as a function of the $\sqrt{s}$. The dashed line shows the ratio of the $\sigma_{el}(s)$ and $\sigma_{tot}(s)$ fits from [3].

2.4.2 THE TOTAL CROSS-SECTION

The exact growth of the total cross-sections with energy is a puzzle that many tried to resolve. It has been present for nearly forty years now. Initially, it was believed that the total cross-sections would become asymptotically constant. This turned out not to be the case and the very first evidence of total cross-section growth with energy came from preliminary results of the Serpukov accelerator on $\pi^{\pm}p$ and

$K^{\pm}p$ scattering at $p_L \sim 60$ GeV [5]. This observation was confirmed for both, pp and $p\bar{p}$, total cross-sections by the ISR and FNAL experiments [51], [52]. These data were compatible with the asymptotic equality of $\sigma_{tot}(pp)$ and $\sigma_{tot}(p\bar{p})$ predicted by the Pomeranchuk theorem, [24]. The growth of $\sigma_{tot}(p\bar{p})$ became macroscopically visible from SPS data at $\sqrt{s} = 0.546$ TeV and $\sqrt{s} = 0.90$ TeV, [53], [54], [55], and with the Tevatron data at $\sqrt{s} = 1.8$ TeV, [56], [57], [58]. The pp and $p\bar{p}$ total cross-section data are presented in Fig. 9 together with a fit to a $\ln^{\gamma}s$, [5]. This growth is discussed in Section 2.3 as evidence that the proton becomes larger and blacker as seen by an incoming hadron of increasing energy.

The exact growth of $\sigma_{tot}(pp)$ and $\sigma_{tot}(p\bar{p})$ with energy is both delicate and

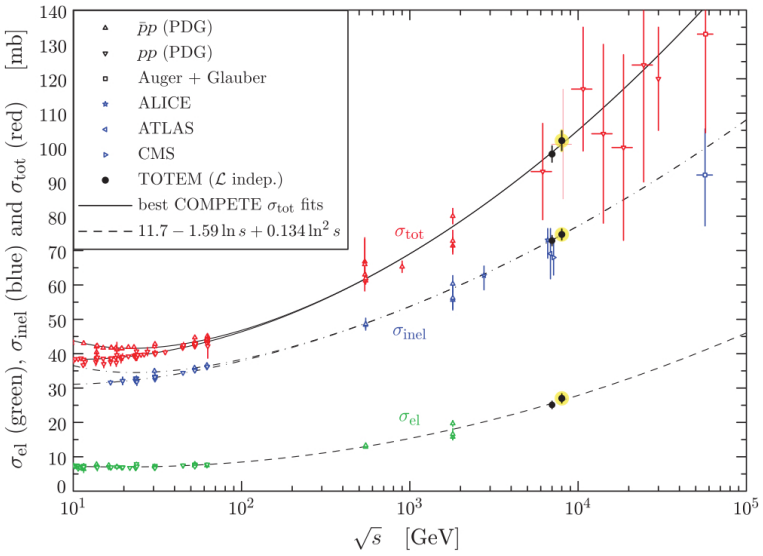

FIG. 9. Total pp and $p\bar{p}$ cross-sections fitted to a $\ln^{\gamma}s$ behavior [3], [4].

unresolved. An approximate $\ln^{\gamma}s$ ($\gamma = 2.2 \pm 0.3$) is suggested, which saturates the energy growth permitters by the Froisart-Martin bound, [5]. Phenomenologically, the uncertainties of the data do not dismiss the possibility of an $\ln s$ growth (note the discrepancy between the two Tevatron measurements at $\sqrt{s} = 1.8$ TeV). Cosmic ray data do not lead to a conclusion regarding the increase [59], [60] and the E710 result tends to favor a $\ln s$ increase, while CDF result favors $\ln^2 s$ dependence. The TOTEM

collaboration at LHC measurements of σ_{tot} at $\sqrt{s} = 7$ TeV [3] and $\sqrt{s} = 8$ TeV [4], are both in good agreement with the extrapolation of the lower energy measurements. At $\sqrt{s} = 14$ TeV at the LHC, the difference between the $\ln s$ and $\ln^2 s$ fits is about 15 mb.

The available data for $\sigma_{tot}(s)$ for both pp and $p\bar{p}$ can also be fitted successfully by a mild power dependence [9]. However, to distinguish between power and $\ln^2 s$ growths one needs to measure at very high energies, which is hard to achieve. Similarly, the combination of a $\ln s + C$ term is also indistinguishable from a combination containing a $\ln^2 s$ term. From the physics point of view, any power behavior, taken at face value, would violate unitary and, consequently, should be modified. On the other hand, no such argument exists against any $\ln^\gamma s$ behavior as long as $\gamma < 2$.

According to the Pomeranchuk theorem, [24], $\sigma_{tot}(pp)$ and $\sigma_{tot}(p\bar{p})$ become equal at asymptotic energies (present data can be used if they were already assymptotic). The power law fit to the difference between $\sigma_{tot}(pp)$ and $\sigma_{tot}(p\bar{p})$ gives $\Delta\sigma_{tot} \sim s^{-0.56}$, which is in agreement with the theoretical predictions by Regge theory. In fact, the *Pomeron* contributions cancel out in the $\sigma_{tot}(pp)$ and $\sigma_{tot}(p\bar{p})$ difference an the $\Delta\sigma_{tot}$ is dominated by a secondary *Reggeon* trajectory with an intercept close to 1/2.

However, this is not quite so conclusive since maximum energies obtained for both $\sigma_{tot}(pp)$ and $\sigma_{tot}(p\bar{p})$ data are in the ISR range ($\sqrt{s} \simeq 62$ GeV). Unfortunately, at the time being, there are no plans for extending this energy range at LHC or RHIC.

2.4.3 THE REAL PART OF THE FORWARD ELASTIC AMPLITUDE

As described in section 2.1.3, the optical theorem gives the relation between total cross-section and imaginary part of the forward scattering amplitude [5]. It tells us that the imaginary part of the forward amplitude incases with energy, Eq. (22), while no such constraint exists for the real part. The measurement of the real part of the forward scattering amplitude, which in turn is complementary to the measurement of the total cross-section, is directly related to the measurement of the ρ-parameter. In addition, ρ is a very sensitive indicator of several theoretical properties.

The ρ dependence on energy is shown on Fig. 10. In the region where the total cross-section is first decreasing with energy and then rising, ρ, which is initially negative, will rise, going through zero when the cross-section has a minimum and becoming positive at high energy.

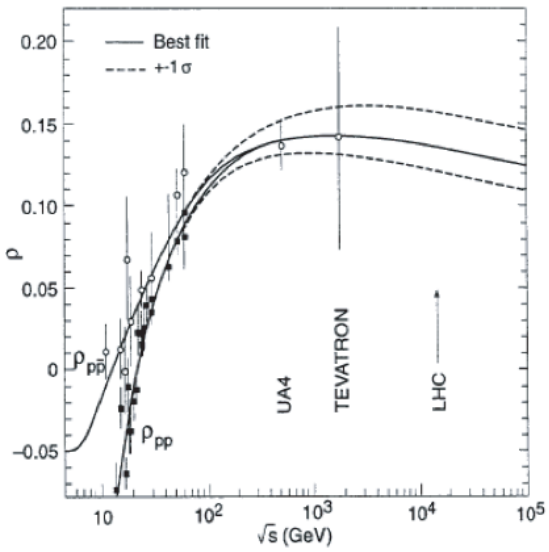

FIG. 10. The ρ parameter for pp (black circles) and $p\bar{p}$ (white circles) as a function of the energy. The solid line represents the dispersion relation fit with the 1σ uncertainty region determined by the dashed lines [5].

Experimentally, the measurement of $\rho(s)$ is performed by observing the interference of the hadronic amplitude F_h, parameterized as in Eq. (33) in the low-$|t|$ region, with the known Coulomb amplitude which is given with Eq. (29). Coulomb scattering becomes dominant at low-$|t|$, and the two amplitudes become comparable, Eq. (41). At present energies, $t_0 \sim 10^{-3}$ GeV^2, which is the region where the measurement of the real part of the amplitude is possible. At this $|t|$ range, $|F_h|^2$ can be neglected and the interference term is proportional to $(\rho \pm \alpha_{em}\phi)$. The relative phase was first calculated by Bethe (1958) in a potential scattering model [61], and later investigated by many authors [62], [63].

2.4.4 THE FORWARD PEAK

The high energy t-distribution shows a pronounced diffraction peak (forward peak). Theory and data show that the slope of the diffraction peak depends on s. In natural units, the slope of a diffraction peak has units of $length^2$ which suggests that there is a relation between this quantity and the hadron size or, equivalently, the total cross-section, with the expectation to with grow energy as

$(\ln s)^{\gamma}$. And indeed, the data show this growth of B with energy, Fig. 11. The

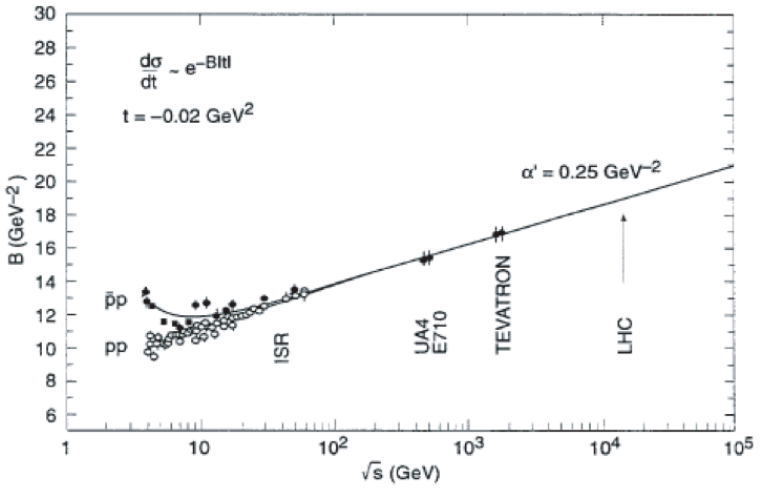

FIG. 11. Current World data on the nuclear slope of the forward peak B. A growth of B is observed with the increase of cms energy [5].

solid line in Fig. 11 represents the Regge prediction of the growth of $B(s)$. In the high-s region, it is represented as a straight line with a slope given by the *Pomeron* slope $B(s) = B_0 + 2\alpha'_P \ln s$. From this figure it can be estimated that the value of $\alpha'_P \approx 0.25$ GeV^{-2}, which is in a good agreement with other estimates.

The only direct high energy comparison between pp and $p\bar{p}$ slopes in the diffraction region is at ISR energies [64]. The ratio $B(p\bar{p})/B(pp)$ decreases towards 1 as the energy increases and reaches unity at approximately 62 GeV. The overall diffraction peak at $|t| < 0.5$ GeV^2 is not described by simple exponential. For $|t| > 0.02$ GeV^2 the slope $B(s)$ is found to decrease which is visible in both ISA [65] and SPS [53], [54]. At $0.2 < |t| < 0.3$ GeV^2 the slope is below $|t| \simeq 0$ for about two units of GeV^{-2}. Contrary to this $B(s)$ behavior, the Tevatron data [56], [57] show no evidence of B decreasing with $|t|$. However, this decrease is accounted for by various models such as Bourely, Soffer and Wu (see Section 2.3.2), [36], [66], [67].

CHAPTER 3

EXPERIMENT

3.1 RELATIVISTIC HEAVY ION COLLIDER (RHIC)

The Relativistic Heavy Ion Collider (RHIC) is an accelerator facility at the Brookhaven National Lab (BNL) on Long Island, New York. Its main goal is to provide collisions of heavy ions (i.e.^{197}Au) and lighter ions all the way to protons (including polarized protons) at energies of up to 100 GeV/c per beam for the heavy ions, and up to 250 GeV/c for unpolarized or polarized proton beams [68]. The complete RHIC facility is a complex set of interconnected accelerators (see Fig. 12).

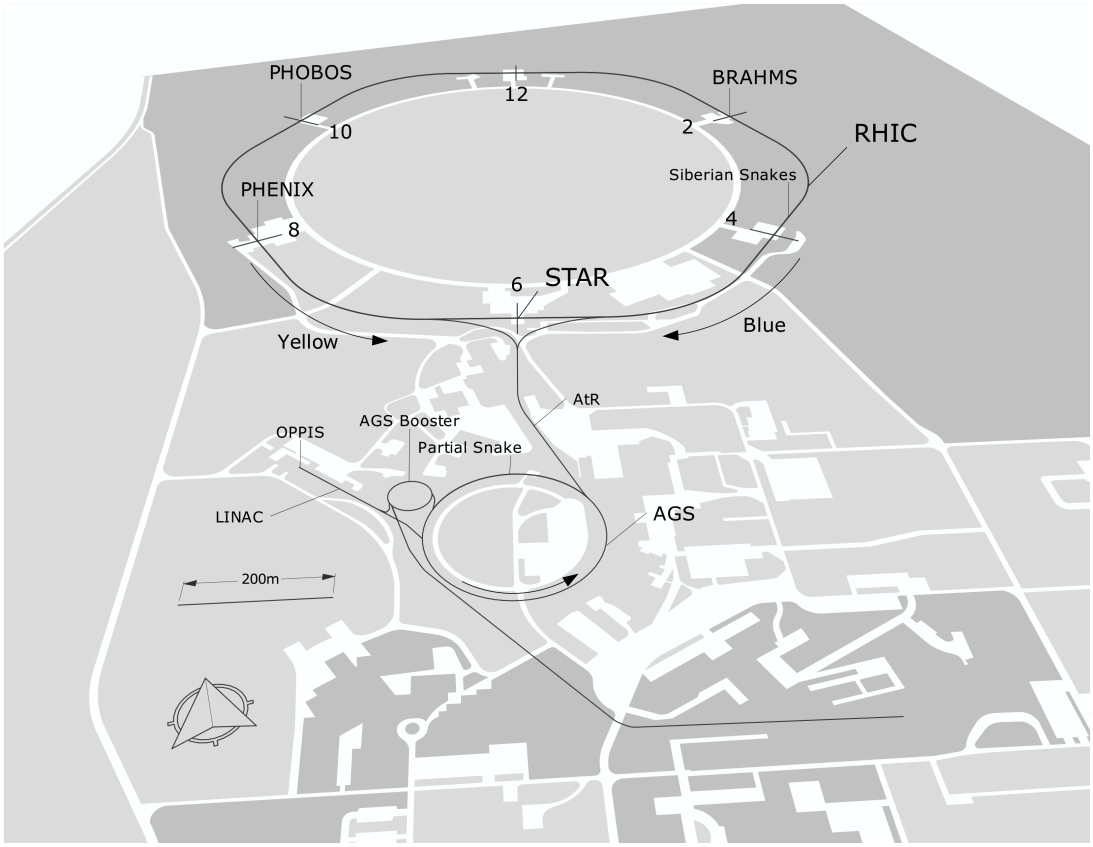

FIG. 12. Overall layout of the Brookhaven National Laboratory accelerator complex.

1. ***The Linear Accelerator (Linac):*** For collision of proton beams at RHIC, protons are supplied by the 200 MeV/c Linac. Protons from the Linac are then transferred to the Booster Synchrotron.

2. ***The Booster synchrotron*** is a powerful circular accelerator that provides the protons with more energy. The ions are accelerated to higher and higher speeds, getting closer to the speed of light. The Booster synchrotron accelerates protons to 1.5 MeV/c. The Booster then feeds the beam into the Alternating Gradient Synchrotron (AGS).

3. ***Alternating Gradient Synchrotron:*** The AGS is filled with proton bunches previously accelerated in the Booster. The bunches are then accelerated further to 24 GeV/c.

4. ***RHIC:*** The RHIC is an intersection storage ring particle accelerator. It consists of two independent concentric accelerator/storage quasi-circular rings of superconducting magnets, each with a circumference of 3.8 km. One ring is called the Blue Ring, where the beam moves in a clockwise direction and the other one is known as the Yellow Ring, where the beam moves in a counter-clockwise direction. The rings share a common horizontal plane inside the tunnel, with each ring having an independent set of bending and focusing magnets as well as radio frequency acceleration cavities. This allows independent tuning of the magnetic fields in each ring which is required to achieve equal rotation frequencies of the different particle/ion species in each ring. In RHIC, the counter-rotating proton beams are accelerated up to an energy of 250 GeV/c per beam and can be collided at six interaction regions (IR). The IRs are spaced equidistant around the circumference, separated by arc sections (Fig. 12).

Presently, there are two active experiments at RHIC positioned in the 6 o'clock and 8 o'clock IRs. One of those two experiments is the STAR experiment [69] (located at the 6 o'clock IR of RHIC). The *Physics With Tagged Forward Protons At The STAR Detector* experiment is part of the STAR experimental program [70].

3.2 THE STAR DETECTOR

STAR [71] is one of the two presently active detectors, located at the 6 o'clock interaction region. The physics motivation behind STAR is to investigate the behavior of strongly interacting matter at high density and to search for the signatures of quark-gluon plasma (QGP). STAR was designed for measurements of hadron production over a large solid angle. It incorporates high precision tracking systems for particle identification at the central rapidity region. It measures many observables simultaneously in search of a possible phase transition from hadronic matter to QGP and studies space-time evolution of the collision process in ultra-relativistic heavy ion collisions. In addition, apart from its heavy ion program, STAR has an active spin physics program oriented towards the study of the nucleon spin structure and a program with tagged forward protons (see Section 3.3) for the study of the spin-dependent and spin-averaged observables in pp elastic scattering and central production at very low-$|t|$. For the purpose of its program with forward protons, STAR has an additional system of forward detectors called the Roman pots (see Section 3.4).

The STAR detector with its subsystems (other than the Roman pot (RP) subsystem) is shown in Fig.13. The entire detector is enclosed in a solenoidal magnet that provides a uniform magnetic field of maximum value 0.5 T parallel to the beam direction. This feature allows measurements of the momenta of charged particles. At the heart of the STAR detector is the Time Projection Chamber (TPC) which is used for charged particle tracking and particle identification. The TPC covers a pseudo-rapidity range of $|\eta| \leq 1.8$ with complete azimuthal coverage. In order to extend this coverage to the forward region, two Forward Time Projection Chambers (FTPC) are installed which extend pseudo-rapidity coverage to $2.5 \leq |\eta| \leq 4$ on either side of the TPC in forward and backward rapidity, also with full azimuthal coverage. A barrel Time-of-Flight (TOF) detector is also installed in STAR and it consists of 120 trays covering the range of $|\eta| \leq 0.9$ in full azimuthal coverage. The TOF trigger system has two Pseudo Vertex Position Detectors (upVPD), each located 5.7 m away from the TPC center along the beam line providing the start time information to it. The full Barrel Electro Magnetic Calorimeter (BEMC) and End-cap Electromagnetic Calorimeter (EEMC) are used for detection of charged particles covering $|\eta| < 1$ and $1 \leq |\eta| \leq 2$ respectively. Calorimeters include Shower-Maximum Detectors (SMD) for distinguishing between

deposited energy from a single photon or from photon pairs arising from neutral pion (π_0) or $|\eta|$ meson decays. For detecting photons at forward rapidity, the Photon Multiplicity Detector (PMD) is used. This detector covers a pseudo-rapidity range $-3.7 < \eta < -2.3$ with full azimuthal coverage.

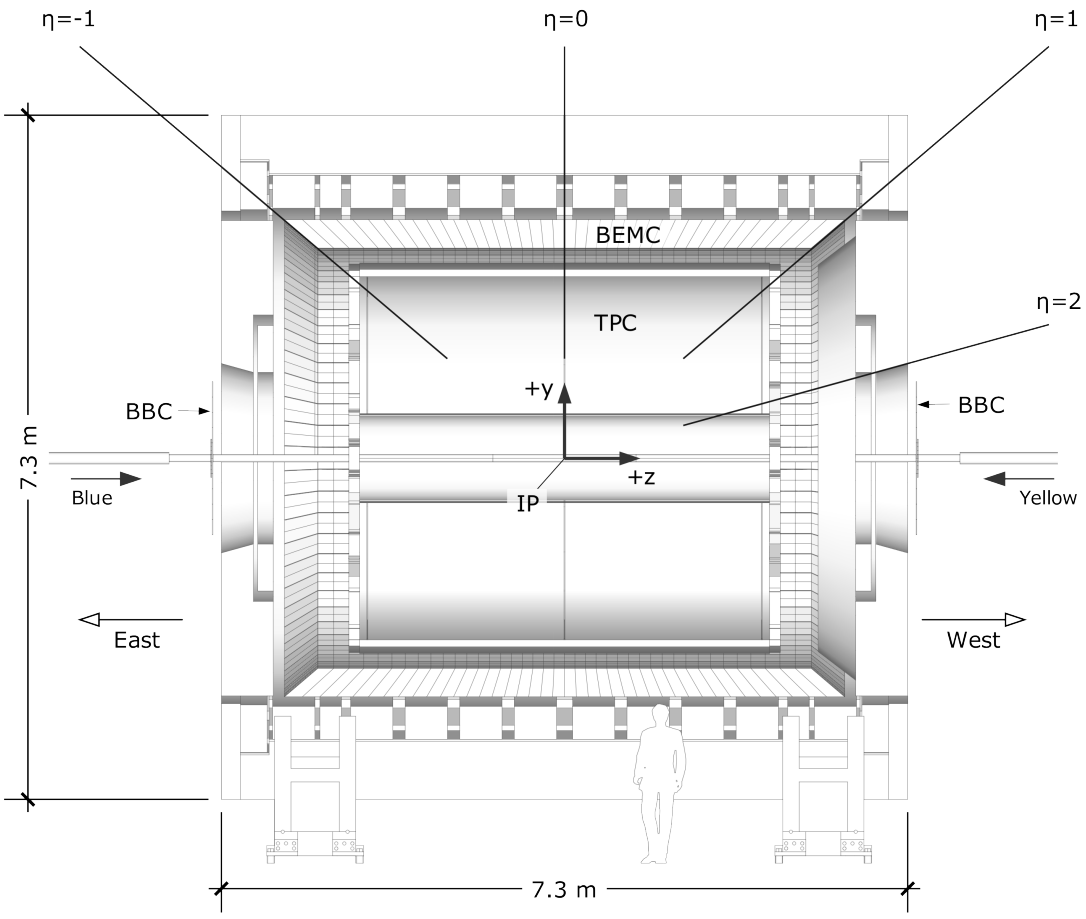

FIG. 13. Cross-sectional view of the STAR detector.

As previously mentioned, the STAR detector has a set of Roman pot (RP) detectors located in the very forward direction, about sixty meters away from the IP. The Roman pots are used as a part of the STAR physics program with tagged forward protons, explained in the following section.

3.3 PHYSICS WITH TAGGED FORWARD PROTONS AT THE STAR DETECTOR

"Physics With Tagged Forward Protons At The STAR Detector" experiment (formerly known as the *pp*2*pp* experiment [70]) is designed to study elastic proton-proton (*pp*) scattering at the Relativistic Heavy Ion Collider (RHIC) at Brookhaven National Laboratory (BNL). One of the objectives of this experiment is the study of differential cross-sections and polarization effects in *pp* elastic scattering by using both unpolarized and polarized proton beams at all center of mass energies available at RHIC, $50 \leq \sqrt{s} \leq 500$ GeV, in the four momentum transfer squared range of $0.003 \leq |t| \leq 0.03$ $(\mathrm{GeV/c})^2$. With unpolarized proton beams, the focus of this experiment is on the differential elastic cross-section together with the nuclear slope parameter B of *pp* elastic scattering and their dependences on $\sqrt{s}$ and t. Moreover, the total elastic cross-section and the ratio of real to imaginary part of the hadronic scattering amplitude, the parameter ρ, are of great interest and importance.

Elastic events are identified by detecting two, and only two, back-to-back scattered particles in the final state. In the case of *pp* collisions, the two colliding beams have the same energy and very small cross-section. The difficulty is that the higher the energies of the incoming beams, the smaller the scattering angles so there is a need for retractable detectors called Roman pots [50], which can reach the positions very close to the beam inside the beam pipe.

3.4 ROMAN POT DETECTOR SYSTEM

Roman pots are cylindrical vessels that house the detector system isolating it from the high vacuum of the accelerator beam pipe [50]. The name Roman was chosen because this technique was first used by a CERN group from Rome in the early 1970s to study *pp* collisions at CERNs intersecting storage rings (ISR). The pots are connected to the vacuum chamber of the collider by bellows, which are compressed as the pots are pushed towards the particles circulating inside the vacuum chamber. In their retracted position, the Roman pots do not obstruct the beam, leaving the aperture of the vacuum chamber free for the beams during their injection and ramp. Once the beams are brought into collision, the Roman pots are moved inside the beam pipe as close as a few mm to the beam, without disturbing the stability of the circulating proton beams. Thus, the Roman pots are moved during operation, approaching the detectors close to the beam and enabling detection of forward

scattered particles, while the detectors remain isolated from the beam vacuum.

The windows of the Roman pots are made of stainless steel with a thickness of 300 μm. The thin stainless steel minimizes the material through which the proton passes, but must maintain its strength, preserving the beam pipe vacuum, in the event the proton beam is accidentally dumped directly into the pot. As the interior of the pot is at atmospheric pressure and the exterior is exposed directly to the beam vacuum, the window frame serves to prevent the thin window from deforming into the beam.

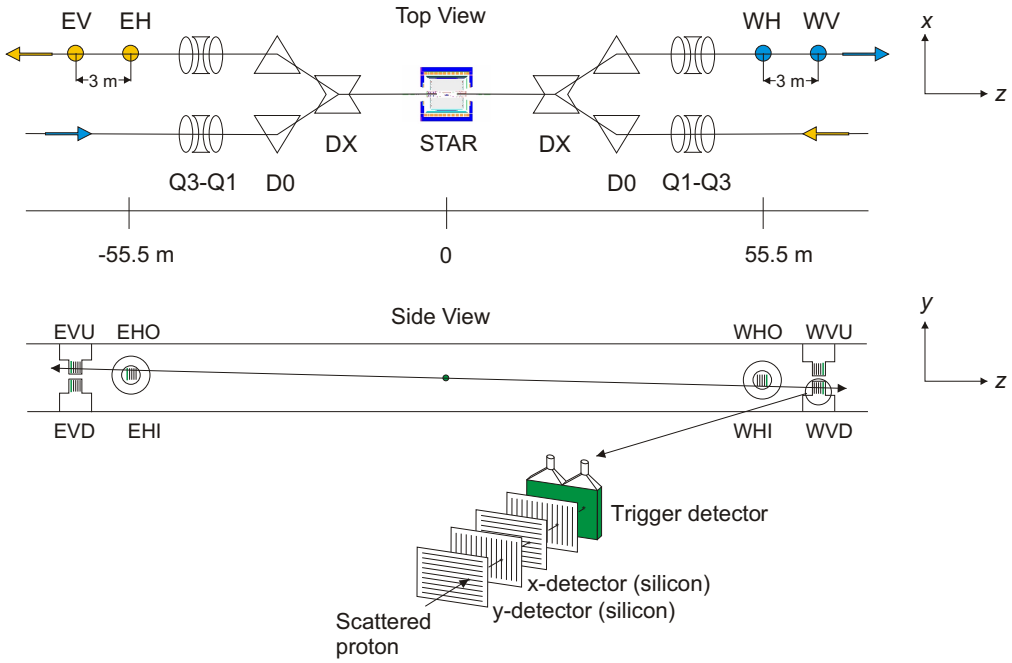

FIG. 14. Roman Pot detector system layout [6].

The layout of the "*pp*2*pp* at STAR" experiment consists of a total of four RP stations, two horizontal and two vertical RP stations [6]. These stations are

symmetric with respect to the STAR interaction point (IP) and are positioned on both sides of the STAR IP at 55.5 m and 58.5 m along the outgoing beam pipeline. One station consists of two RPs on opposite sides of the beam (see Fig.14). Each of the RPs in the system houses a single detector package which consists of four silicon micro-strip detector layers (two X-view and two Y-view), one scintillator which is connected to two photo multiplier tubes (PMTs), detector assembly structure and temperature measuring system. Two of the silicon micro-strip detector layers (X-view detectors) measure the x-coordinate in horizontal RP stations and y-coordinate in vertical RP stations. The other two silicon micro-strip layers (Y-view detectors) measure the y-coordinate in horizontal RP stations and x-coordinate in vertical RP stations. X-view detectors consist of 756 micro-strips and Y-view detectors have 504 active micro-strips.

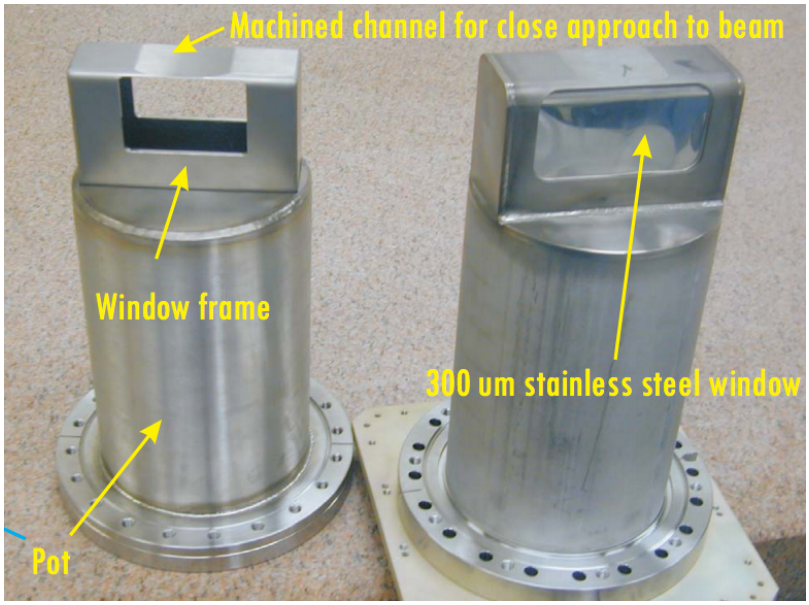

FIG. 15. Components of the "*pp*2*pp* at STAR" Roman pot detector system: Roman pot housing.

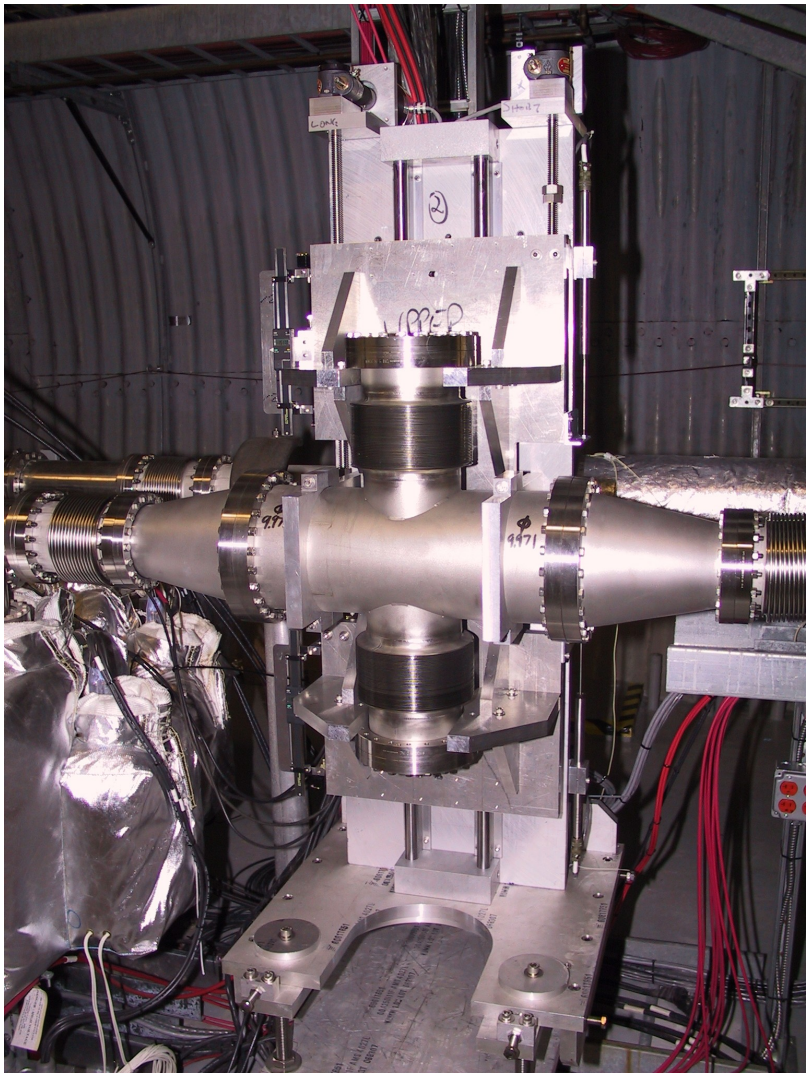

FIG. 16. Components of the "*pp*2*pp* at STAR" Roman pot detector system: Roman pot detector station (vertical).

SVXIIE chips are used for the readout of the silicon micro-strip detectors [72]. Each SVXIIE chip reads signals from 128 strips (126 active) of the silicon micro-strip detector. X-view detectors have six SVXIIE chips and Y-view detectors have four.

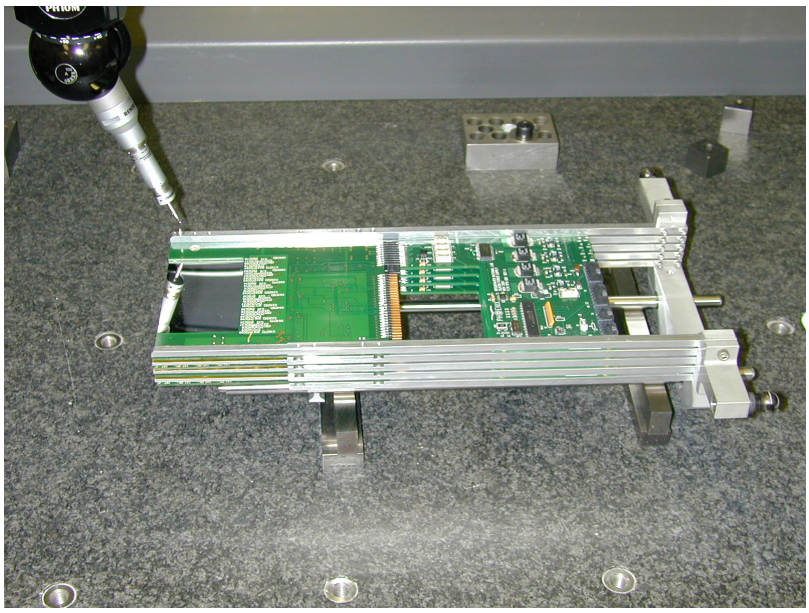

FIG. 17. Components of the "*pp*2*pp* at STAR" Roman pot detector package: Roman pot detector package assembly.

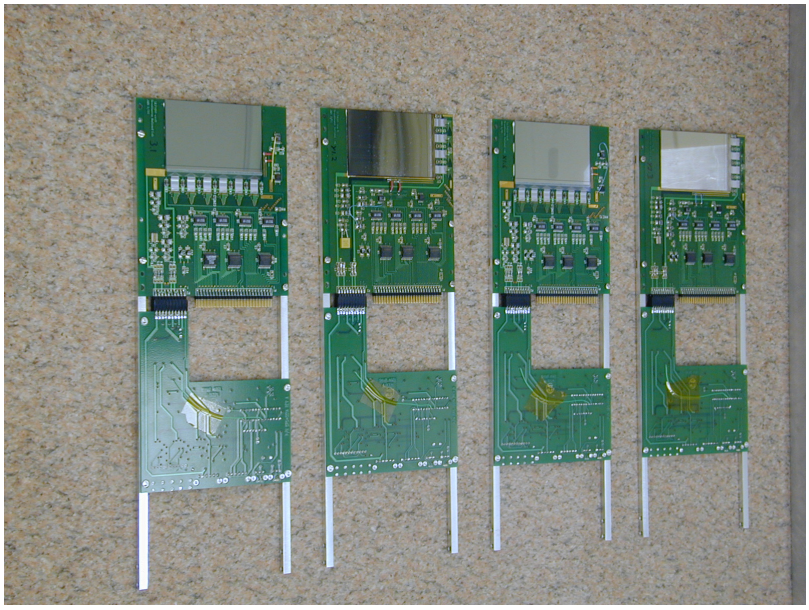

FIG. 18. Components of the "*pp*2*pp* at STAR" Roman pot detector package: Roman pot detector package boards.

3.5 SILICON MICRO-STRIP DETECTORS

Silicon micro-strip detectors have a special place in experimental particle physics [7] for many reasons, especially due to the properties of the silicon material. The relatively high density of silicon is one of the essential properties of this material that allows highly precise position measurements if used for tracking detectors (even less than 10 μm). Very good mechanical properties (i.e. elasticity), very well developed manufacturing technology and affordability of silicon are the main reasons of their wide spread use in various experiments.

The basic idea of silicon detectors is based on p-n junction diodes which are made from a junction of p-type (positive-type) and n-type (negative-type) silicon. A p-type junction is made by doping silicon crystals with boron (which has three valence e^-). p-type material has holes as its majority charge carriers. On the other hand, n-type material is made by doping pure silicon crystals with phosphorus (five valence e^-), which leaves excess electrons in the material. Those electrons became majority charge carriers of n-type material. The number of majority carriers in the material, which is determined by doping concentration, determines the resistivity (or conductivity) of the material [73].

3.5.1 PHYSICAL DESCRIPTION AND PROPERTIES OF SILICON MICRO-STRIP DETECTORS

A silicon micro-strip detector is constructed by implementing thin strips of highly doped p-type silicon over an n-type silicon wafer. The backplane of the wafer is made of a thin layer of aluminum. This is done for protection and ensures good electrical conductivity along the backplane. At the end of each silicon p-type micro-strip there is an implanted resistor. The top surface of the silicon wafer is layered with a thin layer of SiO_2 glass, which is an excellent insulator. Aluminum strips run above and along the length of p-type micro-strips. Together they create a series of capacitors. A silicon micro-strip detector cross-sectional view is shown in Fig. 19. Each Al strip is connected to charge-integrating preamplifiers which are implemented in the SVXIIE readout chips. A thin Al ring (a guard ring) surrounds all the strips in the detector and is used to eliminate edge-related leakage current from the rest of the detector.

Key parameters of silicon micro-strip detectors are the spacing between two consecutive micro-strips (strip pitch) and the detector capacitance. The pitch of the

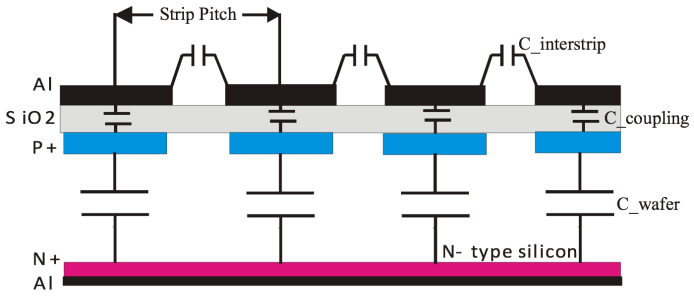

FIG. 19. Silicon micro-strip detector cross-sectional view [7].

micro-strip detectors in the "*pp*2*pp* at STAR" experiment is 100 μm [7]. With this pitch, the spatial precision of these silicon micro-strip detectors is expected to reach $100/\sqrt{12}\mu\text{m}\simeq 28.8$ μm. $1/\sqrt{12}$ is the sigma of the uniform probability distribution. This calculation is based upon the assumption that all of the charge created in the vicinity of the strip is solely collected by that strip. In reality, however, this is not the case and the charge sharing between two consecutive micro-strips is highly probable.

In the case of minimum ionizing particles, the number of created charges is, in general, small so the space charge effects that tend to expand the charge cloud are small as well. In this case, the charge cloud does not expand more than 1 μm. On the other hand, in the case of highly ionizing particles, the number of charges created is high, as are the space charge effects in the charge cloud. In this case, it is expected that the charge drift effect is large, which makes charge sharing between two consecutive micro-strips almost inevitable. However, by shortening of the drift time this problem can be easily solved. This is accomplished by over-depleting the detector and creating a smaller resistivity in the silicon bulk. Consequently, charge diffusion effects in the "*pp*2*pp* at STAR" experiment can be neglected with high confidence.

Sharing of the charge between two consecutive silicon micro-strips also depends on the impact angles of ionizing particles and widths of the micro-strips. In our experiment, due to very small scattering angles of the scattered particles of interest (high energy protons), it is expected that their trajectories are almost perpendicular to the silicon planes of the detectors. However, the micro-strips are still wide enough so the charge sharing between two strips is still possible to occur. This effect is carefully studied in Chapter 5.1.4. Charge sharing can be used to improve the

position resolution of the detected particles by weighting the individual strip positions with the collected charge by the strips.

The total detector capacitance depends on the thickness of the silicon bulk, the thickness of the oxide layer and the dimension of the micro-strips (length, width). The thickness of the silicon bulk in the "*pp*2*pp* at STAR" experiment is 400 μm, thickness of the oxide layer is about 100 nm. The width of the p-type strips is 70 μm and the width of Al strips is 72 μm. Therefore, the gap between two consecutive strips is 30 μm. The length of the silicon strips is about 80 mm in Y-view detector. This is summarized in Table 2.

TABLE 2. Parameters and dimensions of the Si micro-strip detectors.

Strip width	70 μm
Strip pitch (x-plane, center to center)	97.4 μm
Strip pitch (y-plane, center to center)	105 μm
Resolution = Strip pitch/$\sqrt{12}$	$\sim$ 29 μm
SiO_2 layer	100 nm
p^+ width	70 μm
Al width	72 μm
Wafer thickness	400 μm
C_{wafer}	600 pF/μm depletion
$C_{\text{interstrip}}$	2 nF
C_{coupling}	$\sim$ 2 nF

Two different capacitors, the capacitor formed by the n-type backplane and p-type strip (C_{wafer}) and the capacitor formed by p-type strip and Al strip (C_{coupling}), contribute to the total capacitance of the detector, see Fig. 19. These two capacitors are approximated to be in series, hence the overall detector capacitance can be determined by their equivalent capacitor. C_{coupling} is calculated to be about 2000 pF and C_{wafer} about 1.7 pF which is rather small compared to C_{coupling}. Therefore, the total detector capacitance will be mainly dominated by C_{wafer}. In order to decouple

neighboring strips from each other, C_{coupling} capacitance is required to be much larger than the capacitance between two consecutive strips, $C_{\text{interstrip}}$. In other words, the bigger the C_{coupling} capacitance, the better the charge induction in the Al strip.

3.5.2 PARTICLE DETECTION USING SILICON MICRO-STRIP DETECTORS

As previously explained, when a charged particle passes through a thin silicon layer, it looses energy through ionization. This energy loss can be described by the Bethe-Bloch formula [74]. According to this formula, at relativistic energies, this loss can be considered as constant. Therefore, the energy loss is approximately the same for any particle with relativistic energies.

Energy loss (stopping power) in micro-strip detectors follows a Landau distribution [74]. The most probable energy loss in a thin 400 μm layer of silicon is about 118 keV. In silicon, it takes on average 3.6 eV to create one electron-hole pair. Therefore, a high energy proton will create around 8,200 electron-hole pairs per 100 μm of silicon. The charge equivalent to this is about 1.31 fC which gives around 5 fC signal to be collected by p-type micro-strips, as shown in Fig.20. This will be studied in detail in Chapter 5.

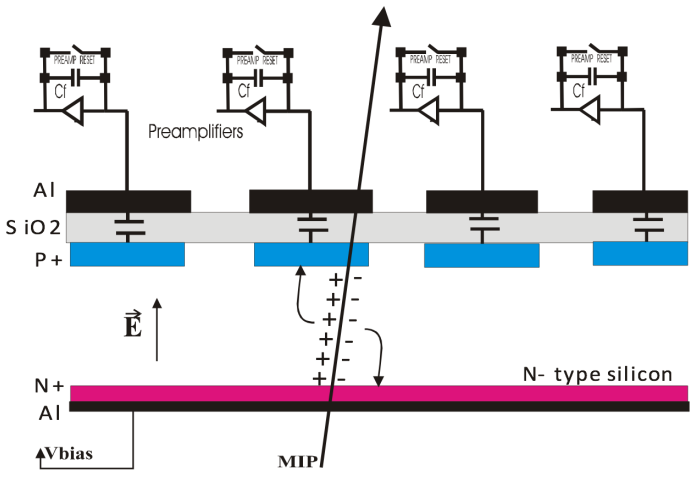

FIG. 20. Signal creation and collection in silicon micro-strip detector [7].

3.5.3 PROBLEMS AND DRAWBACKS OF SILICON MICRO-STRIP DETECTORS

A few problems can be encountered when silicon micro-strip detectors are used. The first among them is damage due to radiation. This is a general problem with all silicon detectors. High radiation can cause displacement of atoms at their lattice site which changes doping concentration in the silicon bulk. This leads to an increasing leakage current. Also, it can cause surface damage due to charge build up at the surface layers which can cause an increase of the surface leakage current and effect inter-strip isolation. In addition, it can cause ineffective biasing and therefore, non-uniform electric fields inside the bulk.

The second drawback with silicon micro-strip detectors is an unreliable oxide layer. This oxide layer can break if the voltage difference applied across it is larger than 10 V. However, this is not a problem for our silicon micro-strip detectors.

Inter-strip capacitance is, also, one of the problems that can occur. As previously stated, the coupling capacitance has to be greater than the inter-strip capacitance. If this is not the case, fake signals could be observed in the neighboring strips of the hit micro-strip. Our system is checked for this and no such effect was detected.

The external electric field of the accelerator environment can cause charge induction on the Al strips leading to surface charge currents. External magnetic fields can cause unexpected deflections in the trajectory of the particle passing through the silicon detector, disturbing the spatial measurement precision. Because of this, the detectors should be protected from external fields.

The silicon detectors used in the "$pp2pp$ at STAR" experiment are designed with a small cutting edge of 500 μm. This is the distance to the first strip closest to the beam, and it is minimized for detecting particles with as small as possible scattering angles. However, the cutting edge of the silicon can be a source of leakage current, which can affect nearby strips. To prevent this effect a guard/bias ring is used around the strips, to serve as a leakage current drain and minimize the inactive area. More details on drawbacks of silicon micro-strip detectors can be found in [7], [74], and [73].

3.6 THE READOUT SYSTEM

The readout system of the silicon micro-strip detectors consists of 160 SVXIIE chips. The SVXIIE chip is a 128 channel device, developed by a collaboration of engineers at FNAL and LBNL [72]. The chip was designed to meet the requirements for both CDF and D0 experiments at FNAL. The SVXIIE chip features a 32-cell analog pipeline, programmable test patterns, downloadable settings for ADC ramp, pedestal, bandwidth and polarity [7]. The SVXII chip is designed for daisy chained operation with silicon strip detectors, to reduce the number of control and readout connections in a multi-chip system [7]. The major characteristics and features SVXIIE chip are:

- 128 channels per chip.
- Designed to accommodate beam crossing time from 132 ns to 396 ns.
- Separate acquisition and readout cycles.
- Double correlated sampling.
- Large dynamic range.
- Programmable depth analog pipeline (32 cell maximum depth per channel).
- Digitization of analog signals to 8 bits of resolution.
- Data sparsification (zero suppression).
- Neighbor channel readout selection.
- Low noise (S/N=10 to 20:1).
- Low power dissipation (approximately 350 mW/chip).
- Operation compatible with doubled sided AC coupled detectors.
- Separate test input for each channel.
- Daisy chain operation capability.
- Parallel bus data readout.

- Numerous programmable internal registers (chip ID, preamp risetime, threshold level, etc.).

For details on design and operation of SVXIIE chips refer to [7].

3.7 MEASUREMENT TECHNIQUE

The incoming beams collide at the interaction region in a local coordinate system at a vertical distance x and y from the reference orbit and are scattered with polar angle θ. The common nomenclature is that the z-axis has been chosen to be the beam axis (usually denoted as the s - axis), while the remaining x and y axes are transverse to the beam (in the following text denoted as the "ξ"), and φ is the azimuthal scattering angle.

Due to small scattering angles, the scattered particles travel inside the beam pipes after the beams collide. They follow trajectories determined by transport matrices of the magnet system until they reach the Roman pot detectors. As previously described, the Roman pots measure the positions of the scattered particles with respect to the reference orbit. Consequently, the parameters of the accelerator lattice can be used to determine the scattering angle θ_ξ^{IP}, and the deflection in the transverse direction ξ^{IP}, at the interaction point. The angle φ_ξ^{IP} between transverse ξ and the scattering plane is arbitrary. Therefore $\theta_\xi^{IP} = \theta^{IP} \sin \varphi_\xi^{IP}$.

The motion of the particle in the accelerator is given with the so called Hill's equation [75],

$$\frac{d^2\xi}{ds^2} + K(s)\xi(s) = 0, \tag{60}$$

where the $K(s)$ from this equation is determined by the accelerator lattice.

The harmonic solution of Eq.(60):

$$\xi(s) = A\sqrt{\beta(s)} \cos\left(\Psi(s) + \lambda\right) \tag{61}$$

gives the transverse displacement as a function of the position (for arbitrary A amplitude and λ) along the s-axis (the accelerator axis). $\Psi(s)$ is the phase given in terms of the beta function $\beta(s)$ as

$$\Psi(s) = \int_{s_0}^{s} \frac{ds'}{\beta(s')}. \tag{62}$$

On the other hand, the angle of the particle trajectory, with respect to the s-axis,

is given as the derivative of the transverse displacement ξ:

$$\theta_\xi(s) \equiv \frac{d\xi}{ds} = -\frac{A}{\sqrt{\beta(s)}}[\alpha(s)\cos(\Psi(s)+\lambda) + \sin(\Psi(s)+\lambda)], \tag{63}$$

where $\alpha(s)$ is the derivative of betatron (beta) function $\beta(s)$,

$$\alpha(s) = -\frac{1}{2}\frac{d\beta}{ds}. \tag{64}$$

The values of the transverse displacement and the angle of the particle trajectory at the detection point, $\xi(s)$, and $\theta_\xi(s)$ respectively, are related to corresponding variables at the interaction point, $\xi^{IP}(s)$, and $\theta_\xi^{IP}(s)$, by:

$$\begin{bmatrix} \xi \\ \theta_\xi \end{bmatrix} = \begin{bmatrix} \sqrt{\frac{\beta}{\beta^*}}\,(cos\Psi + \alpha^*\sin\Psi) & \sqrt{\beta\beta^*}\sin\Psi \\ \frac{(1+\alpha\alpha^*)\sin\Psi + (\alpha^* - \alpha\cos\Psi)}{\sqrt{\beta\beta^*}} & \sqrt{\frac{\beta}{\beta^*}}\,(cos\Psi - \alpha\sin\Psi) \end{bmatrix} \begin{bmatrix} \xi^{IP} \\ \theta_\xi^{IP} \end{bmatrix}, \tag{65}$$

where β is the betatron function, and β^* is its value at the IP ($\beta^* = \beta(s=0)$), α^* is the derivative of the betatron function β^* at the IP , and Ψ is the phase advance from IP. These parameters are sometimes called twiss parameters of the lattice.

In order to measure the scattering angle of the protons, the angle has to be larger than a minimum value denoted as the angular spread of the beam at the IP given by:

$$\sigma_{\theta_\xi^{IP}} = \sqrt{\frac{\varepsilon}{6\pi\beta^*}}, \tag{66}$$

where ε is the normalized emittance. One can see that the larger β^*, the smaller the angular spread of the beam. On the other hand, the larger β^* the larger the beam spot at the IP,

$$\sigma_\xi^{IP} = \sqrt{\frac{\varepsilon\beta^*}{6\pi}}. \tag{67}$$

From Eq.(65), the displacement in the transverse direction ξ at the detector can be written as

$$\xi = \sqrt{\frac{\beta}{\beta^*}}\,(\cos\Psi + \alpha^*\sin\Psi)\,\xi^{IP} + \sqrt{\beta\beta^*}\theta_\xi^{IP}\sin\Psi, \tag{68}$$

and simplified to

$$\xi = a_{11}\xi^{IP} + L_{eff}\theta_\xi^{IP}, \tag{69}$$

where

$$L_{eff} \equiv \sqrt{\beta\beta^*}\sin\Psi, \qquad a_{11} \equiv \sqrt{\frac{\beta}{\beta^*}}\,(\cos\Psi + \alpha^*\sin\Psi)\,. \tag{70}$$

The experiment requires that L_{eff} is as large as possible, and on the other hand, a_{11} as low as possible in order to have the transverse displacement ξ independent of the displacement at the IP, ξ^{IP}, and maximized for the range of scattering angles θ_ξ^{IP}. This is called "parallel to point focusing". The conditions that meet this criteria are when $\sqrt{\beta\beta^*}$ is large, and when Ψ is the odd multiple of $\pi/2$. When these conditions are met, Eq.(68) becomes

$$\xi \cong L_{eff}\theta_\xi^{IP}. \tag{71}$$

From this equation, it is obvious that in this way the value of θ_ξ^{IP} is obtained just by measuring the displacement at the detector alone.

The smallest measurable four-momentum-transfer squared $t_{\min}$ is determined by the smallest scattering angle measured $\theta_{\min}^{IP}$, by:

$$\theta_{\min}^{IP} = \frac{d_{\min}}{L_{eff}}, \tag{72}$$

where $d_{\min}$ is the minimum of the distance detector from the beam center, and it is given by:

$$d_{\min} = k\sigma_\xi + d_0, \tag{73}$$

where k is an accelerator constant determined by the maximum acceptable rate, which is optimized by beam scraping, σ_ξ is the beam size at the detection point, and d_0 is the distance between the beginning of the sensitive area of the detector and the beam side of the Roman pot. In our case, $d_0 \sim 1.8$ mm, so it is not negligible. The smallest measurable four-momentum-transfer squared $t_{\min}$ is given by:

$$|t_{\min}| = \frac{k^2\varepsilon p^2}{\beta^*}. \tag{74}$$

From this equation, one can see that in order to obtain a minimum t, the parameter β^* has to be as large as possible, and parameters ε, and k as low as possible. Large β^* is obtained by adjusting the accelerator "optics", and low ε, and k by careful beam scraping and collimation.

CHAPTER 4

RUN 2009

After many weeks of successful data collection in 2009 (Run9), the STAR collaboration dedicated its final running week to "The Physics with Tagged Forward Protons and the STAR Detector" experiment ("*pp*2*pp* at STAR" experiment). During this last running week, the STAR collaboration was able to measure elastic scattering events at very high precision. In order to have such precision, the angular spread of the beams at the interaction point had to be minimized. This is accomplished by setting special beam optics with a large β-function, see Section 3.7. In addition, the emittance of the beams was drastically reduced by collimator scraping. The optical properties of the transport channel from the IP to the Roman Pot detectors was measured by various methods. In this chapter, we report on the running conditions of the "*pp*2*pp* at STAR" experiment during this final week of the RHIC Run9 as well as on the equipment calibration efforts in order to obtain the most accurate data collection and analysis.

4.1 RUNNING CONDITIONS OF THE "*pp*2*pp* AT STAR" RUN9

During the final week of the RHIC run of 2009 (Run9), the STAR collaboration was able to record a total of 33 million elastic triggers [6]. The data were taken during four dedicated RHIC beam stores, with special beam optics of $\beta^* = 22$ m and luminosity of $\mathcal{L} \simeq 2 \cdot 10^{29}\text{cm}^{-2}\text{s}^{-1}$.

The luminosity of the beam can be calculated using Eq.(75) and Table 5:

$$\mathcal{L} = \frac{3}{2}\frac{\mu}{\beta^*}(\beta\gamma)\frac{N_B N^2}{\varepsilon} \tag{75}$$

where β^* is the betatron function at the IP and μ is the revolution frequency. For 100 GeV protons, $\gamma = 106.8$. N_B is the number of bunches per beam, N is the beam intensity or the number of protons per bunch and ε is the emittance of the beam. For more on the luminosity calculation, refer to [76].

The data were collected in 45 runs during four running days, with the closest

Roman pot approach to the center of the beam pipe at about 10 mm, Fig. 21 . The full list of runs with all the running conditions, i.e. run numbers, number of events taken, number and fraction of elastic events for each run and store number is given in [77]. The list of data sets with Roman pot insertion positions is shown in Table 3. The four momentum transfer squared t range in "*pp*2*pp* at STAR" Run9 was $0.003 \leq |t| \leq 0.035(\mathrm{GeV/c})^2$. A summary of the running conditions, i.e. beam parameters, during Run9 is given in Table 5.

TABLE 3. Roman pot insertion positions (in [mm], from the beam pipe center) of the "*pp*2*pp* at STAR" experiment during Run9. Each insert position combination represents one data set. E - East; W - West; H - Horizontal; V - Vertical; I - Inner; O - Outer.

Set No.	WHI	WHO	WVU	WVD	EHI	EHO	EVU	EVD
0	10.3	10.3	15.4	15.2	10.4	10.6	10.3	10.5
1	8.9	10.3	10.2	10.2	10.2	10.3	5.0	10.3
2	10.2	10.3	10.2	10.2	16.9	17.2	15.9	16.6
3	10.2	10.3	10.2	10.2	14.5	14.7	10.9	12.8
4	6.4	9.0	8.9	8.9	7.6	12.8	7.8	9.6
5	8.9	8.4	10.2	10.2	7.0	7.8	7.1	7.1
6	8.9	8.4	10.2	10.2	8.0	8.8	8.1	8.1
7	10.3	10.3	14.1	11.4	19.5	16.0	16.5	19.1
8	10.3	10.3	15.3	12.6	19.5	16.0	16.5	19.1
9	9.1	9.1	9.6	8.9	8.3	8.3	8.4	8.4
10	9.0	9.8	19.3	16.6	20.1	17.9	17.3	19.1
11	6.5	8.4	10.2	7.0	13.2	10.9	10.3	12.8
12	7.1	8.4	10.8	7.6	13.2	10.9	10.3	12.8

The set of 45 physics runs was analyzed to extract the physics of interest. This entire set belongs to four RHIC beam stores, 11020, 11026, 11030 and 11032 (see Table 4). Each one of these fills had the same bunch structure for both Blue and Yellow circulating beams. Both beams had a fill structure of 120 $\times$ 120 bunches per

TABLE 4. Beam stores (fills), data sets and runs of the "*pp*2*pp* at STAR" experiment during Run9.

Store No.	Set No.	Run No.
11020	0	10181085, 10181086, 10182001, 10182002, 10182004, 10182005, 10182006
	1	10182015, 10182016, 10182021, 10182025
11026	2	10183013, 10183014, 10183015, 10183016, 10183017
	3	10183018, 10183020, 10183021
	4	10183027, 10183028
	5	10183034
	6	10183035, 10183037, 10183038
11030	7	10184016, 10184017
	8	10184018, 10184019, 10184020, 10184021
	9	10184030, 10184031, 10184032, 10184033
11032	10	10185001, 10185002, 10185003, 10185004, 10185005, 10185006
	11	10185018
	12	10185019, 10185022, 10185023

beam (Blue × Yellow). However, 30 bunches were never filled in order to provide an abort gap for the beams. Therefore, the fill structure of the four "*pp*2*pp* at STAR" RHIC beam stores were 90 × 90 bunches per beam. 64 out of 90 bunches per beam had useful polarization combinations where both bunches from Blue and Yellow beams were polarized. This includes four bunch combinations, 16 $\uparrow\uparrow$, 16 $\downarrow\downarrow$, 16 $\uparrow\downarrow$ and 16 $\downarrow\uparrow$ in both Blue and Yellow beams.

The polarization pattern for the Blue beam was: $-+-++-+-$ ..., and for the Yellow beam was: $++-++-$ ..., with 90 × 90 bunches for Blue × Yellow. The polarization measurement during the run was performed by the CNI Polarimeter group at RHIC [78].

Also, the events that came from collisions of the first seven bunches were excluded for the purpose of data analysis. The reason for this is because the timing of these

TABLE 5. Running conditions of the "*pp*2*pp* at STAR" experiment during Run9.

Parameter	Symbol	Value
Beam momentum (Blue)	p_B	100.2 GeV/c
Beam momentum (Yellow)	p_Y	100.2 GeV/c
Beam polarization (Blue)	P_B	0.60
Beam polarization (Yellow)	P_Y	0.62
Beam intensity (No. of protons/bunch)	I_{beam}	$5 \cdot 10^{10}$ protons/bunch
Beam emittance	ε	15π mm mrad
Betatron function at IP	$\beta^*_{x,y}$	22 m
Beam lateral width at IP	$\sigma^{IP}_{x,y}$	701.62 μm
Beam angular divergence	$\sigma^{IP}_{\sigma_{\theta_x,\theta_y}}$	33.36 μrad
Fill pattern (No. of bunches/ring, Blue×Yellow)		120 × 120
No. of filled bunches/ring, Blue×Yellow		
(after excluding the abort gap in the ll pattern)		90 × 90
No. of colliding pairs		64
No. of bunches with both beams Polarized		64
No. of bunches with polarization pattern		
either ↑↑, ↓↓, ↑↓ or ↓↑ for P_B and P_Y , respectively		16
Closest approach of the RPs		
to the center of beam-pipe	d_{min}	∼10 mm ≈ 12 σ_{beam}

bunches corresponded to the time when the preampliers of the SVXIIE readout chips of the silicon detectors were resetting, which had to be done once per revolution of the proton beam. After this reset, it takes a short amount of time for the preamplier output to settle. This resetting occurred during the collision of the first seven bunches.

Fig.21(a) and Fig.21(b) show the total number of elastic triggers collected during the four days of data taking and the number of elastic triggers taken with Roman pots inserted at different distances, as close as ∼6 mm to the beam center, respectively. The "steps" in Fig.21(a) correspond to the time between the four RHIC stores during

Run9, when there was no beam circulating and data taking was stopped.

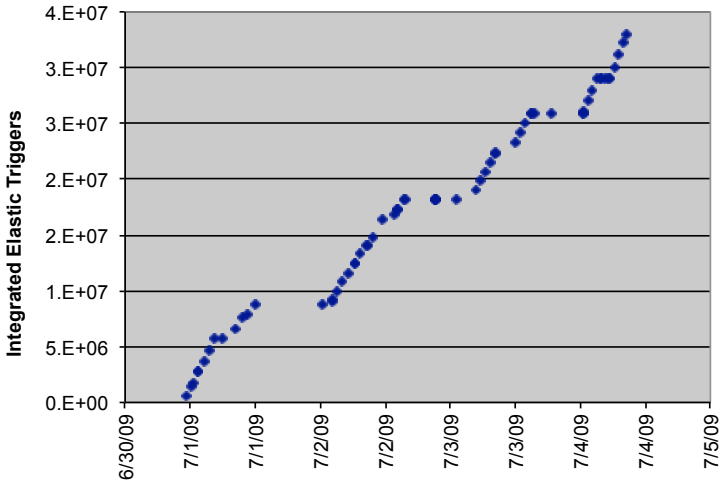

(a) Integrated number of elastic triggers [79].

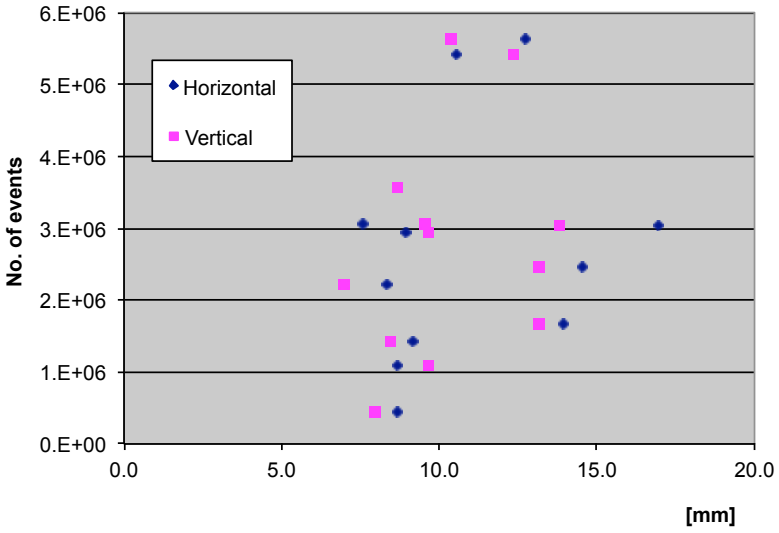

(b) Integrated number of elastic triggers for Roman pot minimum position [79].

FIG. 21. Total number of elastic triggers collected during Run9 (a) and the number of elastic triggers taken as a function of RPs insertion distances (b).

4.2 TRANSPORT MATRICES

Each beam particle can be described by a 6-component space vector $(x, \theta_x, y, \theta_y, E, 1)$, where (x, θ_x), (y, θ_y) are horizontal and vertical coordinates and angles, respectively. E represents the particle's energy and the sixth component is a factor used to add an angular kick on the particle momentum direction. On the other side, each optical element in the beam line, i.e. dipole or quadrupole magnet or a drift space etc., can be described by a 6×6 transport matrix [75]. Furthermore, the beam line from one to another point along the z-axis (s-axis) can be expressed as a single transport matrix, which is the multiplication of the transport matrices of each optical element between the two selected points along z-axis of the beam-line. In other words, a particular beam-line segment or even the whole beam-line along the z-axis can be expressed as a single transport matrix, as given in Eq.(76),

$$M_n = \prod_{i=1}^{n} M_i, \tag{76}$$

where n represents the number of optical elements between two selected points along the z-axis (s-axis).

Therefore, the propagation of a single particle through one segment or the whole beam-line, assuming there are no intra-beam interactions, can be described as the rotation of the phase space vector by one single transport matrix derived from n transport matrices, Eq.(76). This phase space rotation is given by

$$X(s) = \underbrace{\prod_{i=1}^{n} M_i}_{M_n} \cdot X(s = 0), \tag{77}$$

where $X(s = 0)$ is the particle's 6-component space vector at the starting point (usually the interaction point).

The 6×6 matrix of the particle transport can be decomposed into blocks where A and B blocks (2×2) matrices refer to the action (focusing, defocusing, drift) on horizontal and vertical coordinates and angles of the particles, respectively. D terms reflect the dispersion effects of the dipole magnets on off-momentum particles, and

K factors are the angular action of kickers:

$$M = \begin{pmatrix} A & A & 0 & 0 & D & K \\ A & A & 0 & 0 & D & K \\ 0 & 0 & B & B & 0 & K \\ 0 & 0 & B & B & 0 & K \\ 0 & 0 & 0 & 0 & 1 & 0 \\ 0 & 0 & 0 & 0 & 0 & 1 \end{pmatrix} \tag{78}$$

The full 6×6 transport matrices calculated for the special running conditions and beam-line optics between the interaction point and positions of the horizontal and vertical Roman Pot stations, for both Blue and Yellow outgoing beam-lines, during Run9 are given by [80]:

$$TM_{B,H} = \begin{pmatrix} -0.091323718 & 25.256606 & -0.0034073425 & 0.076451454 & 0 & -0.0834729 \\ -0.039643610 & 0.013735315 & -0.00013825484 & 0.005662108 & 0 & 0.0046256554 \\ -0.0032942032 & -0.10011101 & 0.10435091 & 24.759801 & 0 & 0.0027857599 \\ 0.00018576904 & 0.0082935034 & -0.043057022 & -0.63319645 & 0 & -3.3403833e^{-05} \\ 0.0037320072 & -0.11795512 & -8.9159080e^{-05} & -0.001763131 & 1 & 0.0075384334 \\ 0 & 0 & 0 & 0 & 0 & 1 \end{pmatrix} \tag{79}$$

$$TM_{B,V} = \begin{pmatrix} -0.21025431 & 25.297812 & -0.0038221063 & 0.093437746 & 0 & -0.069701292 \\ -0.039643610 & 0.013735315 & -0.00013825484 & 0.005662108 & 0 & 0.0046256554 \\ -0.0027368972 & -0.075230550 & -0.024819895 & 22.860216 & 0 & 0.0029501839 \\ 0.00018576904 & 0.0082935034 & -0.043057022 & -0.63319645 & 0 & -3.3403833e^{-05} \\ 0.0037362315 & -0.11795438 & -0.0001005389 & -0.0019312942 & 1 & 0.0078009082 \\ 0 & 0 & 0 & 0 & 0 & 1 \end{pmatrix} \tag{80}$$

$$TM_{Y,H} = \begin{pmatrix} -0.090388919 & 25.302702 & -0.00010063732 & -0.10865959 & 0 & 0.085060902 \\ -0.03957787 & 0.015879885 & 7.333990e^{-05} & -0.0021584442 & 0 & -0.004574485 \\ 0.0001727273 & 0.051677892 & 0.10617954 & 24.800433 & 0 & -9.8771151e^{-05} \\ -0.0001699380 & -0.003448997 & -0.043026306 & -0.63175279 & 0 & -1.6627775e^{-05} \\ -0.0037799928 & 0.11709879 & 1.1793282e^{-05} & -0.0002058859 & 1 & 0.007531161 \\ 0 & 0 & 0 & 0 & 0 & 1 \end{pmatrix} \tag{81}$$

$$TM_{Y,V} = \begin{pmatrix} -0.20912230 & 25.350341 & 0.00011938194 & -0.11513491 & 0 & 0.071508789 \\ -0.039577874 & 0.015879885 & 7.333990e^{-05} & -0.0021584442 & 0 & -0.004574485 \\ -0.00033708581 & 0.041330921 & -0.02289911 & 22.905178 & 0 & -0.00017832232 \\ -0.0001699380 & -0.003448997 & -0.043026306 & -0.63175279 & 0 & -1.6627775e^{-05} \\ -0.0037867681 & 0.11710162 & 1.308234e^{-05} & -0.0001875129 & 1 & 0.0077933494 \\ 0 & 0 & 0 & 0 & 0 & 1 \end{pmatrix} \tag{82}$$

4.3 CALIBRATION OF THE SILICON DETECTORS

In order to obtain precise position measurements of detected scattered protons with respect to the center of the beam pipeline, it was necessary to perform survey and alignment of the assembled detector packages. This task was successfully performed both in the lab, after they had been assembled, and in the actual setup inside the RHIC tunnel at the end of Run9. The survey and alignment of silicon strip detectors was part of the initial calibration, which was followed by the final micro alignment, done by the use of the elastic events in the overlapping regions of the horizontal and vertical RPs. Furthermore, the micro alignment [81] was followed by a study based on the collinearity of the elastic events and Monte-Carlo simulations of the acceptance boundaries, which are limited by the apertures of the quadrupole magnets in front of the RPs in the outgoing RHIC rings. This study of the acceptance boundaries was used to further constrain the geometry and to finalize the alignment of the silicon detectors.

The information obtained from survey and alignment studies of the detector packages were used to calculate the positions of the 1^{st} silicon strip in each one of the silicon detector planes, with respect to the center of the RHIC beam-line. Also, this information was used to calculate the tilt angles of the detector packages in the $x - y$ plane, as they were positioned inside the RPs during the run.

The survey of the detectors performed in the lab provided information on the positions of the two survey points (tooling balls), with respect to a previously established reference point on the package (the centering pin). The position of the centering pin and corresponding two tooling balls, for each RP package, together with positions of the four cross points on each corner of the silicon detector plane, made by lithography on the silicon during manufacturing, provided the positions of the 1^{st} silicon strip on each detecting plane with respect to the positions of the tooling balls. For the details of this part of the survey, refer to [77].

After the initial survey of the silicon detector packages in the lab, this process was continued on the actual setup in the RHIC tunnel, with the goal of finding positions of the 1^{st} strips of each detector package with respect to the center of the beam pipe-line. The measurements of the positions of the tooling balls, with respect to the center of the beam pipe-line, were performed for each RP in 16 positions, including the one where the RPs are fully retracted ($\sim$ 70 mm from the center of the beam pipe-line). The displacements from the fully retracted positions of the RPs

were measured by using Linear Variable Differential Transformer (LVDT), a position measuring device installed inside the RHIC tunnel. Precisions of these measurements were of the order of 30 μm.

The possibility of the existence of angles of tilt for each detector package in the $x-y$ plane comes from the fact that each detector plane within each detector package of the RP can be slightly tilted relative to the package itself and furthermore, each package can be slightly tilted relative to the $x-y$ RHIC coordinate plane. Therefore, the final tilt angle is the sum of these two tilts.

A tilt of each detector package relative to the RHIC $x-y$ coordinate plane is calculated as an average tilt calculated for all surveyed LVDT Roman Pot positions. These calculated numbers (tilt angles) are expected to be constant regardless of LVDT positions of the Roman Pots. The table of calculated final tilt angles for all detector planes in the RHIC $x-y$ plane is given in Table 6. For the details of this calculation, refer to [77].

TABLE 6. Calculated final tilt angles for all detector planes in the RHIC $x-y$ plane.

	Plane A Tilt Angle (mrad)	Plane B Tilt Angle (mrad)	Plane C Tilt Angle (mrad)	Plane D Tilt Angle (mrad)
EHI	1.803	1.803	1.903	1.903
EHO	-0.659	-0.659	-0.759	-0.659
EVU	0.366	0.566	0.466	0.466
EVD	-2.041	-2.041	-2.041	-2.041
WHI	-0.896	-0.996	-0.896	-0.796
WHO	0.607	0.507	0.507	0.607
WVD	1.320	1.420	1.420	1.220
WVU	-2.472	-2.472	-2.472	-2.572

By using all the information above, both survey measurements and final tilt angles calculations, one can calculate positions x_0 and y_0 of the 1^{st} silicon strip in all the detector planes and their relation with the LVDT positions of the RPs [77]. For

planes A and C, in order to get these positions, one can use the given linear relation between the calculated x_0 and y_0 and the LVDT position for each $pp2pp$ run number during Run9 (see [82]). On the other hand, for planes B and D, the calculated x_0 and y_0 is the same for all the runs and are, also, given in [77].

The information about the techniques related to micro-alignment (global and local alignment) can be found in [81].

CHAPTER 5

DATA ANALYSIS

The analysis was carried out on data taken during the 2009 RHIC run. The "pp2pp" experiment had five days of dedicated running time with special beam optics (see Chapter 4), during which, ∼33 million elastic triggers were recorded. The full data sample was recorded in 45 runs which can be grouped into 12 different "sets" or into four different "beam stores". Each one of the "sets" corresponded to one "set" of the Roman pots' positions and each"beam store" corresponded to one RHIC beam fill (store).

The main objective of this analysis is to obtain forward scattering parameters, the nuclear slope B in particular, through elastic scattering of polarized protons at $\sqrt{s} = 200$ GeV and $0.003 < |t| < 0.035$ $(\mathrm{GeV/c})^2$.

This chapter will address several key objectives in the process of obtaining forward scattering parameters from recorded data: reconstruction of tracks from the raw data, selection of elastic events, assigning kinematic parameters $|t|$ and φ and calculating forward scattering parameters.

5.1 ELASTIC TRACK RECONSTRUCTION

The track reconstruction procedure can be performed in several stages. The first stage starts at the strip/channel of the silicon micro-strip detector level. At this level, the performance of the detector must be analyzed in detail. The next stage in the analysis process is at the level of "clusters". An elastically scattered proton detected by the silicon detector, may deposit its energy in several neighboring silicon strips of the hit strip. A cluster is a set of consecutive strips with an ADC read out value above a certain threshold. Clusters represent real particles, and by analyzing characteristics of clusters one can eliminate events that do not satisfy requirements of the elastically scattered protons which are of interest in this study. The third stage of track reconstruction procedure is at the level of Roman pot where tracks are being tested whether they satisfy conditions of being an elastic event or not. The final stage is the calculation of physics quantities and their analysis.

5.1.1 PEDESTALS AND NOISE OF SILICON DETECTOR

The pedestals and noise level study plays a very important role in this analysis. It characterizes the detector performance and provides a threshold value that needs to be subtracted from the measured signal in order to eliminate the part that comes from the noise. Because this study plays such an important role, several data taking periods of about 10,000 inelastic events, during Run 2009, were dedicated only to this purpose.

There are ∼20,000 channels within the total of 32 detector planes (see Chapter 3), that must be studied for pedestal and noise levels. A distribution of pedestals and pedestal-σ values for one of the 32 detector planes, is shown in Fig. 22.

The definition of the pedestal value is given with the following equation:

$$P_{kj} = \frac{1}{N}\sum_{i=0}^{N} ADC_{ikj}, \tag{83}$$

where P_{kj} is the pedestal value for the j^{th} channel and k^{th} SVXIIE chip (see Chapter 3), ADC_{ijk} represents ADC value for the i^{th} event, j^{th} channel and k^{th} SVXIIE, and N is the total number of events.

On the other side, noise is defined as the root mean square (RMS) value of all ADC counts and is represented with:

$$\sigma_{kj} = \sqrt{< ADC_{ikj} - P_{kj} >_i^2}. \tag{84}$$

The total noise is defined as a sum of white noise and so called common mode noise:

$$\sigma_j^2 = \sigma_{wj}^2 - \sigma_k^2, \tag{85}$$

where σ_{wj}^2 is the white noise.

The common mode noise is the RMS value for the distribution of average ADC per SVXIIE chip and is represented with:

$$a_{ik} = \frac{1}{M}\sum_{j=1}^{M=126} ADC_{ikj}, \tag{86}$$

where M is the total number of channels per one SVXIIE chip and in the case of our experimental setup equals 126. In Eq. (85), σ_k^2 represents the RMS value for k^{th}

SVXIIE chip and is given by:

$$\sigma_k^2 = \frac{1}{N}\sum_{i=1}^{N} a_{ik}^2 - \left(\frac{1}{N}\sum_{i=1}^{N} a_{ik}\right)^2. \tag{87}$$

An example of pedestal mean values and noise for each individual strip within one RP detector plane is presented in Fig. 22.

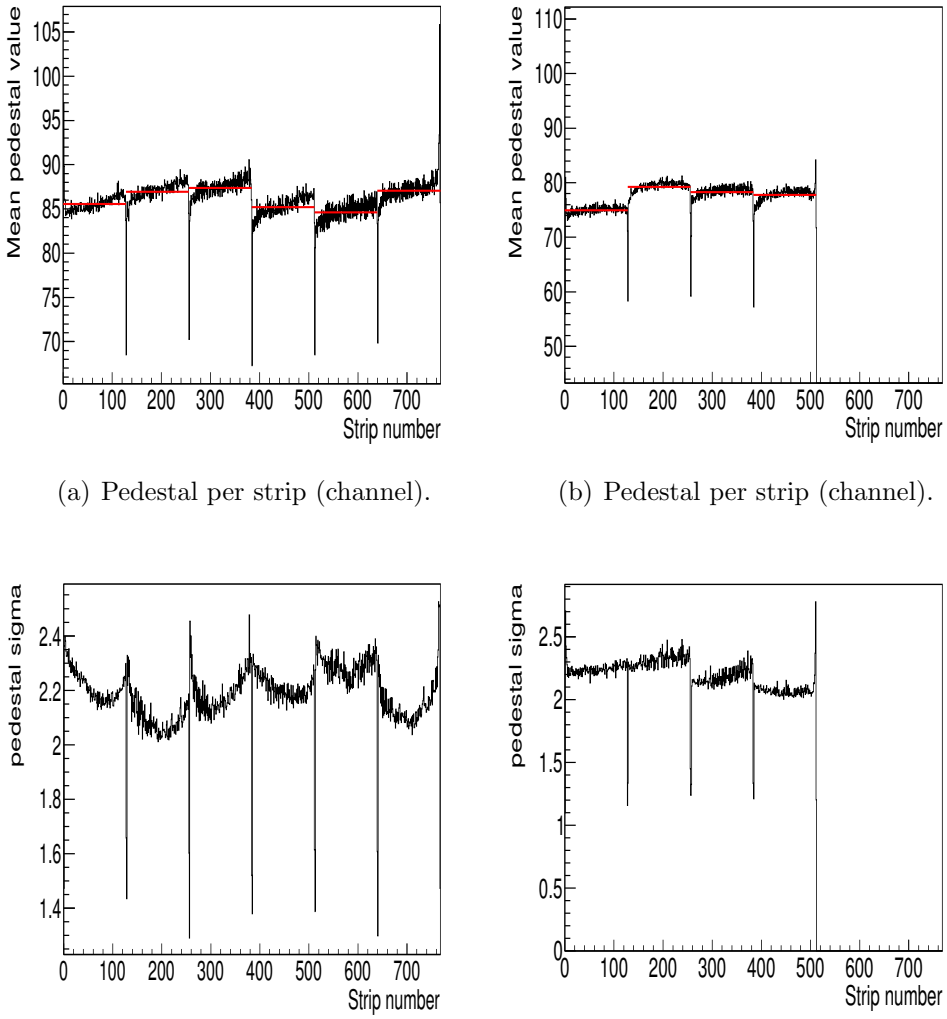

(a) Pedestal per strip (channel).

(b) Pedestal per strip (channel).

(c) Pedestal-σ per strip (channel).

(d) Pedestal-σ per strip (channel).

FIG. 22. Representation of pedestal and pedestal-σ vs. strip (channel) number for one silicon detector plane, i.e. B and D: x-view (6 SVXIIE chips) or A and B: y-view (4 SVXIIE chips) detector planes. The red lines represent relative average pedestal values of SVXIIE chips.

5.1.2 THRESHOLD

Finding an optimal threshold value in the process of hits selection is of great importance. It enables us to distinguish between the hits of interest and noise. Its purpose is elimination of all the noise without affecting the real signal. The threshold value is defined by:

$$T_{kj} = P_{kj} + n \cdot \sigma_{kj}, \tag{88}$$

where T_{kj}, P_{kj} and σ_{kj} are threshold, pedestal and noise (RMS value of ADC counts) values for j^{th} strip and k^{th} SVXIIE chip, respectively. Optimization of threshold values is performed by finding the optimal value for the "sigma cut" coefficient n in Eq. (88). In order to find the optimum n values, in other words optimum pedestal-σ cut, for determining the best signal to noise ratio, values of n = 3, 4, 4.5 and 5 were studied carefully [83] and [84].

It was found that the optimum signal to noise ratio was obtained for n=5 [84]. Applying this threshold cut allowed elimination of about 96% of the total noise from the sample. The remaining 4% of the total noise was eliminated by applying complementary energy cuts (see Section 5.1.5).

5.1.3 CLUSTERS

As previously mentioned, elastically scattered protons detected by the silicon micro-strip detector are represented by clusters. A cluster is defined as a set of consecutive micro-strips with an ADC value above threshold (see Section 5.1.2). Every cluster is characterized by three observables: size (length), energy and position. These three observables provide all the information about the particle and its track.

The size (length) of the cluster

Due to very small scattering angles of the scattered particles of interest, it is expected that their trajectories are almost perpendicular to the silicon planes of the detectors. This has the consequence of very limited cluster sizes (lengths). Therefore, it is expected that clusters that come from real events are not larger than a few strips.

The size (length) of the cluster gives the information about the number of consecutive silicon micro-strips of the detector which had an ADC read out value above threshold.

The energy of the cluster

The energy of the cluster is the total energy deposited by a particle in the material of the detector. The energy loss of the particle in the material of the detector is well described by the Landau distribution.

The position of the cluster

The position of the cluster is defined as the weighted average:

$$\bar{x} = \frac{\sum_{i=1}^{N} x_i E_i}{\sum_{i=1}^{N} E_i}, \tag{89}$$

where i is the strip index and N is the number of strips in the set that forms the cluster, i.e., cluster size (length). x_i is the position of strip i and E_i is its collected energy minus threshold (ADC read out value).

5.1.4 CLUSTER SIZE

As previously stated, scattered protons have trajectories almost perpendicular to the silicon strip planes of the Roman pot detector. This is due to very small scattering angles of the scattered protons. Therefore, it is expected that clusters have lengths of no more then a few strips. Cluster sizes were checked and it was found that in order to select good clusters (clusters that come from good events), it is sufficient to introduce a cut that will remove all the clusters that do not have lengths of less than or equal to five strips from further analysis. This, however, does not imply that clusters with lengths greater than five can not be good events. Instead, as shown in Fig. 23, the likelihood of having clusters with lengths greater than five is very small compared to the number of particles with lengths equal to 1 or 2. Fig. 23 represents the number of clusters with different lengths.

Fig. 23 shows that clusters with lengths of five or more strips make $< 0.5\%$ of the total number of clusters recorded in run 2009. This figure also shows that most of the clusters have lengths of one or two strips.

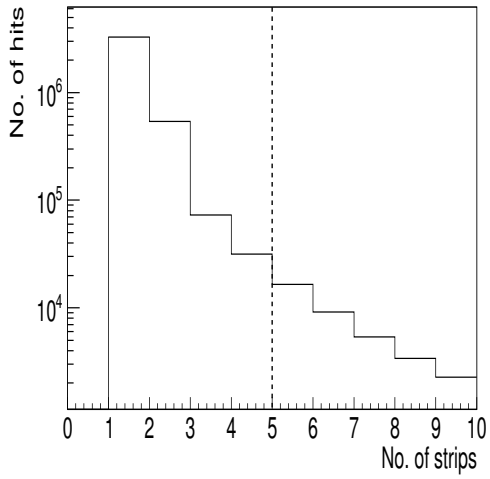

FIG. 23. Distribution of the size/length of clusters (in number of strips).

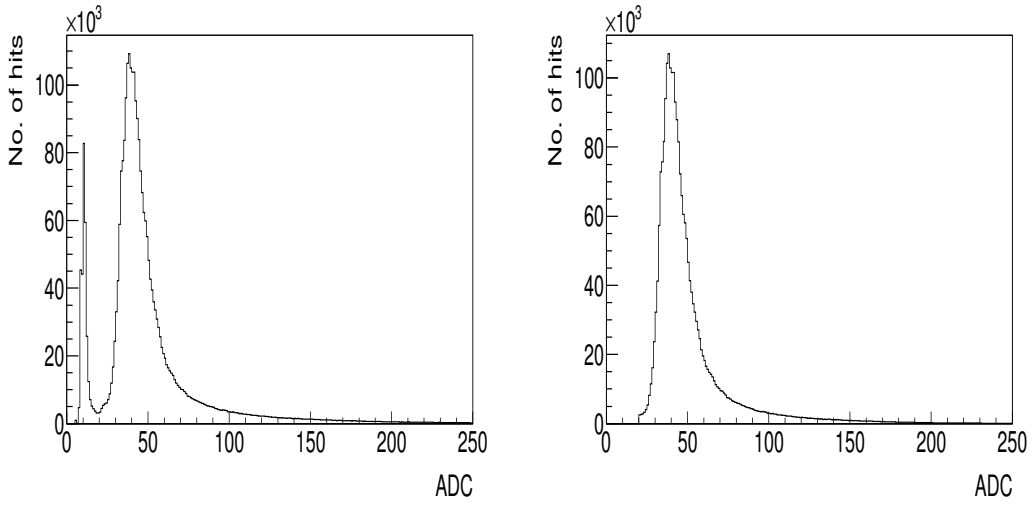

(a) E with the noise peak.

(b) E without the noise peak.

FIG. 24. A sample cluster energy distribution (Landau distribution) in a silicon strip detector. The energy is the sum of the deposited energy above threshold ($T_{kj} = P_{kj} + 5\sigma_{kj}$ subtracted) in all adjacent strips for clusters with lengths $\leq$5.

5.1.5 CLUSTER ENERGY AND FURTHER NOISE REDUCTION

When particles move through the detector, they deposit certain amount of energy in the silicon micro-strip detectors (see Chapter 3). The total energy deposited in the material of the detector is described by a Landau distribution. A sample energy distribution for one of the Roman pot detectors is given in Fig. 24.

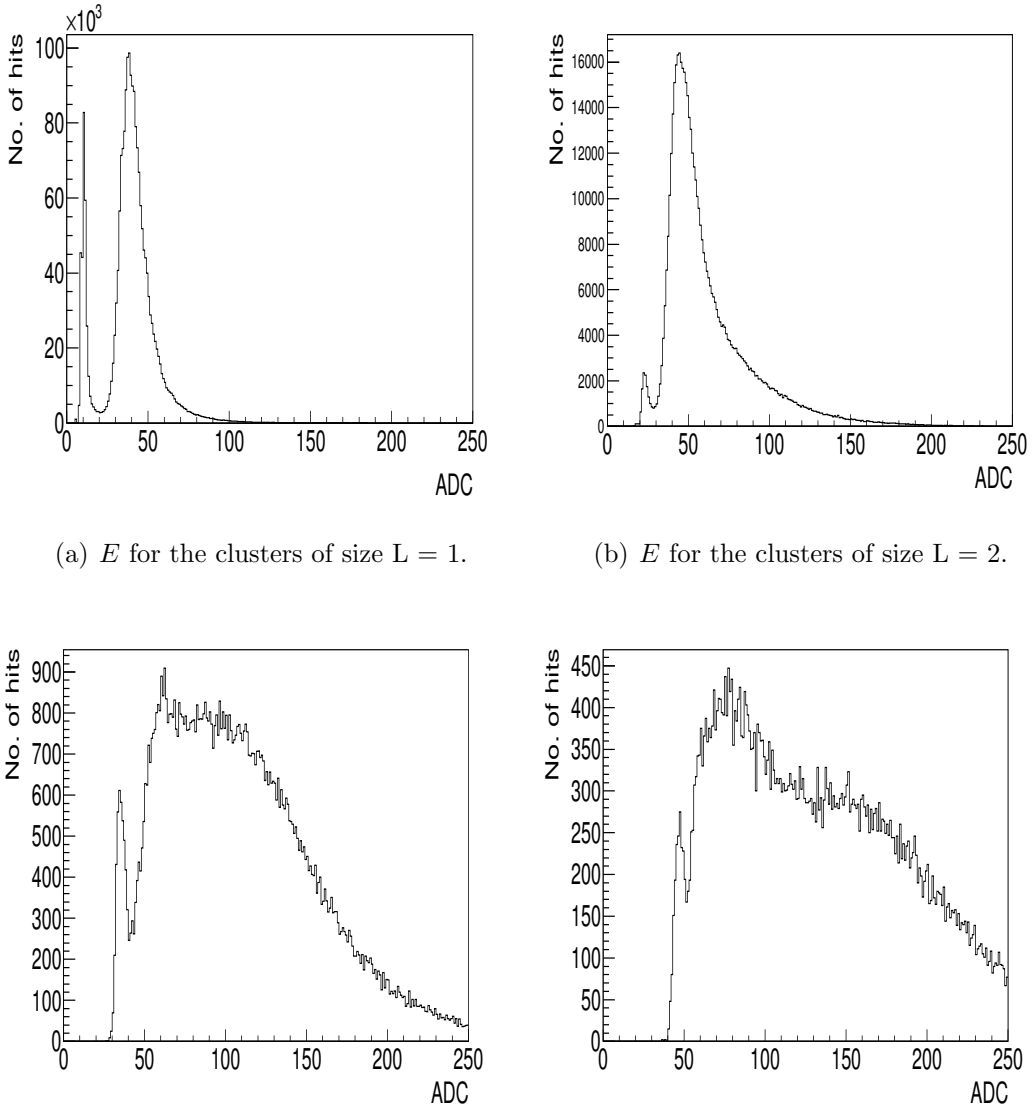

(a) E for the clusters of size L = 1.

(b) E for the clusters of size L = 2.

(c) E for the clusters of size L = 3.

(d) E for the clusters of size L = 4 and 5.

FIG. 25. Energy distribution for the clusters of size L = 1, 2, 3 and 3<L≤5.

The plot in Fig. 24(a) shows, besides the signal of Landau shape, a peak that is well separated from the Landau distribution and is located at low ADC count values. This peak represents the noise or the background that remained after the threshold cut was introduced. Due to this, a minimum energy cut, $E_{\min}$, needed to be introduced in order to remove the remaining noise/background. This cut is complementary to the threshold cut introduced in Section 5.1.2. In fact, it represents a "backup" if in any case, the threshold values are not set correctly.

This cut was obtained by finding minimum ADC count values between Landau distribution and noise/background peaks. This was repeated for different cluster sizes because the energy distribution varies with cluster size and has the tendency of shifting towards higher energy values for higher cluster lengths.

Figure 25 shows energy distributions for the clusters of length L = 1, 2, 3 and $3<L\leq5$.

Clusters of size 1 and 2 show clearly separated Landau distributions and noise peaks. These distributions were used to determine the $E_{\min}$ cut value. The $E_{\min}$ value was set such that it removed no more than 0.2% of all the events. Analysis shows that these values can be applied to all silicon planes in the detector package and that they vary between Roman pot detectors. The full list of all $E_{\min}$ cuts for all Roman pot detectors is shown in Table 7 [1].

TABLE 7. Energy threshold based for different Cluster Size/Length and for each Roman pot [1].

RP/cls length	EHI	EHO	EVU	EVD	WHI	WHO	WVD	WVU
1	19	18	18	19	20	23	21	19
2	27	24	28	28	27	29	29	25
3	49	45	48	50	50	53	46	46
4 and 5	65	60	69	70	60	64	60	59

Even with these and previous cuts, there is still a background in the data sample. This requires additional studies on the properties of the clusters.

5.1.6 NUMBER OF HITS PER PLANE

Further background reduction can be done by limiting the number of clusters accepted per event. In an ideal case, due to the nature of an elastic event, there would be only one cluster (particle) in each of the detector's silicon planes. However, this does not always happen. It was found that about 86% of the events were ideal[1]. The remaining ∼14% of events had more than one cluster per detector's silicon plane. This was mainly due to breakup of protons during interaction with materials of the detectors (see Chapter 6) and background that was still present after previous noise/background elimination efforts. Fig. 26 shows distribution of number of clusters in one Roman pot silicon detector plane.

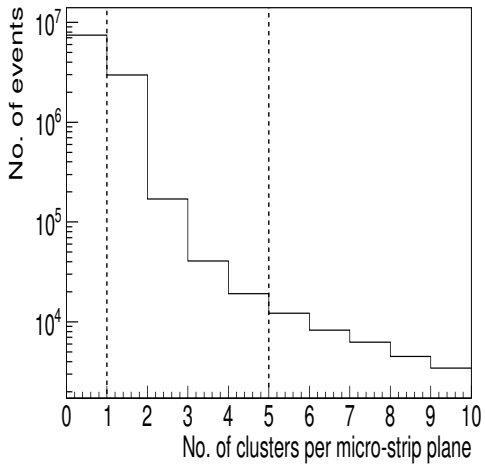

FIG. 26. Distribution of the number of clusters in one silicon micro-strip plane. The first bin shows the number of events when no particle was detected by the shown detector plane. However, in that case, it is most likely that the particle was successfully detected in another arm.

The distribution quickly falls and the fraction of events with more than 5 clusters per silicon plane is as low as ∼0.5% of the number of events shown on the plot.

[1] "Golden events" (Events with one cluster per detector's silicon plane that met all required conditions)

In order to further reduce the background, in the case of events with more than 5 clusters per detector's Si plane, particularly problematic planes were excluded from analysis of that specific event and the corresponding redundant silicon plane was used instead. The installation of redundant Si detector planes was done to address this type of events. Most probable reasons for the number of hits per plane exceeding 5 is the detection of particles of the beam halo (background) or showers of particles caused by proton interactions with detector materials (see Section 6). Each of the five hits that remained in the data sample was studied by applying "matching" condition (Section 5.1.10) after which, only one hit (cluster) remained to be tested for co-linearity.

5.1.7 SILICON STRIP/CHANNEL ANALYSIS

In this analysis, it was very important to retrieve the exact positions of scattered protons.

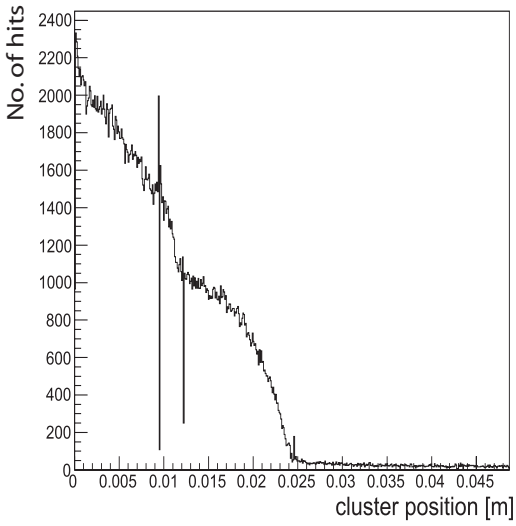

FIG. 27. Particle position distribution illustrating several malfunctioning strips in the silicon micro-strip detector plane.

As previously explained, protons are represented by clusters that have certain characteristics (size, energy, etc.). The size of clusters is the measure of how

many strips/channels of the Si detector planes had an ADC read out value above a certain threshold. By knowing the exact positions of the strips/channels inside the detector package with their ADC read out values, one can easily determine the cluster positions using Eq. (89), and hence the position of the scattered protons. To successfully do that, the condition of each Si strip/channel was checked for proper operational condition and possible malfunctions. There were a total of 20,160 channels used in this experiment and each one of them was checked for proper running condition. Various strip/channel malfunctions are caused by extensive radiation over time or by mechanical damage.

TABLE 8. Malfunctioning strips in the "*pp*2*pp*" Run9.

Detector (Plane)	Strip Number
EHI (A)	252 - 254
EHO (A)	219
EHO (B)	100 - 103
EHO (C)	475 - 485
EVU (A)	98-100, 249, 441
WHI (A)	49 - 51
WHI (C)	442
WHO (B)	744 - 749
WHO (C)	496 - 498
WVU (A)	497, 503, 504

First, hit position distributions for every Si micro-strip detector plane were analyzed. A sample plot of such distribution is shown in Fig. 27.

This particular analysis was focused on finding bad channels. Bad channels are characterized by very high occupancies ("hot" channels) or no occupancies ("dead" channels). By analyzing position distributions of accepted clusters for all Si micro-strip detectors, 40 "hot" and "dead" channels were found. Data that came from these channels/strips were designated as not reliable and they were excluded

from further analysis. Even though the number of malfunctioning strips was small compared to the overall number of strips, they still affected the efficiencies of Roman pot detectors (see Section 5.1.12). The list of all bad channels from "*pp*2*pp*" Run9 are listed in Table 8.

5.1.8 SIGNAL TO NOISE RATIO

Proper working condition of Si strip detectors can be also checked by calculating the ratio of the most probable energy loss value represented by Landau energy loss distribution (see Section 5.1.5) E_{mp} and the value of the total noise σ:

$$SNR = \frac{E_{\mathrm{mp}}}{\sigma}. \tag{90}$$

The most probable value of energy loss E_{mp} and the total noise σ values from our experiment are 41 ADC and 10 ADC counts respectively. Therefore the signal to noise ratio in our experiment was about 4:1 (see Fig. 24). Another analysis of the signal to the total noise ratio from the "*pp*2*pp*" experiment is presented in [84].

5.1.9 TRIGGER CONDITIONS

The positions of the particles coming from real elastic events are measured by two co-linear and opposite Roman pot detectors which are positioned symmetrically around the STAR interaction point (IP). In order to select real elastic events, a condition which checks that both scattered particles were detected by detectors symmetrical around the IP was implemented. Besides four silicon detecting planes that detected positions of the elastically scattered protons, there was a scintillator in each of the Roman pot detector packages connected to two photo multiplier tubes (PMT) which checked if detector was hit by particles.

Since there were a total of eight Roman pots in the experiment (16 PMTs), 16 signals were delivered to the STAR triggering system. Both amplitude and timing information was recorded for each of the 16 PMTs.

A Roman pot "triggered" if either one of its two PMTs recorded a signal that had proper timing and amplitude above the pedestal [83]. Elastic trigger was determined by requiring that there is one proton detected on both sides of the IP and nothing else. The definitions of "allowed" Elastic Arms are given in Table 9.

TABLE 9. Definition of elastic trigger arms.

Elastic trigger arm	RP combinations
EA (Elastic Trigger A - vert.)	(WVU and not WVD) and (EVD and not EVU)
EB (Elastic Trigger B - vert.)	(WVD and not WVU) and (EVU and not EVD)
EC (Elastic Trigger C - horiz.)	(WHO and not WHI) and (EHI and not EHO)
ED (Elastic Trigger D - horiz.)	(WHI and not WHO) and (EHO and not EHI)

Also, there were combinations of triggered Roman Pots that were "forbidden". Those triggering combinations were vetoed and corresponding events were removed during the event reconstruction procedure, Table 10.

TABLE 10. Definition of "forbidden" triggers.

Forbidden trigger	RP combination
EHF (East Horiz. Forbidden)	(EHI and EHO)
EVF (East Vertic. Forbidden)	(EVU and EVD)
WHF (West Horiz. Forbidden)	(WHI and WHO)
WVF (West Vertic. Forbidden)	(WVU and WVD)

As previously stated, whether Roman pots triggered or not was determined by checking the amplitude (ADC signal) and timing (TAC signal) levels. The ADC (Analog to Digital Converter) threshold level for the scintillator trigger counters was determined and set to be equal to 5, ($ADC_{ij} \geq 5$), [83]. The range for the TAC (Time to Analog Converter) signal of the trigger counters was determined to be $100 \leq TAC_{ij}$ signal ≤ 1700, where index i determins the Roman pot Id and index j corresponds to PMT number within i^{th} Roman pot. Only after the ADC and TAC threshold limits are met, are the conditions from Tables 9 and 10 checked. Examples of TAC and ADC plots for one of the triggered Roman pot arms are shown in Figs. 28(a) and 28(b).

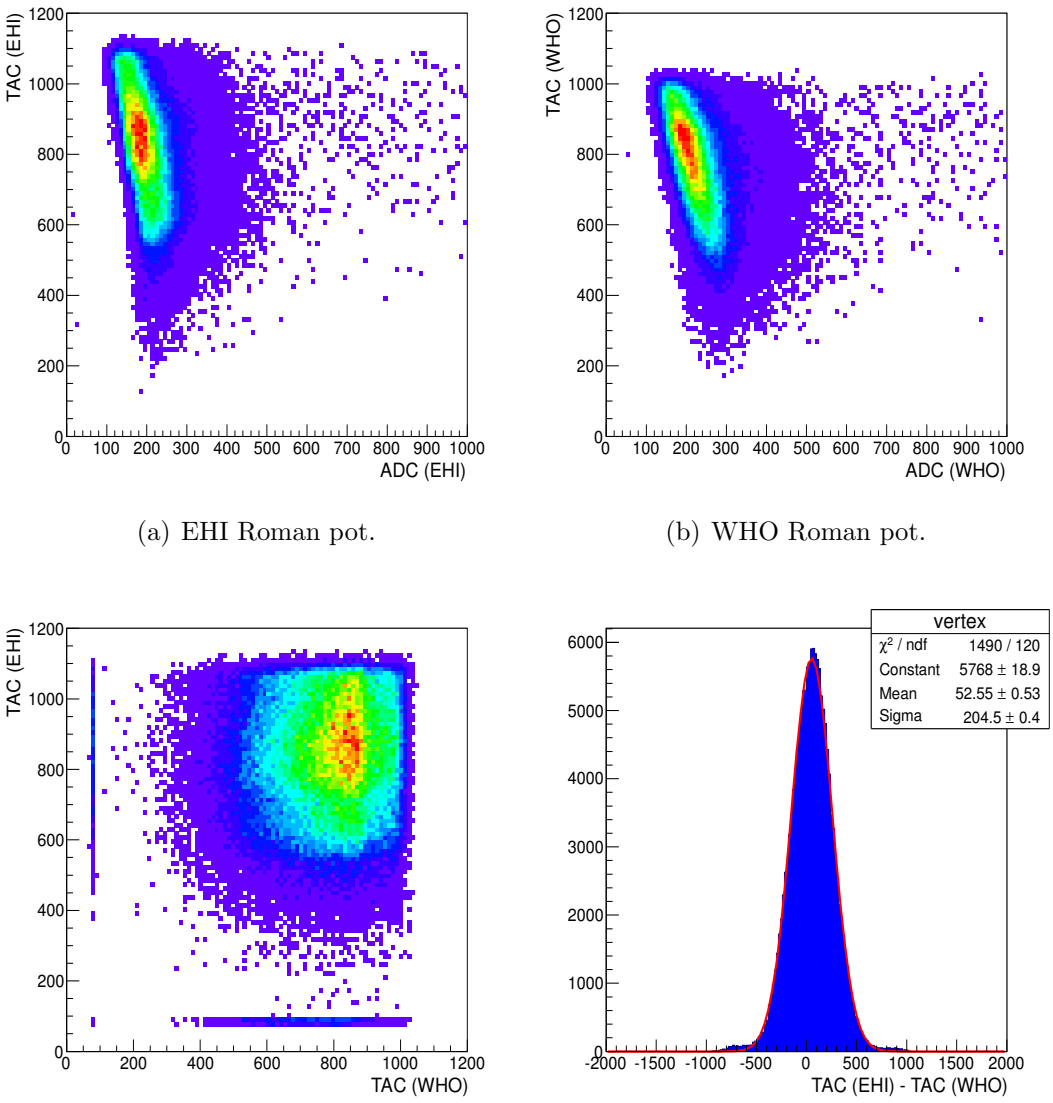

(a) EHI Roman pot.

(b) WHO Roman pot.

(c) EHI-WHO Roman pot arm.

(d) IP s-axis position from TACs.

FIG. 28. TAC vs. ADC signals for the EHI (a) and WHO (b) Roman pots. Elastic events can be seen as a bright spot in the TAC for EHI vs WHO (c). The time difference is shown in (d).

Figs. 28(a) and 28(a) show TAC vs. ADC signals for the EHI and WHO Roman pots respectively . Since "*pp*2*pp*" TACs were set with a "common stop" [12], higher TAC signals corresponded to the faster particles. Having this in mind, one can notice

from Figs. 28(a), 28(b) and 28(c) that particles detected by the EHI Roman pot were slightly faster than their corresponding co-linear particles detected by WHO Roman pot. This indicates that the interaction point (IP) was not positioned at the $s = 0$ position which becomes obvious from Fig. 28(d). The mean value of Gaussian fit on this Figure is equal to 50 TAC units which corresponds to roughly 0.14 m (1 TAC unit = 18 ps).

The triggering setup of the "*pp*2*pp* at STAR" experiment plays a very important role in the elastic data analysis, mainly because it largely contributes to the systematic uncertainties on the event loss and selection process. Therefore, a careful study is needed in order to understand timing (TAC), collected charge (ADC) signals and trigger setup in general [12]. This detailed study is presented in Sections 6 and 8.

5.1.10 CLUSTER MATCHING

In order to increase the efficiency for detecting protons (see Section 5.1.12) and further reduce background, detectors were built from four detecting silicon planes. Two of them measure particle x-coordinates and the other two particle y-coordinates in the local coordinate systems relative to each of the detecting planes (see Chapter 3). In an ideal case, every particle will deposit some energy in each of the detectors' silicon planes (see Section 5.1.5) and will, therefore, have both sets of local coordinates determine its local positions. In an ideal case these two pairs of coordinates will give exactly the same local proton position. Consequently, the matching check of these coordinate pairs is very important when dealing with real data samples that are, naturally, not ideal. Applying this condition helps in distinguishing between clusters that come from real events and clusters that come from background. However, background particles can still make tracks which satisfy this condition. It is estimated that the number of background particles which satisfy the matching check is small. Thus, further checks are needed.

The matching algorithm is as follows. Positions of clusters from redundant planes (A(B) and C(D)) were checked whether they satisfy:

$$\left|(x_1; y_1)_{A(B)} - (x_2; y_2)_{C(D)}\right|_{RP} \leq 2 \cdot \text{strip pitch}, \tag{91}$$

where strip pitch is the distance between centers of two consecutive strips (in X-type detector equals 105 μm and in Y-type detector 97.4 μm).

However, before this condition was checked, redundant planes were examined for their number of clusters in an attempt to extract every good elastic event from the data sample. There are four pairs of redundant micro-strip detector pairs from which cluster coordinates were matched and then extracted. In order to call the event an elastic event, a single coordinate is needed to be obtained from each of the four micro-strip detector pairs (both x and y coordinates on both sides of the IP). Positions of clusters were matched based on the algorithm presented in Table 11. This algorithm is independently applied to all Roman pots from any triggered detector arm on both sides of the IP.

TABLE 11. Cluster matching algorithm.

Case	$N_{cls}(A;B)$	$N_{cls}(C;D)$	position
0	0	0	NA
1	0	1	$(x;y)_{(C;D)}$
	1	0	$(x;y)_{(A;B)}$
2	0	>1	NA
	>1	0	
3	1	1	$(x;y)_{ave} = \frac{(x;y)_{(A;B)}+(x;y)_{(C;D)}}{2}$
4	1	>1	$(x;y)_{ave}$ using min $\lvert\Delta(x;y)\rvert$
	>1	1	
5	>1	>1	$(x;y)_{ave}$ using min $\lvert\Delta(x;y)\rvert$

The differences between two sets of coordinates of the same kind were observed and cluster positions difference plots were produced. Plots for these differences for East Horizontal Inner (EHI) Roman pot are shown in Fig. 29.

The plots in Fig. 29 show that differences in particle positions between corresponding planes are in most cases within 200 μm, which is equal to the width of two Si strips. The number of events with position differences between coordinates of corresponding planes that were above 200 μm represents 0.1% of the total data sample and were excluded from further event reconstruction procedure because they

do not originate from the same event. The plots in Fig. 29 clearly show one or two distinguished peaks. The difference between those peaks is equal to the distance between two strips within the same Si detector plane. Having one or two of these peaks on these plots also serves as a check of how well two Si micro-strip detector planes within the same detector package overlay each other. In other words, the difference between n^{th} strip of one Si detector plane and n^{th} strip of the other, corresponding, Si micro-strip detector plane serves as a good check of how well the detector package was assembled. However, one needs to note here that it is quite difficult to achieve 10μm level precision in alignment of two independent detector planes during the detector assembly process. In fact, this was never intended in the first place due to the fact that it is easy to correct this lack of precision by determining and applying corresponding offsets after the end of experimental measurements and during the event reconstruction procedure.

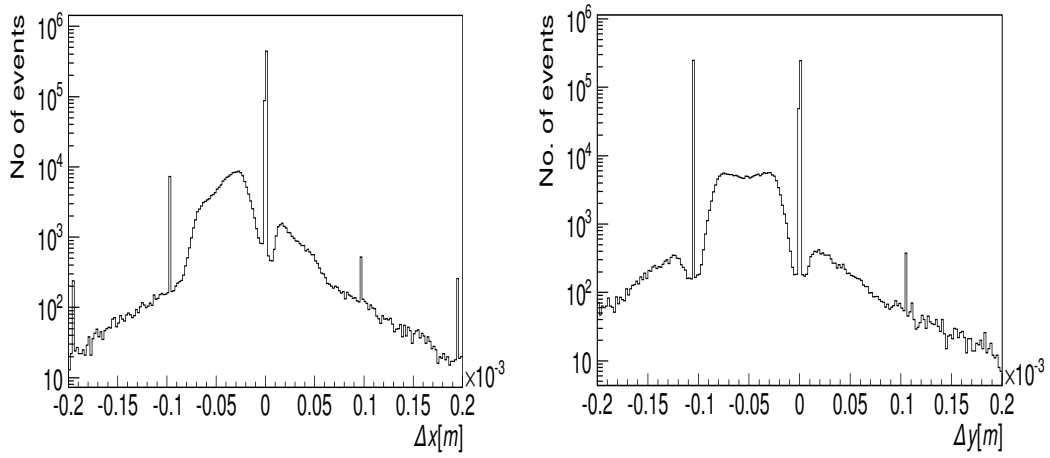

(a) Δx(EHI). (b) Δy(EHI).

FIG. 29. Position difference in [m] between two corresponding, redundant x and y planes within one Roman pot before application of the "cluster matching" condition.

Also, one can notice a clear off-zero shift for these distributions. These shifts occur as an artifact of several procedures for detectors' alignment and clusters' positions

calculations in the "global" (RHIC) coordinate system with respect to the center of the beam pipeline. To successfully perform the cluster matching procedure, they need to be taken into account. The table of the shifts used in the cluster matching procedure is given in Table 12.

TABLE 12. Silicon detector planes offsets.

RP/offset	EHI	EHO	EVU	EVD	WHI	WHO	WVD	WVU
δx [μm]	17	-1	-34	0	-4	-19	-61	-41
δy [μm]	41	-46	-28	7	-63	30	7	-2

After confirming the condition from Eq. (29), positions of the particles were found as an average value according to Table 11 from all four silicon micro-strip detector pairs.

5.1.11 CO-LINEARITY OF ELASTICALLY SCATTERED PROTONS

Due to the nature of elastic events, elastically scattered particles should have the same scattering angles. Hence, positions of particles that come from the same elastic event are measured by two opposite, co-linear detectors, symmetrical with respect to interaction point (IP). The difference between scattering angles at IP of co-linear particles should be close to zero. Scattering angles were calculated from the transport equations (see Section 3.7) and their differences were analyzed. A sample distribution of scattering angle at IP differences fitted with Gaussian fit is shown in Fig. 30.

The plots in Fig. 30 show that differences in scattering angles of elastically scattered protons are in most cases within 3.5σ of Gaussian distribution fit. The number of events with co-linear scattering angle differences bigger than 3.5σ of the fitted Gaussian mean represent about 15% of the total data sample and were excluded from further analysis. The mean values of these differences show offsets from zero. It is crucial to correct for these offsets before applying any co-linearity cuts. The plots in Fig. 30 show differences in scattering angles before these offsets were corrected.

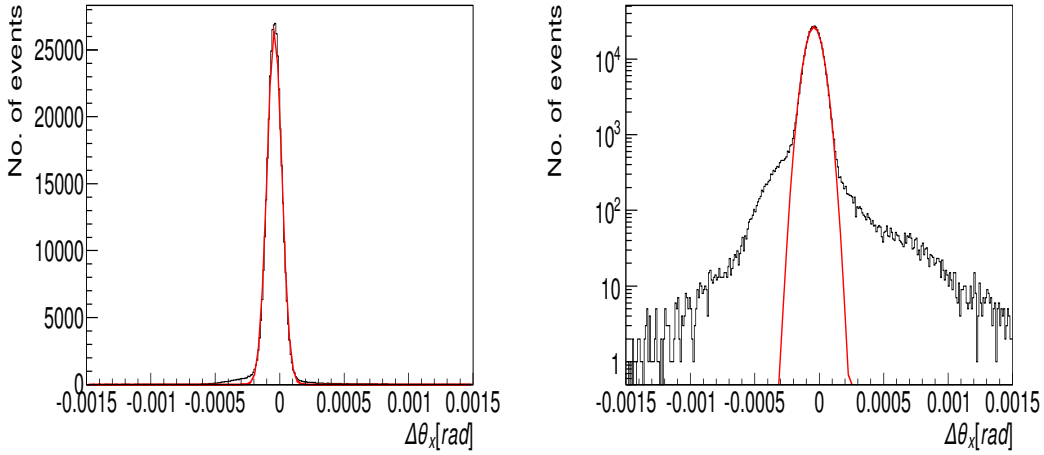

(a) $\Delta\theta_x = \theta_x(EHO) - \theta_x(WHI)$. (b) $\Delta\theta_x = \theta_x(EHO) - \theta_x(WHI)$: log scale.

FIG. 30. Distribution of scattering angle differences of two co-linear detector packages [rad] before co-linearity correction cut.

Besides the 3.5σ co-linearity cut, another quantity, χ^2, was calculated from values of protons' scattering angles as co-linearity analysis cross check with the purpose to further reduce the remaining background. It is estimated that about 1% of background events remained in the data sample after the 3.5σ co-linearity cut was applied. The χ^2 variable is given by:

$$\chi^2 = \left(\frac{\Delta\theta_x}{\sigma_x}\right)^2 + \left(\frac{\Delta\theta_y}{\sigma_y}\right)^2, \tag{92}$$

where $\Delta\theta_x$ and $\Delta\theta_y$ represent the differences in scattering angles between co-linear protons and σ_x and σ_y are one standard deviation from the Gaussian fits to these differences, in x and y-coordinates respectively. A sample χ^2 distribution is shown in Fig. 31.

In order to cross-check the 3.5σ co-linearity cut, a $\chi^2 \leq 22$ cut was applied. Particles that passed the 3.5σ cut have $\chi^2 \leq 22$. Co-linearity plots of $\theta_{x,y}(East)$ vs. $\theta_{x,y}(West)$ and $\Delta(\theta_x)$ vs. $\Delta(\theta_y)$ before and after 3.5σ and $\chi^2 \leq 22$ co-linearity cuts are shown in Fig. 33 and Fig. 32 respectively.

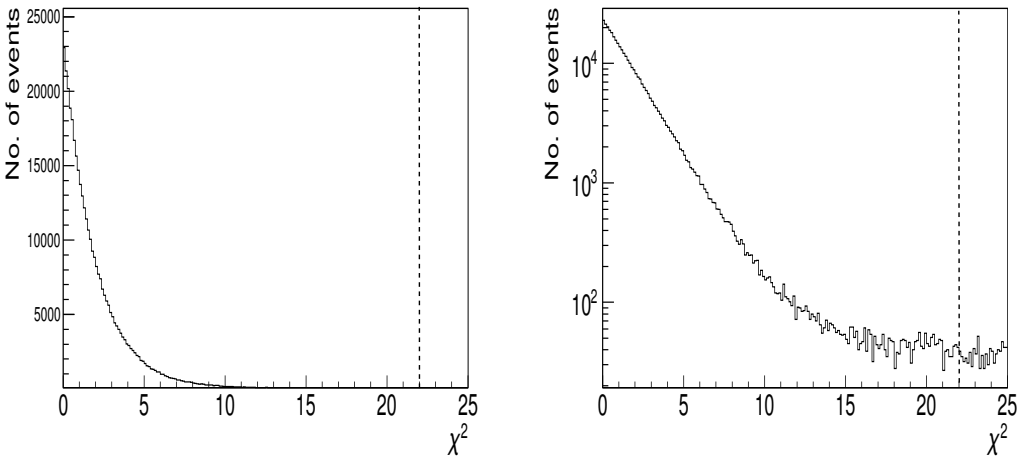

(a) χ^2. (b) χ^2 - log scale.

FIG. 31. χ^2 for EHO-WHI detector arm before the 3.5σ co-linearity condition is applied. Note the logarithmic scale on the right.

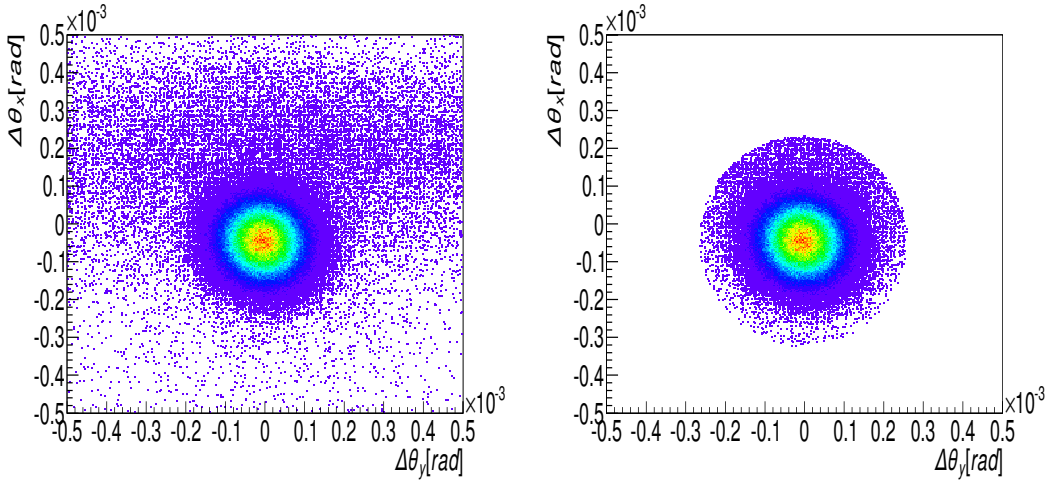

(a) $\Delta(\theta_x)$ vs. $\Delta(\theta_y)$ before cuts. (b) $\Delta(\theta_x)$ vs. $\Delta(\theta_y)$ after cuts.

FIG. 32. $\Delta(\theta_x)$ vs. $\Delta(\theta_y)$ before and after 3.5σ and $\chi^2 \leq 22$ co-linearity cuts for EHI-WHO detecting arm.

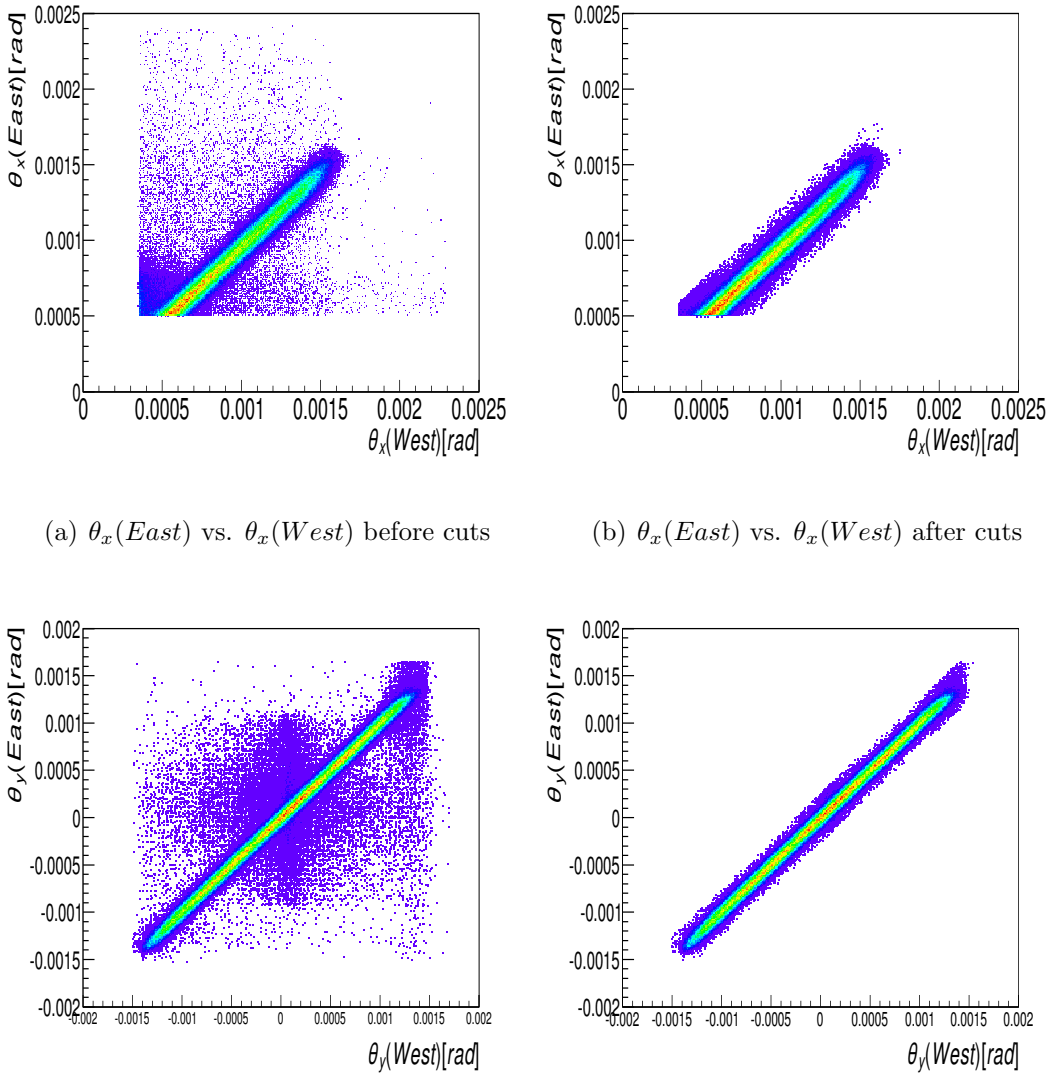

(a) $\theta_x(East)$ vs. $\theta_x(West)$ before cuts

(b) $\theta_x(East)$ vs. $\theta_x(West)$ after cuts

(c) $\theta_y(East)$ vs. $\theta_y(West)$ before cuts

(d) $\theta_y(East)$ vs. $\theta_y(West)$ after cuts

FIG. 33. Co-linearity of particles from opposite sides of IP before and after 3.5σ and $\chi^2 \leq 22$ co-linearity cuts for EHI-WHO detecting arm.

5.1.12 EFFICIENCIES OF SILICON STRIP DETECTORS

The efficiency of all Si strip detecting planes in the experiment was studied. The

efficiency of a detector plane is defined as:

$$\varepsilon_i = \frac{N_{i,detected}}{N_{i,total}} \tag{93}$$

where $N_{i,detected}$ and $N_{i,total}$ represent number of detected and total number of particles, respectively, that passed through i^{th} detector plane. Total number of particles is given with:

$$N_{i,total} = N_{i,detected} + N_{i,not\ detected}. \tag{94}$$

In order to find the number of particles that passed through i^{th} detector but were not detected, one has to check whether those particles were, in fact, detected by other detector planes (planes within the same Roman pot, as well as the ones within opposite, co-linear Roman pot). If all other Si planes detected the particle, and the one that is being checked didn't, then the hit that was not detected can be added to $N_{i,not\ detected}$. From efficiencies of all detector planes represented in Fig. 34(a) only EVU(A) and WHI(A) have values less than 97%. This is mainly due to the existence of bad channels/strips in this detector planes. If a particle hits the bad strip (malfunctioning strip with high or no occupancies) and those strips are excluded from track reconstruction analysis, it is still added to the $N_{i,not\ detected}$ because bad channels add to the inefficiency of the detector.

The efficiency analysis was also performed when clusters from bad channels are not added to $N_{i,not\ detected}$. By comparing Fig. 34(a) and Fig. 34(b) one can conclude that inefficiencies due to the existence of bad channels (see Section 5.1.7 and Table 8) contribute the most.

Efficiencies of the detecting planes range from about 96.5% to over 99%. Therefore, the overall average probability to detect a particle in one detector Si plane pair is about 99.9%. The requirement that a particle is detected on both sides of the IP in both pairs of Si detector planes (A and C or B and D; the same nomenclature as in the Table 11) gives the overall probability to detect elastic event in the detecting system (all Roman pots) of about 99.6%.

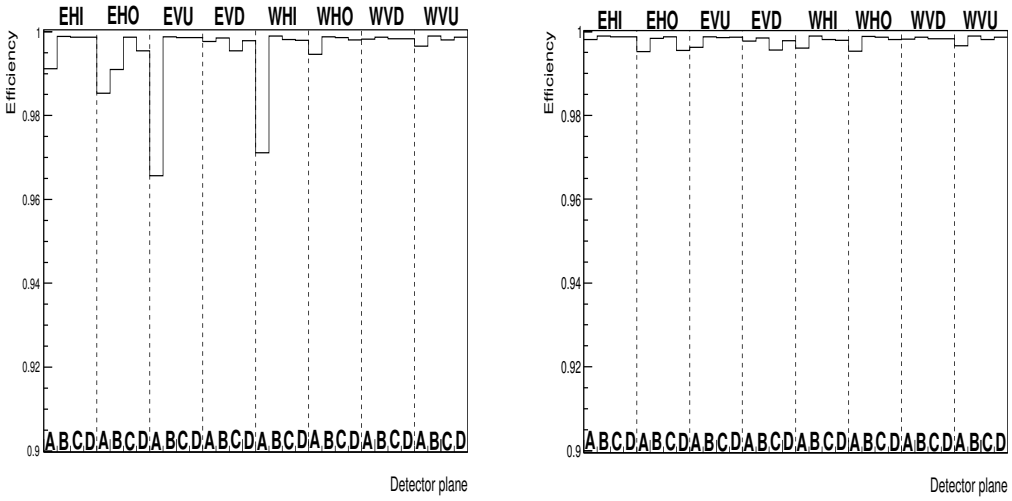

(a) Efficiencies, including "bad" Si micro-strips.

(b) Efficiencies, excluding "bad" Si micro-strips.

FIG. 34. Efficiencies for all detector planes.

5.1.13 FIDUCIAL CUTS

Generally, a fraction of particles acquires enough transverse energy from the repulsive space-charge forces within the beam to form a halo. Characteristics of the beam halo are absence of clearly defined separation between the halo and the main core of the beam and increased population of the outer part of the beam. These properties and proximity of the detectors to the beam during data taking periods lead to the "pollution" of the elastic data sample with particles of the beam halo. Therefore, the elastic event sample is further reduced by applying fiducial cuts. Since there was no possibility to distinguish between particles from the beam halo and elastically scattered protons, highly occupied regions in certain detector stations were entirely removed from further analysis. It is estimated that only about 0.3% of the particles were removed from the elastic data sample with this cut.

An example of proton $|t|$ vs. φ distributions before and after fiducial cuts is represented in Fig. 35.

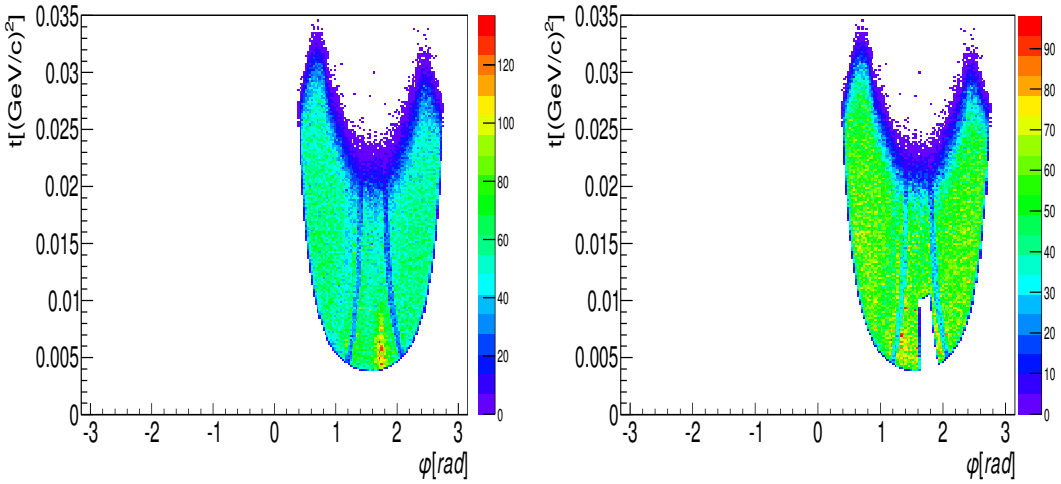

(a) Before fiducial cut.

(b) After fiducial cut.

FIG. 35. $|t|$ vs. φ distributions of elastically scattered protons.

5.1.14 ELASTIC TRACK RECONSTRUCTION SUMMARY

Table 13 gives the total number of events processed in 45 runs and the number of events after each major selection criteria: elastic trigger (scintillators with proper combinations); cluster matching and co-linearity condition.

TABLE 13. Elastic event selection summary.

Tot. No. of events recorded	58,068,295
Tot. No. of elastic triggers	32,729,261 (∼44% less)
Tot. No. of "matching" events	25,195,897 (∼23% less)
Tot. No. of co-linear elastic events	22,130,570 (∼12% less)
Tot. No. of "golden" events	18,452,103 (∼17% less)

5.2 ASSIGNING KINEMATIC PARAMETERS

5.2.1 BEAM TRANSPORT EQUATIONS

Correlated equations for positions and angles of the beam protons describe the beam transport. Elastically scattered protons have small scattering angles and their trajectories are determined by the beam optics. Consequently, elastically scattered protons can be described by the same set of correlated equations [11]:

$$\begin{aligned} x^d &= a_{11}\cdot x_0^{\mathrm{IP}} + L_{effx}\cdot\theta_x^{\mathrm{IP}} + a_{13}\cdot y_0^{\mathrm{IP}} + a_{14}\cdot\theta_y^{\mathrm{IP}} \\ \theta_x^d &= a_{21}\cdot x_0^{\mathrm{IP}} + a_{22}\cdot\theta_x^{\mathrm{IP}} + a_{23}\cdot y_0^{\mathrm{IP}} + a_{24}\cdot\theta_y^{\mathrm{IP}} \\ y^d &= a_{31}\cdot x_0^{\mathrm{IP}} + a_{32}\cdot\theta_x^{\mathrm{IP}} + a_{33}\cdot y_0^{\mathrm{IP}} + L_{effy}\cdot\theta_y^{\mathrm{IP}} \\ \theta_y^d &= a_{41}\cdot x_0^{\mathrm{IP}} + a_{42}\cdot\theta_x^{\mathrm{IP}} + a_{43}\cdot y_0^{\mathrm{IP}} + a_{44}\cdot\theta_y^{\mathrm{IP}}, \end{aligned} \tag{95}$$

where x_0^{IP} and y_0^{IP} are positions at the interaction point, and x^d, y^d, θ_x^d and θ_y^d are positions and angles at the detection point respectively. Coefficients a_{ij}, L_{effx} and L_{effy} depend on the magnetic fields in each of the four detecting sectors and are given with transport matrices (see Section 4.2).

Solving the system of equations, Eq. (95), for the scattering angles at the interaction point results in:

$$\begin{aligned} \theta_x^{\mathrm{IP}} &= \frac{1}{L_{effx}-\frac{a_{14}a_{32}}{L_{effy}}}\left[x^d + \frac{a_{14}}{L_{effy}}y^d + \left(\frac{a_{14}a_{31}}{L_{effy}} - a_{11}\right)x_0^{\mathrm{IP}} + \left(\frac{a_{14}a_{33}}{L_{effy}} - a_{13}\right)y_0^{\mathrm{IP}}\right] \\ \theta_y^{\mathrm{IP}} &= \frac{1}{L_{effy}-\frac{a_{14}a_{32}}{L_{effx}}}\left[y^d + \frac{a_{32}}{L_{effx}}x^d + \left(\frac{a_{32}a_{13}}{L_{effx}} - a_{33}\right)y_0^{\mathrm{IP}} + \left(\frac{a_{32}a_{21}}{L_{effx}} - a_{31}\right)x_0^{\mathrm{IP}}\right]. \end{aligned} \tag{96}$$

Using transport matrices leads to eight equations for proton scattering angles at the IP, two for each detecting sector:

$$\begin{aligned} \theta^{\mathrm{IP}}_{x(B,H)} &= 0.03959\cdot\left[x^d - 0.0001223\cdot y^d + 0.003615\cdot x_0^{\mathrm{IP}} + 0.0001477\cdot y_0^{\mathrm{IP}}\right][1/m] \\ \theta^{\mathrm{IP}}_{y(B,H)} &= 0.04039\cdot\left[y^d + 0.0001601\cdot x^d - 0.004214\cdot y_0^{\mathrm{IP}} + 0.0001477\cdot x_0^{\mathrm{IP}}\right][1/m] \\ \theta^{\mathrm{IP}}_{x(B,V)} &= 0.03953\cdot\left[x^d - 0.0001616\cdot y^d + 0.008311\cdot x_0^{\mathrm{IP}} + 0.0001471\cdot y_0^{\mathrm{IP}}\right][1/m] \\ \theta^{\mathrm{IP}}_{y(B,V)} &= 0.04374\cdot\left[y^d + 0.0001301\cdot x^d + 0.001086\cdot y_0^{\mathrm{IP}} + 0.0001471\cdot x_0^{\mathrm{IP}}\right][1/m] \\ \theta^{\mathrm{IP}}_{x(Y,H)} &= -0.03952\cdot\left[x^d - 0.0001732\cdot y^d - 0.003572\cdot x_0^{\mathrm{IP}} + 0.0001477\cdot y_0^{\mathrm{IP}}\right][1/m] \\ \theta^{\mathrm{IP}}_{y(Y,H)} &= -0.04032\cdot\left[y^d - 0.0000824\cdot x^d + 0.004281\cdot y_0^{\mathrm{IP}} - 0.0000144\cdot x_0^{\mathrm{IP}}\right][1/m] \\ \theta^{\mathrm{IP}}_{x(Y,V)} &= -0.03945\cdot\left[x^d + 0.0001983\cdot y^d - 0.008249\cdot x_0^{\mathrm{IP}} - 0.0000002\cdot y_0^{\mathrm{IP}}\right][1/m] \\ \theta^{\mathrm{IP}}_{y(Y,V)} &= -0.04366\cdot\left[y^d - 0.0000712\cdot x^d - 0.000999\cdot y_0^{\mathrm{IP}} - 0.0000002\cdot x_0^{\mathrm{IP}}\right][1/m] \end{aligned} \tag{97}$$

Positions x_0^{IP} and y_0^{IP} were set to zero (which greatly simplifies Eq. (97)) and were

chosen as reference points for various corrections (i.e. alignment, etc.). Sample plots of proton scattering angles are shown in Fig. 36.

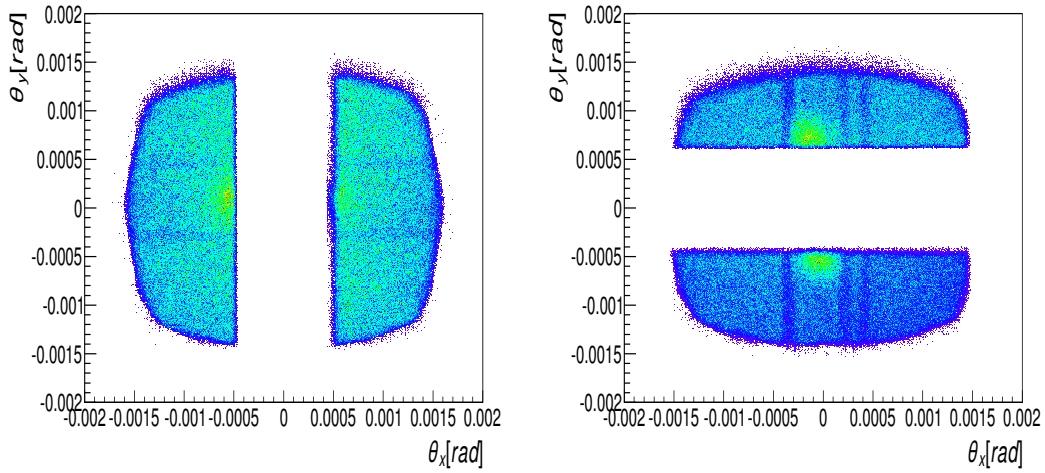

(a) Horizontal Detector Arms. (b) Vertical Detector Arms.

FIG. 36. θ_y^{IP} vs. θ_x^{IP} sample plot for one RP insertion position. Less populated regions on the plots do not come from bad/noisy strips (see Section 6).

Scattering angle values obtained by using Eq. (97) were used to calculate the value of the four momentum transfer squared (see Section 3.7):

$$|-t| = -p^2 \sin^2\left(\frac{\Theta_{\mathrm{IP}}}{2}\right) \simeq -p^2\Theta_{\mathrm{IP}}^2, \tag{98}$$

where Θ_{IP} is given by:

$$\Theta_{\mathrm{IP}} = \sqrt{(\theta_x^{\mathrm{IP}})^2 + (\theta_y^{\mathrm{IP}})^2}. \tag{99}$$

The azimuthal angle φ was calculated by using the scattering angles values obtained from the same set of equations, Eq. (97):

$$\varphi = \arctan\left(\frac{\theta_y^{\mathrm{IP}}}{\theta_x^{\mathrm{IP}}}\right). \tag{100}$$

Since both co-linear protons come from the same, single event, the values of $|t|$ and φ were averaged between the values obtained from both sides of IP. The sample

distribution of kinematic parameters assigned to each proton in the sample is shown in Fig. 37.

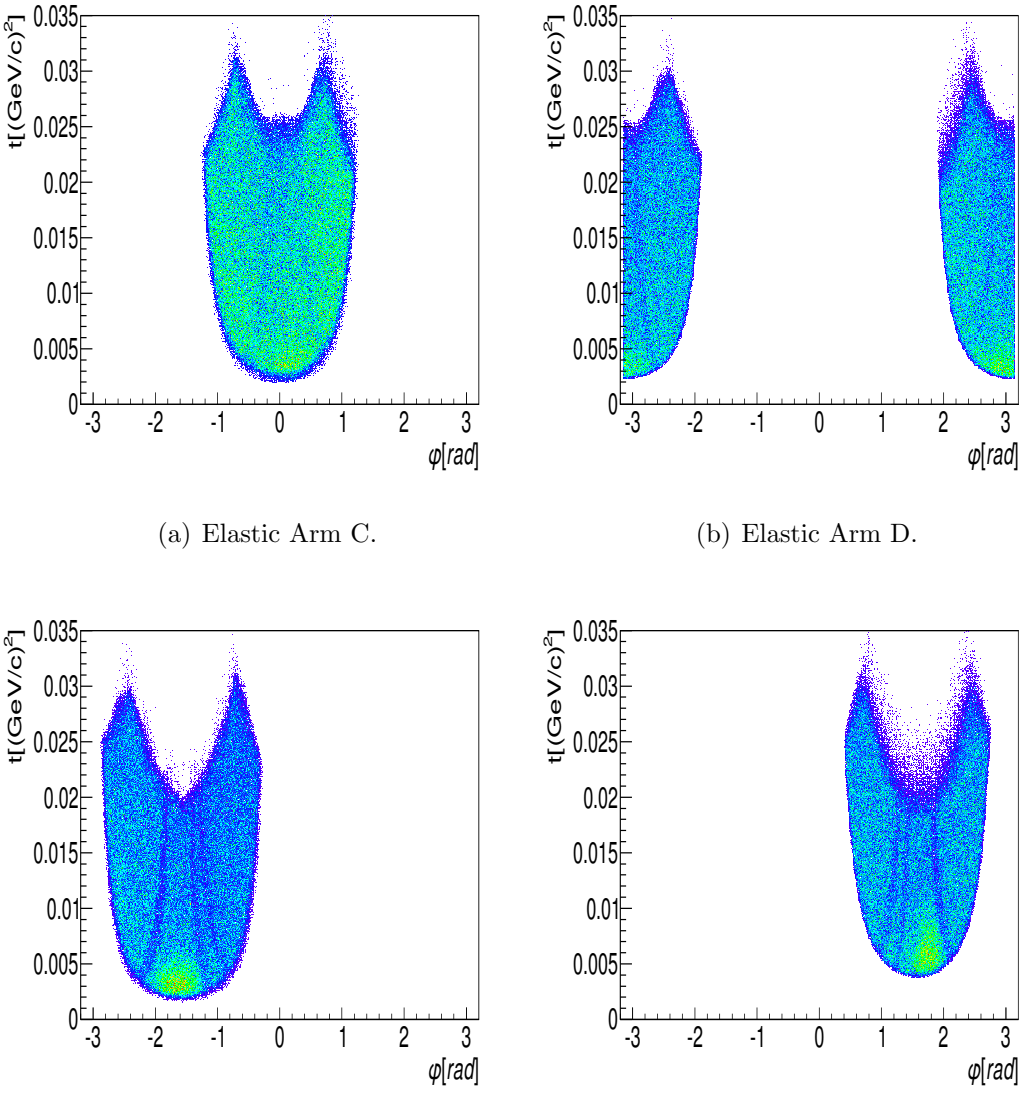

(a) Elastic Arm C.

(b) Elastic Arm D.

(c) Elastic Arm B.

(d) Elastic Arm A.

FIG. 37. $|t|$ vs. φ sample plot for one RP insertion positions.

CHAPTER 6

SIMULATIONS AND DATA CORRECTIONS

After reconstruction of elastic events from the raw data, it was noticed that some detecting regions had significantly less efficiency for particle detection. Bearing in mind that the efficiencies of the silicon strip detectors were thoroughly checked, (see Section 5.1.12) and were found to be very satisfactory (more than 99%), the existence of less efficient regions of the detectors' planes was somewhat puzzling.

Less efficient regions of the detectors' silicon micro-strip planes manifest themselves as "shadows" on spatial, angular particle distributions or on the $|t|$ vs. φ plots (see Fig. 36 and Fig. 37). A careful study of these so called "shadows" was necessary because they are located across 100% acceptance detectors' regions and protons that this analysis is based upon come from these regions. Consequently, not studying and/or correcting this effect can possibly lead to incorrect differential cross-section values and hence, nuclear slope parameter B and σ_{tot}.

There are two causes for the existence of this systematic effect. The first one is the interaction of scattered protons with materials from which Roman pots and detector packages were manufactured. Steel edges at the bottom of the RP cylindrical vessels and their thin front and back steel windows play a major role in the "shadow" appearance. When scattered $\sim$100 GeV/c protons reach the Roman pot detectors, they interact with their materials and loose some energy (about 130 keV in 5 cm of steel, [74]), which is a rather small loss when compared to their energy before this interaction. However, there is a good probability that these protons will scatter or even disintegrate, deviating from their original trajectories. This can lead to incorrect detection of proton positions and angles. These offsets from original trajectories were carefully studied because they can cause rejection of events for not satisfying co-linearity selection criteria (see Section 5.1.11).

The second effect that can cause "shadows" to occur are elastic trigger conditions that were set in this experiment (see Section 5.1.9). When protons break apart after interaction with materials of the Roman pots, the products of this interaction can end up triggering scintillators of the Roman pot in the same detector station, causing "forbidden" elastic trigger combination (see Table 10) and hence rejection ("vetoing")

of perfectly good elastic events.

The experimental layout of this experiment (see Fig. 14) is such that horizontal RP stations are placed closer to the IP then vertical RP stations and hence, are "front" RP stations. Therefore it is expected that vertical RPs ("back" RPs) have both of the effects listed above and that horizontal RPs ("front" RPs) only have trigger "vetoing" effects. However, the trigger effects are more complex in the sense that there is significant probability that RPs from opposite sides of the IP can "shadow" each other, especially if they are inserted to different distances from the beam. This will be explained in one of the following sections.

In attempt to understand, estimate and correct these systematic issues that occurred in the experiment and possibly improve and optimize future runs, Monte Carlo simulations, using GEANT4 simulation software, were performed [85].

6.1 GEANT4 SIMULATION OF INTERACTIONS OF PROTONS WITH THE MATERIALS OF ROMAN POTS

GEANT4 is a toolkit for the accurate simulation and passage of particles through matter. Its areas of application include high energy, nuclear and accelerator physics, as well as studies in medical and space science [85]. A simulation using GEANT4 includes all aspects of simulation processing starting with the geometry of the system and materials involved, through introduction of particles of interest, generation of primary events and their tracking, up to introducing physics processes that govern particle interactions etc.

The simulation in this analysis follows these steps:

1. Generating a system of eight Roman pot detector packages using proper geometry, dimensions and materials, positioned to resemble the entire detecting system used in the experiment and inserted to the same 11 insertion positions as in Run 2009.

2. Random generation of N protons with properties of real beam protons (momentum, etc.) and their tracking throughout detecting system (including appropriate High Energy Physics simulation models, e.g. FTFP-BERT, [85]) with emphasis on their interactions with virtual Roman pots.

3. Recreating trigger vetoing conditions, analyzing systematics and obtaining correction functions.

6.1.1 GEOMETRY OF THE SYSTEM AND MATERIALS INVOLVED

Since the goal of this simulation was to study particle interactions with materials of Roman pots as well as the systematic effects caused by these interactions, it was sufficient to simulate only Roman pot detecting system and not to include any of the beam optics elements before or after it. In order to achieve this, particles were randomly generated at the interaction point (IP) and then "propagated" to their detecting positions by using the transport equations from experimental Run9 (see Section 5.2.1).

Each Roman pot detector is simulated in that way that it resembles the real detector used in the experiment. It consisted of detector housing and detecting package. Each detector package is assembled out of four silicon detecting planes with their power circuit boards and aluminum rails and one scintillator (see Section 3.4).

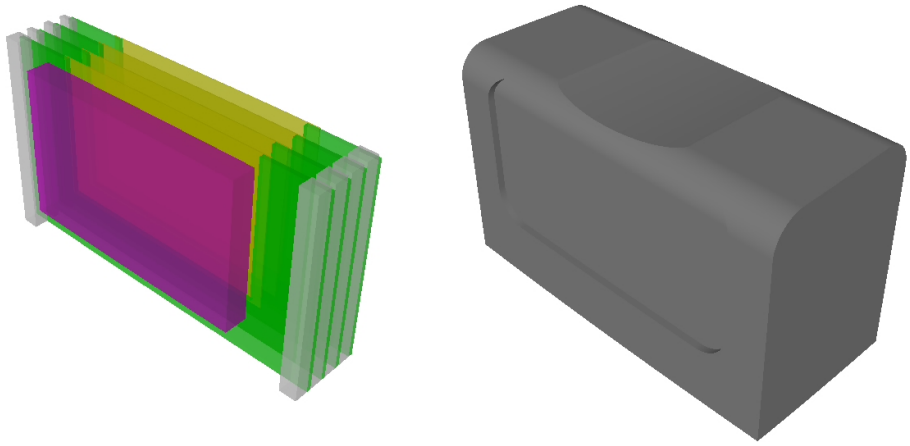

(a) Simulated RP detector package. (b) Simulated RP detector housing.

FIG. 38. GEANT4 simulation of RP detector package and housing. Detector package is an assembly of Si micro-strip detectors (yellow), PCBs (green), Al rails (grey) and vinyltoulene scintillator (magenta). Roman pot housing consists of stainless-steel housing frame and thin stainless-steel window.

In this simulation it was sufficient to approximate silicon strip detecting planes

as blocks of silicon material of proper thickness and not as an assembly of given number of p-n junctions (micro-strips) used in the experiment. The detector housing is simulated to be made of stainless steel with its interior filled with air at pressure of one atmosphere. PCBs are made of G10FR4 material which is a mixture of 60% SiO_2 and 40% Epoxy-Resin ($C_{11}H_{12}O_3$). Material for scintillators is vinyltoulene used by many scintillator manufacturers. The full list of used materials in this GEANT4 simulation is given in Table 14.

TABLE 14. The list of materials used in GEANT4 simulation for detector construction.

RP Component	Material
Si micro-strip	Si
Scintillator	G4_PLASTIC_SC_VINYLTOLUENE
Al rails	Al
PCBs	G10FR4
RP housing	Stainless-steel
G10FR4	60% SiO_2 and 40% Epoxy-Resin
Epoxy-Resin	$C_{11}H_{12}O_3$, density = 1.268 g/cm^3

Sensitive parts of simulated Roman pots were logical volumes of four silicon planes and a scintillator logical volume [85]. These sensitive volumes were designed to detect hits and record positions and deposited energies (in the volume material) of all particles that interacted with them. Examples of deposited energies, by both primary protons and all other secondarily produced particles in the Si micro-strip planes and scintillators, are presented in Fig. 39.

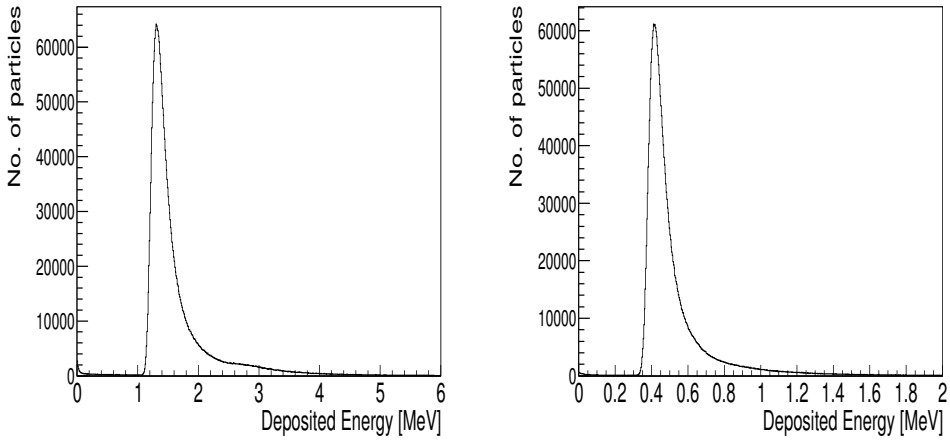

(a) Deposited energy in 8 mm thick scintillator.

(b) Deposited energy in 400 μm thick Si.

FIG. 39. Deposited energies (in MeV) by primary protons and secondarily produced particles in the sensitive logical volumes of simulated Si micro-strip planes and scintillators.

Deposited energies depend on the type and energy of the particle and on the properties of the material it passes. In the case of plastic scintillators, deposited energy (due to the ionization by all particles) is proportional to the number of "optical" photons produced in the scintillator. This number is proportional to the number of "optical" photons that fell on the photo-cathode of the PMTs which is further proportional to the number of photo-electrons emitted from this photo-cathode. The ADC count variable (digitized integrated PMT current) that is assigned to this number is what we measure in reality. In this GEANT4 simulation, the full chain of ADC count on energy deposit dependence was not simulated. Instead, for the purpose of triggering, the energy deposit was tuned in the scintillator by smearing and linear conversion to the measured ADC spectra.

Positions of primary particles, for the cases when energy was deposited in simulated scintillators, were recorded by four simulated silicon micro-strip planes. Single hit positions were obtained by calculating an average value from the positions recorded in silicone planes. It is important to note that deposited energies were recorded for any particle that interacted with sensitive logical volumes and positions only for primary generated protons. By having this, "pollution" in recorded data

samples by secondarily produced particles was avoided. On the other hand, it was absolutely necessary to record energies deposited by all particles produced in the simulation for the recreation of proper trigger conditions from 2009.

6.1.2 GENERATION OF PRIMARY EVENTS, PARTICLES OF INTEREST AND THEIR TRACKING

Each of the simulated events started with random generation of two numbers, four momentum transfer squared $|t|$, and azimuthal angle φ at the interaction point (IP). Azimuthal φ angle was generated as a uniform random distribution of numbers between 0 and 2π and four momentum transfer squared $|t|$ from both uniform and the distributions determined by the equation for theoretical differential elastic cross-section (see Eq. (34)) with $\rho = 0.13$, $\sigma_{tot} = 51.6$ mb and $B = 16.3$ c^2/GeV^2, parameters fixed to the expected values obtained from the extrapolation of the World available experimental data [10], [9], [13]. Simulated $|t|$ range covered the experimental *pp*2*pp* Run9 range which was between 0.001 (GeV/c)^2 and 0.035 (GeV/c)^2.

The two generated numbers were then used to calculate scattering angles θ_x^{IP} and θ_y^{IP} at the IP by using Eq. (101)

$$\begin{aligned} \theta_{0\ x}^{W,E} &= \arctan\left(\tan\theta\ \cos\varphi\right) \\ \theta_{0\ y}^{W,E} &= \arctan\left(\tan\theta\ \sin\varphi\right), \end{aligned} \tag{101}$$

where $\theta = \sqrt{t}/p$ and $p = 100$ GeV/c.

Smearing of scattering angles was done by adding a non-zero crossing angle and beam angular divergence. The beam angular divergence was simulated as a Gaussian correction with standard deviation of about 40 μrad, obtained from the experimental angular beam divergence of Run9 data, Eq.(102),

$$\theta_{x,y}^{W,E} = \theta_{0\ x,y}^{W,E} + \delta\theta_{x,y}^{W,E}, \tag{102}$$

where $\delta\theta_{x,y}^{W,E}$ represents smearing of the scattering angles and is equal the sum of the beam crossing angle and angular beam divergence.

Furthermore, another smearing was introduced, this time to the z positions of the interaction point, also in the form of a Gaussian distribution around $z = 0$. Standard deviation for the Gaussian of the z vertex position was also obtained from the data.

After the smearing process, calculated scattering angle values were used in

transport equations (Eq. (95)) in order to obtain θ_x^d, θ_y^d, x^d and y^d values in front of both, blue and yellow, horizontal Roman pot stations (Eq. (103)). The beam positions x_0^{IP} and y_0^{IP} were assumed to be equal to zero.

$$\begin{bmatrix} x \\ \theta_x \\ y \\ \theta_y \end{bmatrix}_{RP}^{W,E} = T_H^{W,E} \begin{bmatrix} 0 \\ \theta_x \\ 0 \\ \theta_y \end{bmatrix}_{IP}^{W,E} . \tag{103}$$

Momentum directions of primarily generated protons were set by the use of calculated scattering angles at the detection point $\theta_{RP}^{W,E}$ as:

$$\begin{aligned} p_x &= 0 \\ p_y &= \sin\, \theta_{RP}^{W,E} \\ p_z &= \pm\cos\, \theta_{RP}^{W,E}. \end{aligned} \tag{104}$$

Tracking of primarily generated 100 GeV/c protons started in front of the blue and yellow horizontal RP stations and ended after both blue and yellow vertical RP stations. Propagation of "primaries", their interaction with materials and creation and propagation of secondary generated particles is controlled by the predefined GEANT4 high energy physics model FTFP_BERT.

Generated particles were accepted only if both particles on either side of the IP did not hit the apertures of Q_2 and Q_3 quadruple magnets. This was done by calculation of $x_{Q2,Q3}^{W,E}$ and $y_{Q2,Q3}^{W,E}$ coordinates at Q_2 and Q_3 and their comparison with the size of the apertures of corresponding magnets (see Section 6.4).

6.2 CALCULATION OF KINEMATIC VARIABLES AT IP FROM DETECTED SIMULATED EVENTS

After detection of positions and deposited energies of simulated particles at the Roman pots, kinematic variables $|t|$ and φ at the interaction point were calculated. The methodology and reconstruction procedure was essentially the same as the procedure and methodology applied during reconstruction of the same variables from the IP in experimental data samples (see Chapter 5.2). Plots with calculated kinematic variables together with positions of detected simulated particles are represented in Fig. 40.

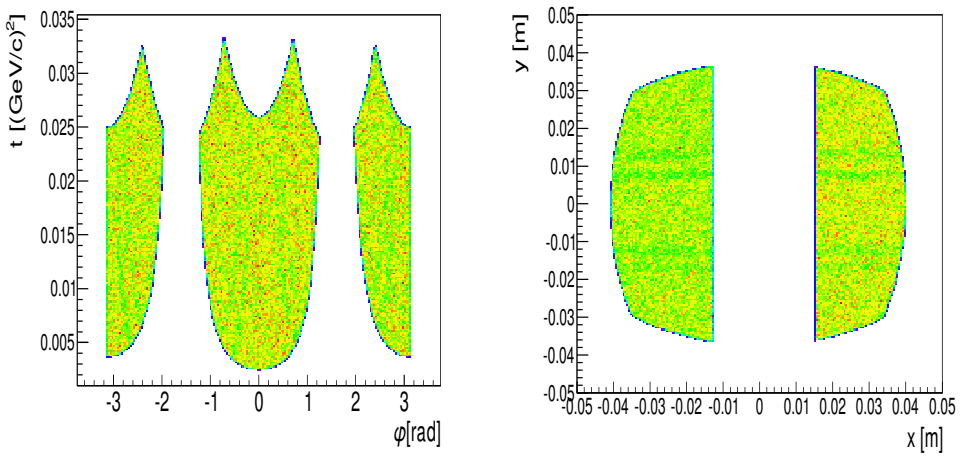

(a) $|t|$ vs. φ particle distribution. (b) Spatial particle distribution.

FIG. 40. $|t|$ vs. φ and spatial distributions of simulated particles.

6.3 TRIGGER BIAS

One of the purposes of this simulation was the study and correction of trigger bias systematic effects observed in selected experimental data samples.

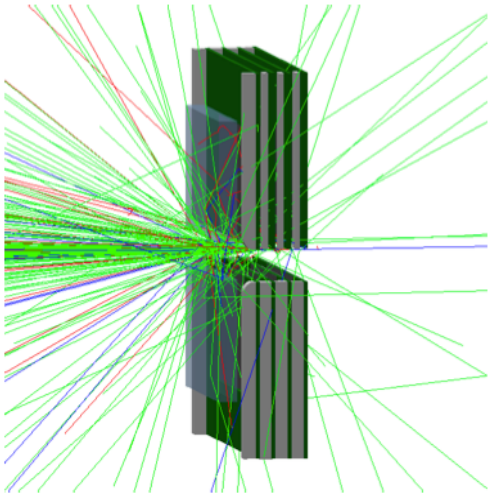

FIG. 41. Simulation of secondary particles production in the primary proton - RP detector material interactions. Image curtesy of R. Sikora [8].

The primary particle loss is more conspicuous in vertical Roman pot stations. As previously noted in Chapter 3, vertical Roman pot stations are positioned farther away from the interaction region and horizontal closer to it. Horizontal and vertical Roman pot stations have overlap regions in the $x - y$-coordinate plane. When outgoing scattered protons hit horizontal Roman pots, especially in the case when they hit Roman pot steel edges, they can disintegrate or deviate from their original trajectories. If this occurs, those protons become lost for corresponding vertical Roman pot detectors and this loss is observed in the data samples of vertical Roman pots. Furthermore, this process works reversibly, when hitting the edges of vertical Roman pot stations vetoes corresponding events in horizontal Roman pots. This process is less intuitive. As explained above, if the scattered outgoing proton disintegrates while hitting the steel edge of one of the vertical Roman pots, the showers of particles that are produced in the process can cause a "forbidden" trigger combination (Table 9) that vetoes events in the corresponding horizontal Roman pot stations. Both of these effects can be observed in Fig.37.

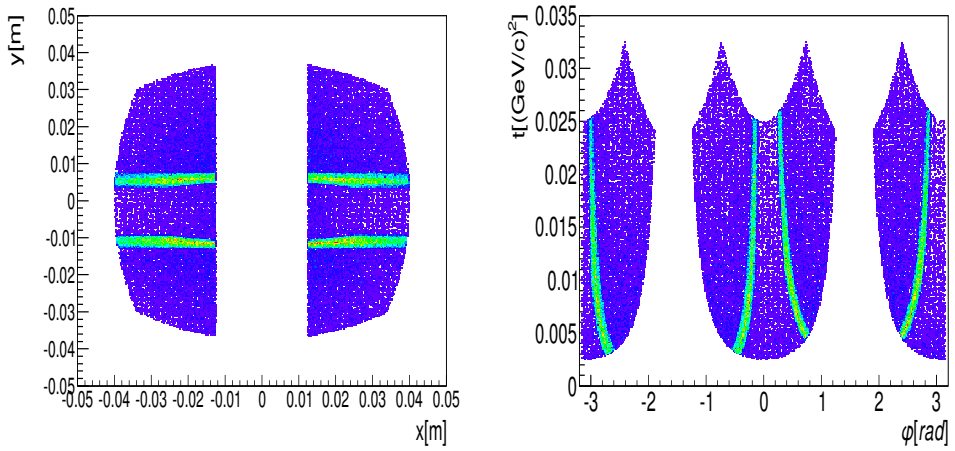

(a) Coordinate space. (b) $|t|$ - φ space.

FIG. 42. Horizontal Roman pot detectors: Distributions of particles lost due to trigger bias systematic effect.

It is estimated from the experimental data, that the loss of events due to trigger inefficiencies in certain spatial regions of the detector are of the order of about 25%

of the entire event sample collected in those regions. This is mainly in the regions of the horizontal RPs that line up with steel edges of vertical RPs. This effect is also present in the remaining regions of the detector due to uniformly distributed material. However, from the simulation it was found that vetoing in those regions was of the order of several percent.

The particles lost from experimental data can not be retrieved. However, their number and spacial distribution is estimated in this GEANT4 simulation. The distributions of particles in coordinate and $t - \varphi$ space are represented in Fig.42.

6.3.1 CORRECTION FUNCTIONS

A study of inefficiencies due to the trigger bias effect by use of simulated events made the correction of this systematic effect possible. In order to successfully correct selected experimental data, correction functions for $|t|$ distributions were calculated. For this purpose, simulated $|t|$ distributions with and without trigger bias conditions were used. Correction functions are obtained by:

$$C\left(-t\right) = \frac{\frac{dN}{dt}\Big|_{\text{w. veto}}}{\frac{dN}{dt}\Big|_{\text{w/o. veto}}} \tag{105}$$

An example of a trigger bias efficiency (correction) function for a one of the horizontal detector pairs is shown on Fig.43.

Correction functions depend on several factors, mainly the precision of the simulation. The errors of the correction functions, or in another words, the errors they introduce to the results that are being corrected, are mainly related to the statistics in the simulation. Therefore, the number of events in this simulation was optimized in order to introduce negligible statistical errors to the experimental data samples that are being corrected. However, even though obtained correction functions had negligible statistical errors, the systematic error of this method still contributes to the error of the final B result.

Each simulation had 10 million randomly generated events that were used to calculate correction functions. Each of the analyzed data sets (with different Roman pot insertion positions) had its unique correction function.

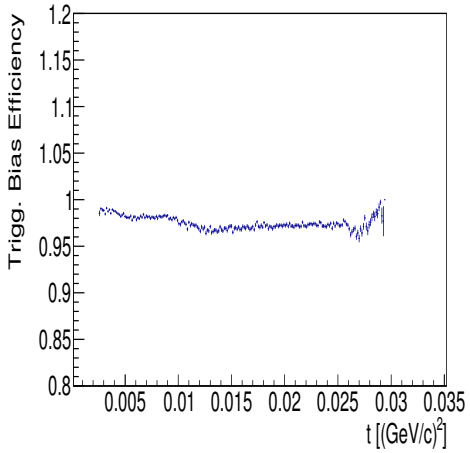

FIG. 43. Trigger Bias efficiency as a function of $|t|$ for EHI-WHO horizontal RP arm, data set 0, obtained from the GEANT4 Monte Carlo simulation.

6.4 DETECTOR ACCEPTANCE STUDY

One important result is obtained by simulating the acceptances and kinematic ranges of the Roman pot detector system used in this experiment. As previously explained (see Section 6.1.2), the trajectories of particles are limited by magnets' apertures and detector acceptances. Acceptances for all RP positions in Run9 were calculated and $|t|$-values of the first strip of each RP was determined. This study shows, given the size of the apertures of accelerator magnets and RP insertion position, what range of $|t|$ was achieved in Run9 and more importantly, what was the $|t|$-region of 100% acceptance that should be used for extracting of the nuclear slope parameter B in a combined fit to the differential cross section. Example of acceptance plot is presented on Fig.44.

The simulation process in the analysis of the Roman pot acceptances in the Run 2009 follows the same procedure given in Section (6.1.2).

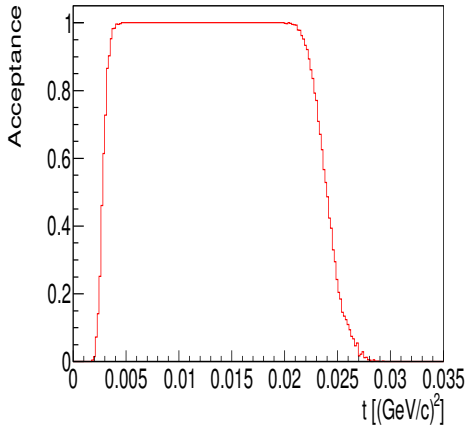

FIG. 44. Acceptance as a function of $|t|$. A region in $|t|$, where the acceptance is independent of $|t|$, is the region of 100 % and flat/constant acceptance: $0.006 \leq |t| \leq 0.02$ (GeV/c)^2. Low-$|t|$ edge is determined by RP insertion depth and high-$|t|$ edge by apertures of accelerator magnets.

Acceptance plots were obtained by dividing the number of simulated protons for a given $|t|$ value, that successfully reached the RP, passing through all the limiting apertures of the magnets between RPs and IP, with the numbers of protons simulated at the IP for exactly the same $|t|$ value. The fall-offs in acceptance plots on the left and right are determined by insertion length of each RP and the size of the magnets' apertures respectfully. In addition, these fall-offs depend of the crossing angles (in this simulation called the smearing of the scattering angles at the IP), beam and vertex positions etc.

A comparison of the $|t|$-distributions of the experimental data sets from Run 2009 together with the acceptance functions for the cases of both detecting arms of horizontal Roman pot detectors is given in Figs. 45 to 49. From these acceptance plots, a Table 15 of $|t|$-ranges used in fitting of experimental $|t|$-distributions (see Chapter 7) is extracted.

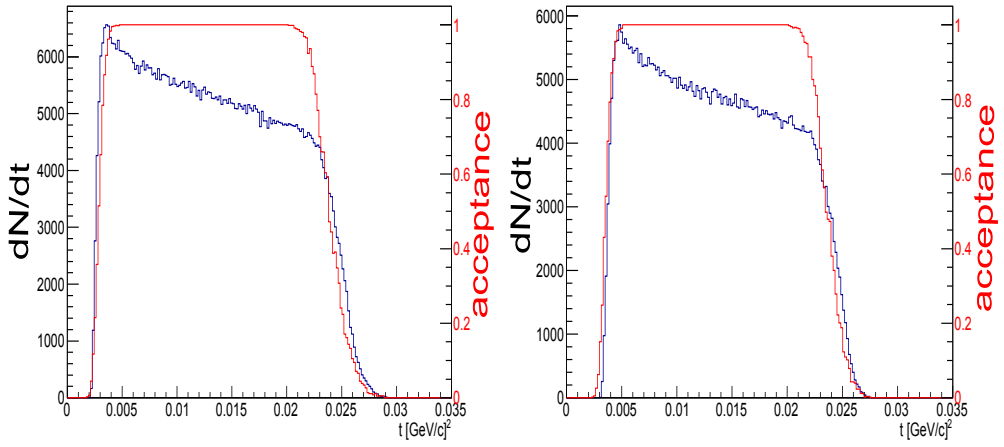

(a) EHI-WHO detector arm. (b) EHO-WHI detector arm.

FIG. 45. RP acceptance functions (red) and experimental $|t|$-distributions (blue) in the case of RP insertion position set 0 for azimuthal $-0.5 \leq \varphi \leq 0.5$ rad (EHI-WHO) and $-2.7 \geq \varphi \geq 2.7$ rad (EHO-WHI) ranges respectively (see Fig. 40 and Sect. 7.1.1).

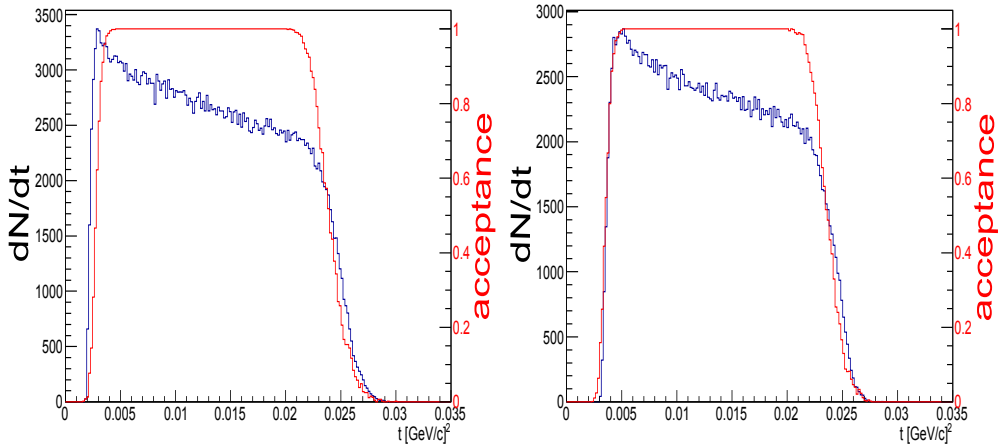

(a) EHI-WHO detector arm. (b) EHO-WHI detector arm.

FIG. 46. RP acceptance functions (red) and experimental $|t|$-distributions (blue) in the case of RP insertion position set 1 for azimuthal $-0.5 \leq \varphi \leq 0.5$ rad (EHI-WHO) and $-2.7 \geq \varphi \geq 2.7$ rad (EHO-WHI) ranges respectively (see Fig. 40 and Sect. 7.1.1).

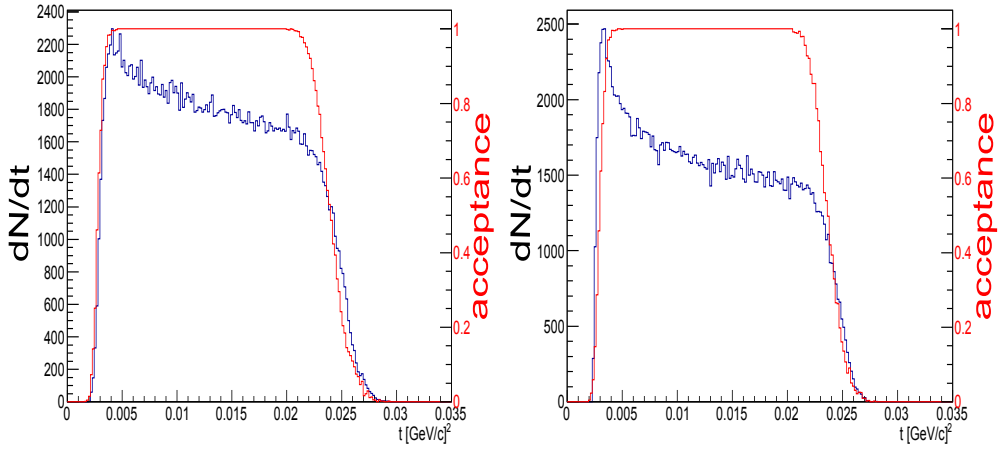

(a) EHI-WHO detector arm. (b) EHO-WHI detector arm.

FIG. 47. RP acceptance functions (red) and experimental $|t|$-distributions (blue) in the case of RP insertion position set 4 for azimuthal $-0.5 \leq \varphi \leq 0.5$ rad (EHI-WHO) and $-2.7 \geq \varphi \geq 2.7$ rad (EHO-WHI) ranges respectively (see Fig. 40 and Sect. 7.1.1).

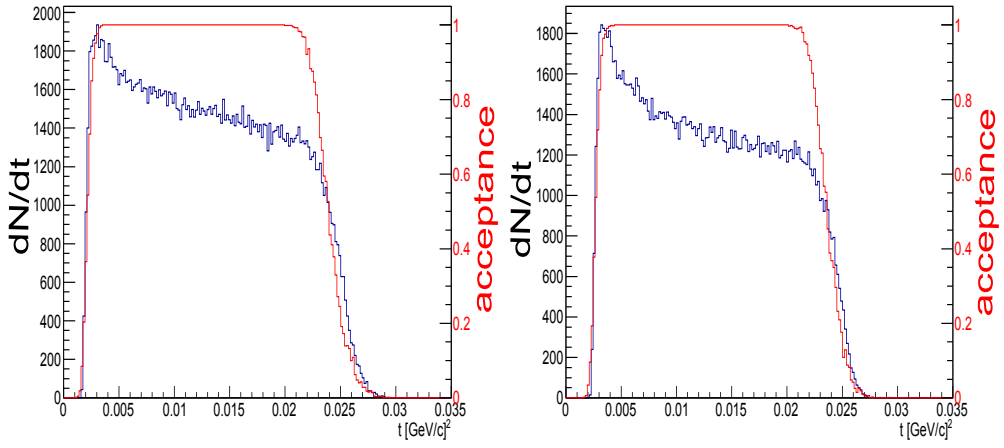

(a) EHI-WHO detector arm. (b) EHO-WHI detector arm.

FIG. 48. RP acceptance functions (red) and experimental $|t|$-distributions (blue) in the case of RP insertion position set 6 for azimuthal $-0.5 \leq \varphi \leq 0.5$ rad (EHI-WHO) and $-2.7 \geq \varphi \geq 2.7$ rad (EHO-WHI) ranges respectively (see Fig. 40 and Sect. 7.1.1).

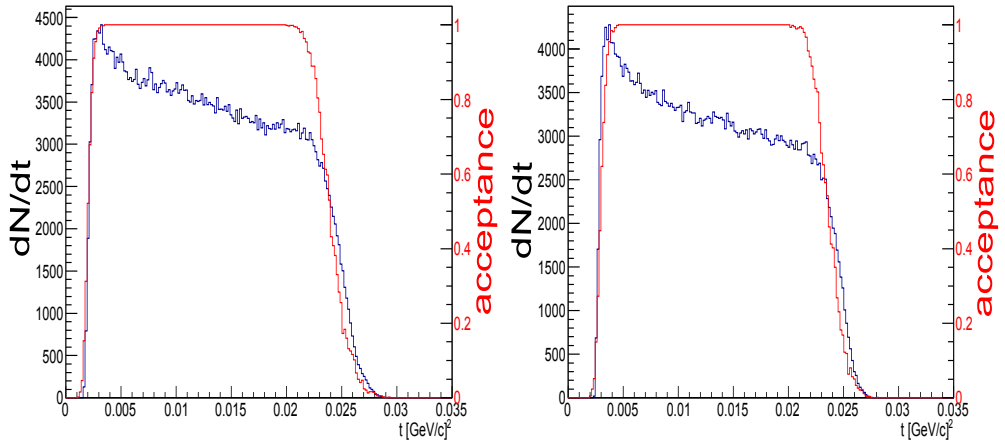

(a) EHI-WHO detector arm. (b) EHO-WHI detector arm.

FIG. 49. RP acceptance functions (red) and experimental $|t|$-distributions (blue) in the case of RPinsertion position set 9 for azimuthal $-0.5 \leq \varphi \leq 0.5$ rad (EHI-WHO) and $-2.7 \geq \varphi \geq 2.7$ rad (EHO-WHI) ranges respectively (see Fig. 40 and Sect. 7.1.1).

Five out of the total of eleven data sets were analyzed for extraction of the nuclear slope parameter B. A discussion about reasons behind rejection of certain data sets will be presented in Chapters 7 and 8.

TABLE 15. Ranges of $|t|$ used in the least square fits to the data for the extraction of nuclear parameter slope B in GeV$^2/c^2$.

Set No.	EHI-WHO	EHO-WHI
0	0.006-0.02	0.007-0.02
1	0.006-0.02	0.007-0.02
4	0.006-0.02	0.008-0.02
6	0.006-0.02	0.008-0.02
9	0.006-0.02	0.008-0.02

CHAPTER 7

PHYSICS RESULTS

In this chapter we present our result for the nuclear slope parameter B from RHIC Run9. The result presented here was obtained from five experimental data sets, each representing one combination of the measurement positions of the Roman pot detector packages. There were total of thirteen experimental data sets with approximately 22 million elastic events selected from the sample of about 33 million elastic triggers recorded in Run9. Elastic events extraction procedure for selection of proton-proton elastic events is shown in Chapter 5.

7.1 ANALYSIS OF EXPERIMENTAL DATA SETS

As previously stated there were a total of thirteen experimental data sets analyzed in this study. Those sets consist of 45 experimental data taking runs and belong to four RHIC beam fills/stores of the Run9 (see Table 4) [77]. After careful analysis of the goodness of all the sets, eight were rejected due to small number of elastic events or problems with the beam fills/stores and/or malfunctioning Roman pot detectors and five were used for extractions of nuclear slopes of the forward peak B.

After initial selection of good data sets (measurement positions of the detector packages), elastic events were plotted in a $|t|$ vs. φ space for the two horizontal arms independently. Vertical detector arms were not used for this analysis (see Chapter 6).

In order to extract the result for nuclear slope parameter B, detector regions with 100% acceptance are used. In order to select events from full acceptance regions, restrictions in φ ranges are introduced. Furthermore, the same φ ranges were used in calculations of the simulated correction functions for compatibility, also shown in Chapter 6.

7.1.1 $|t|$ AND φ RANGES RESTRICTIONS

A restriction of the φ range to $-0.5 \leq \varphi \leq 0.5$ or $-2.7 \geq \varphi \geq 2.7$ leads to a full geometric acceptance in $|t|$. Applying this restriction leads to the $|t|$-distributions

shown in Figs. 45 to 49 and Figs. 51 to 55. According to [12] this φ region needs further investigation and correction of systematic effects which are described in Chapter 8.

7.1.2 FITTING FUNCTION

The differential elastic cross section fitted to the data is given by [11]:

$$\frac{d\sigma}{dt} = C\cdot\left[4\pi(\hbar c)^2\left(\frac{\alpha G_E^2}{t}\right)^2 + \frac{1+\rho^2}{16\pi(\hbar c)^2}\cdot\sigma_{tot}^2\cdot e^{B|t|} - (\rho+\Delta\Phi)\cdot\frac{\alpha G_E^2}{|t|}\cdot\sigma_{tot}\cdot e^{-\frac{1}{2}B|t|}\right], \quad (106)$$

where

$$\frac{\Delta\Phi}{\alpha} = \ln\left(\frac{4a}{B^2}\right) + \ln\left(\frac{B^2|t|}{4(a+\frac{1}{2}B)}\right) - \ln\left(\frac{1}{2}a|t|\right) + e^{a|t|}\cdot\left(-\gamma - 2\ln(a|t|) + \ln\left(\frac{1}{2}a|t|\right)\right). \quad (107)$$

The treatment of the Coulomb phase, $\Delta\Phi$, is based on [86]. The total cross section $\sigma_{tot} = 51.6$ mb [9] and $\rho = 0.13$ [10] were kept fixed to the values taken from the World data, while the normalization constant, C, and the diffraction cone slope, B, were fitted as a function of $|t|$. Other parameters were:

$$\alpha = 137.036^{-1}$$
$$G_E^2 = \left(\frac{\lambda}{\lambda+|t|}\right)^4$$
$$\lambda = 0.71 \text{ GeV}^2/\text{c}^2$$
$$a = 5.6 \ c^2/\text{GeV}^2$$
$$(\hbar c)^2 = 0.389379 \text{ GeV}^2\text{mb}$$
$$\gamma = 0.5772157.$$

The differential cross section (see Eq. (106)) and its individual contributions are shown as a function of $|t|$ in Fig. 50.

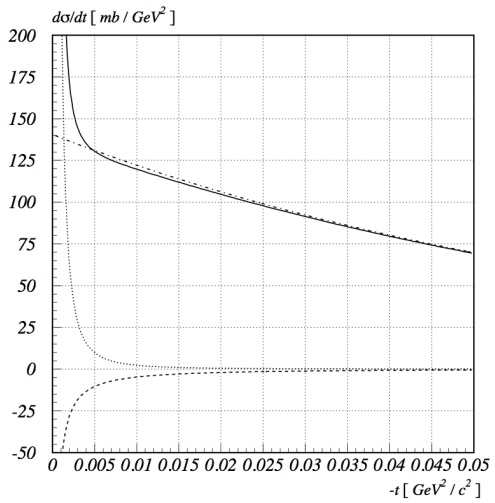

FIG. 50. Differential elastic cross section (solid line) as a function of $|t|$. The contribution from the Coulomb amplitude (dotted line), the hadronic amplitude (dash-dotted line) and the interference amplitude (dashed line) are also shown. The fixed parameters are $\sigma_{tot} = 51.6$ mb [9], $\rho = 0.13$ [10] and $B = 14.0$ c^2/GeV^2. Graph taken from [11].

7.1.3 NUCLEAR SLOPE OF THE FORWARD PEAK B

Restricted φ range t-distributions from selected elastic data sets were fitted with theoretical differential cross section functions given in Eq. (50) in limited $|t|$ ranges shown in Table 15. Nuclear slopes of the forward peak B obtained from "$pp2pp$ at STAR" Run9 are presented in Table 16. Results presented are obtained from corrected elastic $|t|$-distributions as explained in Chapter 6. Correction functions of each data set and both horizontal arms are presented on Figs. 51 to 55 also.

Statistical analysis of the χ^2 goodness of the fit shows that nuclear slopes from two detector arms are in good statistical agreement with above 70% confidence levels and can therefore be averaged. The necessity for averaging these two nuclear slope values comes from uncertainties in $|t|$ of the two horizontal detector arms. Furthermore, results obtained from all data sets are cross-checked for compatibility. χ^2 statistical analysis was done to check if deviations between obtained B results is statistically significant. This analysis is done on the sample of results obtained from

two horizontal detector arms and on the sample of results obtained from five selected data sets (see Table 16). This analysis shows that observed deviations from the null hypothesis (nuclear slope B results are compatible) are not significant. Consequently, the nuclear slope B results obtained from either two horizontal detector arms or five data sets can be averaged.

TABLE 16. The slope parameter B results obtained from experimental data sets. χ^2 values are obtained from two different $\chi^2(\text{ndf}=1)$ and $\chi^2(\text{ndf}=4)$ distributions with their corresponding p-values ($P_{\chi^2}(\text{ndf})$) and represent tests of the null hypothesis for the B results obtained from two detector arms and five data sets respectively. Each p-value in this table shows non significant deviation from the null hypothesis (observed B values in the sample are compatible).

Data set	-B $(\text{GeV/c})^{-2}$		χ^2(ndf=1)	P_{χ^2}(ndf=1)
	EHI-WHO	EHO-WHI		
0	13.8±0.4	13.7±0.4	0.03	86 %
1	14.6±0.5	14.5±0.6	0.016	90%
4	13.6±0.6	13.7±0.9	0.009	92%
6	13.6±0.7	13.3±1.0	0.06	81%
9	14.2±0.5	13.9±0.6	0.15	70%
Mean	**14.0±0.2**	**13.9±0.3**	0.076	78%
χ^2(ndf=4)	2.3	1.71		
P_{χ^2}(ndf=4)	68%	79%		
Average Mean	**14.0±0.2**			

The slope parameter for "*pp*2*pp* at STAR" Run9 data sample is

$$B = (14.0 \pm 0.2)\ \frac{c^2}{\text{GeV}^2}$$

No error analysis has been applied here. The error used by the fitting program is given by the statistics of each bin in $|t|$. Following figures show fits to the limited $|t|$-ranges (see Table 15); $-0.5 \leq \varphi \leq 0.5$ or $-2.7 \geq \varphi \geq 2.7$ is also indicated.

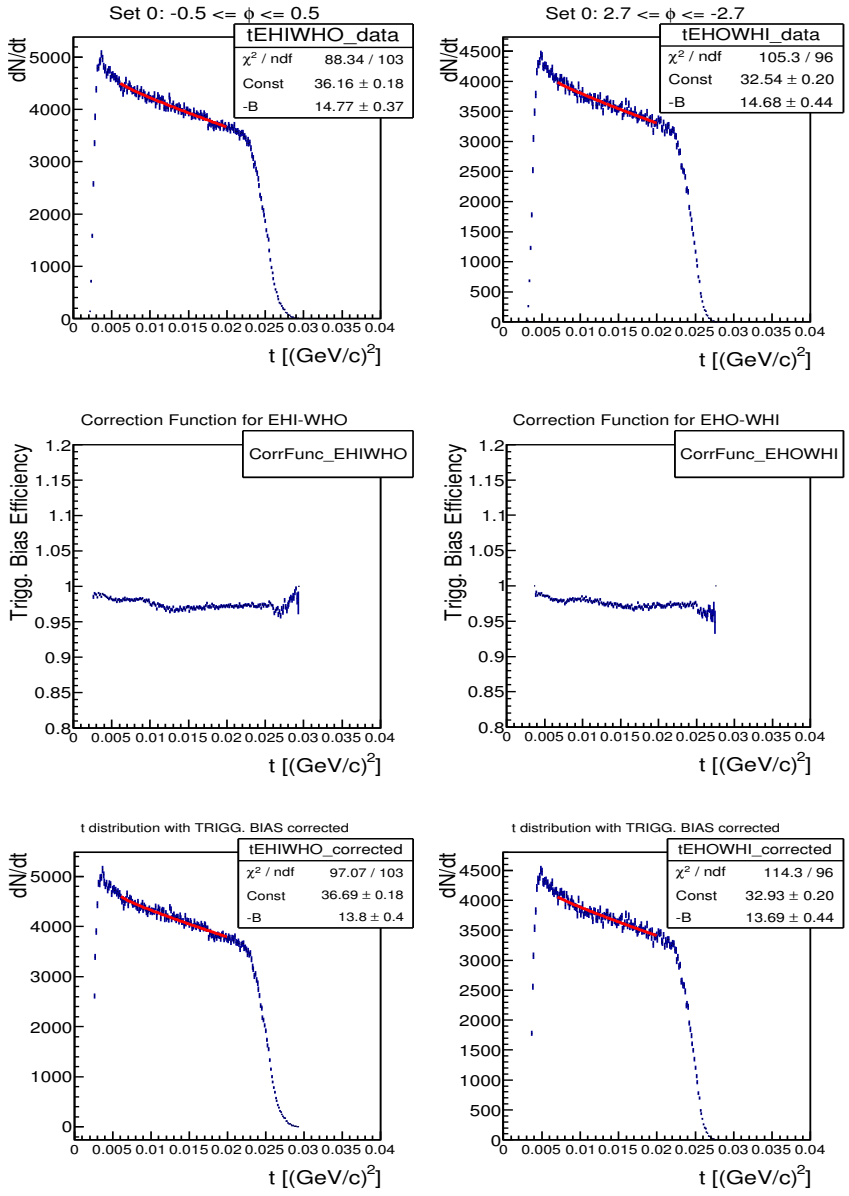

FIG. 51. Detector position set No. 0: $|t|$-distribution for arm EHI-WHO (top left) and EHO-WHI (top right) after applying a cut in φ as described in the text. Generated simulation correction function for arm EHI-WHO (middle left) and EHO-WHI (middle right) after applying a cut in φ as described in the text. Corrected $|t|$-distribution for arm EHI-WHO (bottom left) and EHO-WHI (bottom right) after applying a cut in φ as described in the text.

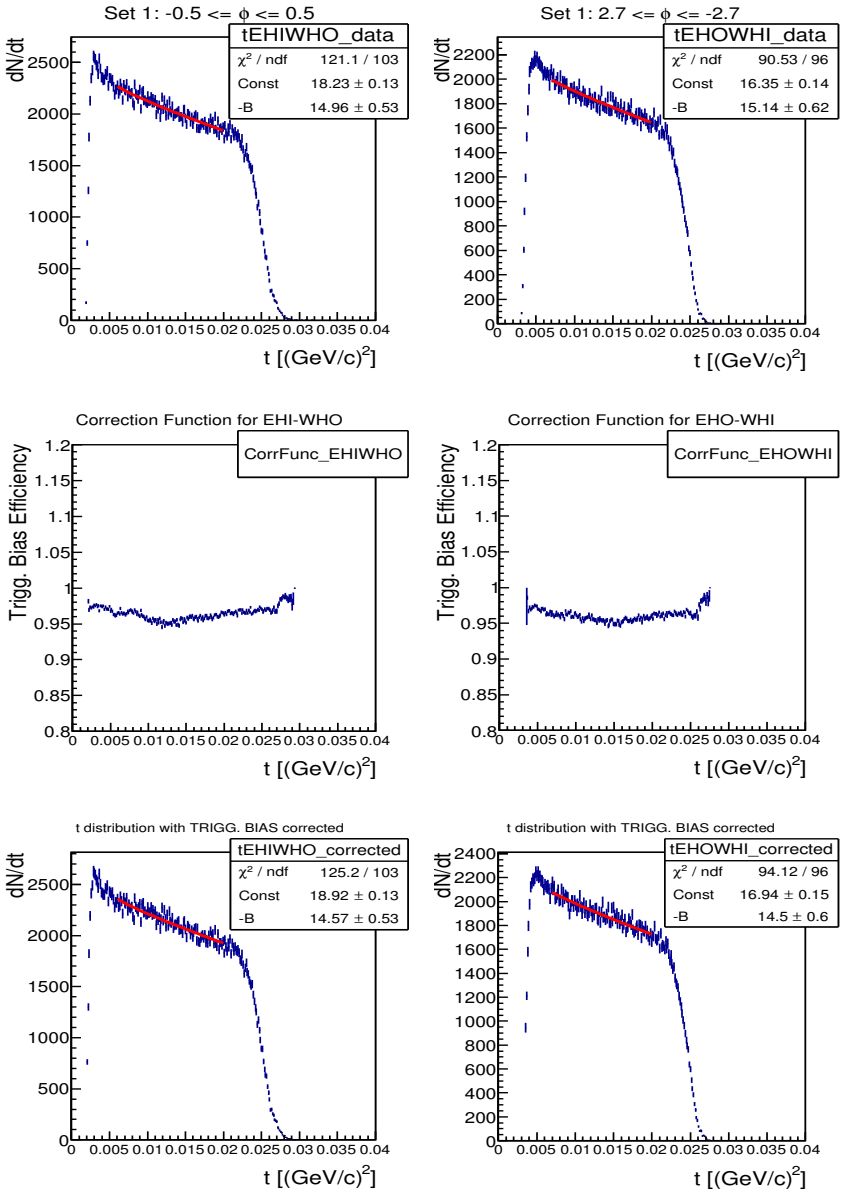

FIG. 52. Detector position set No. 1: $|t|$-distribution for EHI-WHO arm (top left) and EHO-WHI (top right) after applying a cut in φ as described in the text. Generated simulation correction function for EHI-WHO arm (middle left) and EHO-WHI (middle right) after applying a cut in φ as described in the text. Corrected $|t|$-distribution for EHI-WHO arm (bottom left) and EHO-WHI (bottom right) after applying a cut in φ as described in the text.

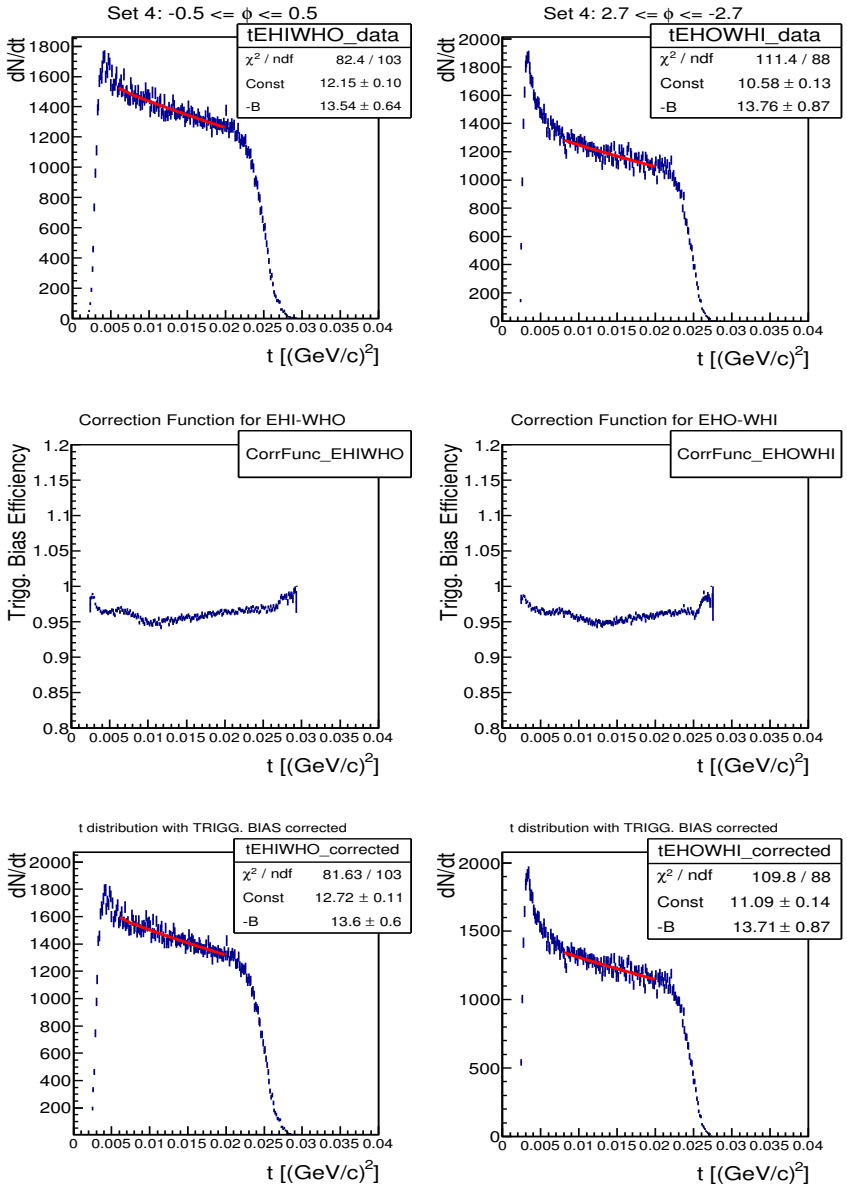

FIG. 53. Detector position set No. 4: $|t|$-distribution for EHI-WHO arm (top left) and EHO-WHI (top right) after applying a cut in φ as described in the text. Generated simulation correction function for EHI-WHO arm (middle left) and EHO-WHI (middle right) after applying a cut in φ as described in the text. Corrected $|t|$-distribution for EHI-WHO arm (bottom left) and EHO-WHI (bottom right) after applying a cut in φ as described in the text.

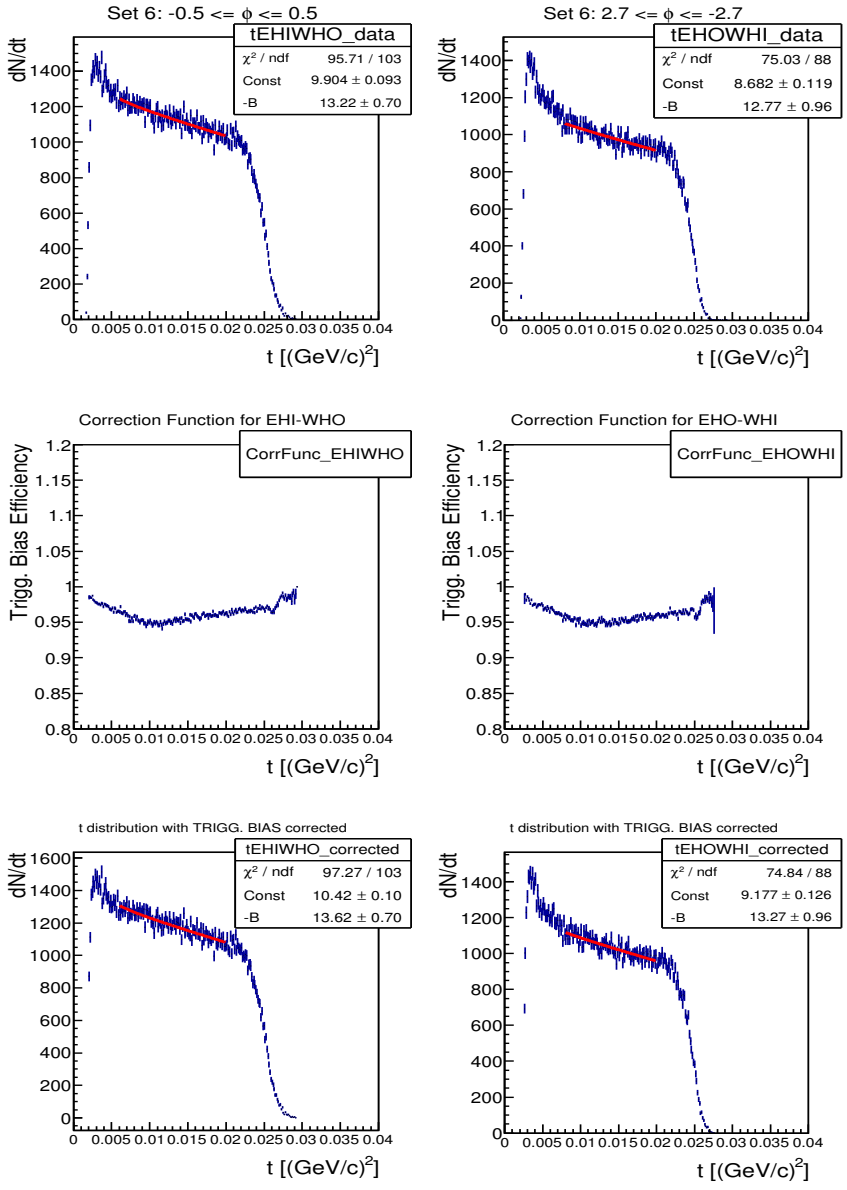

FIG. 54. Detector position set No. 6: $|t|$-distribution for EHI-WHO arm (top left) and EHO-WHI (top right) after applying a cut in φ as described in the text. Generated simulation correction function for EHI-WHO arm (middle left) and EHO-WHI (middle right) after applying a cut in φ as described in the text. Corrected $|t|$-distribution for EHI-WHO arm (bottom left) and EHO-WHI (bottom right) after applying a cut in φ as described in the text.

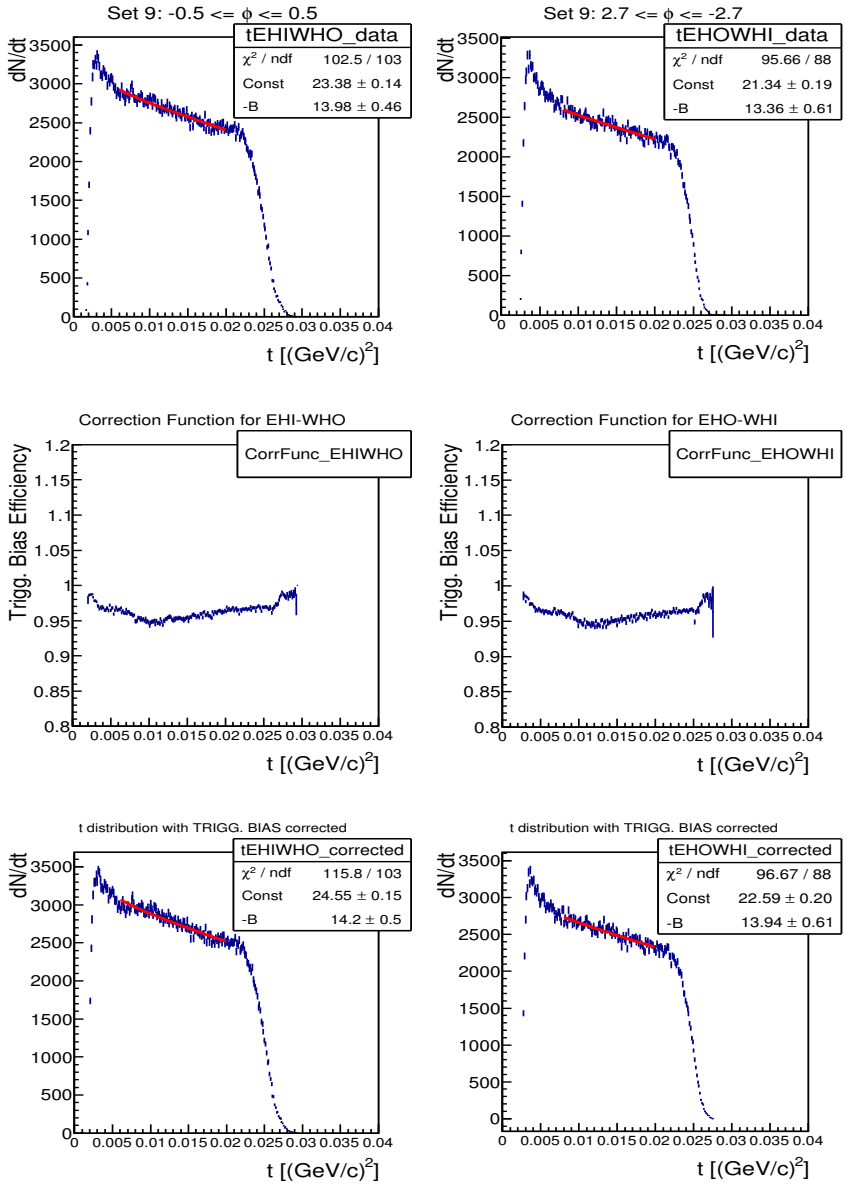

FIG. 55. Detector position set No. 9: $|t|$-distribution for EHI-WHO arm (top left) and EHO-WHI (top right) after applying a cut in φ as described in the text. Generated simulation correction function for EHI-WHO arm (middle left) and EHO-WHI (middle right) after applying a cut in φ as described in the text. Corrected $|t|$-distribution for EHI-WHO arm (bottom left) and EHO-WHI (bottom right) after applying a cut in φ as described in the text.

During careful reconstruction of $|t|$-distributions, further limitations of $|t|$ ranges were investigated to exclude ranges polluted with particles of the beam halo (so called hot spots). From Figs. 51 to 55 we find that detecting EHO-WHI arm was more exposed to this systematic effect. This can be seen by the increase in the number of events at lower $|t|$ and can not be explained by domination of the Coulomb interaction.

CHAPTER 8

SYSTEMATIC UNCERTAINTIES

This Chapter covers the different systematical uncertainties of this experiment which contribute to the uncertainty of the nuclear slope of the forward peak B at $\sqrt{s} = 200$ GeV^2/c^2 in the Coulomb-Nuclear Interference $|t|$ region (CNI). These systematical uncertainties can be divided in two groups:

1. **Uncertainties affecting the determination of kinematic variables: four-momentum transfer squared $|t|$ and azimuthal angle φ.**

   - **Uncertainties related to the transport matrices used in this experiment: the uncertainty in the transport matrix element L_{eff}.**
   - **Beam and Roman pot geometry and/or alignment related uncertainties:**.
     - Uncertainty in the beam transverse position at IP (x_0, y_0)
     - Uncertainty of the beam angular divergence and unknown beam crossing angle
     - Beam position shift from the center at the Roman pot location
     - Offsets effects due to accelerator optics elements such as kicker magnets located before the Roman Pot locations
     - Uncertainties related to the Roman pot survey

2. **Uncertainties affecting the slope of the forward peak B**

   - **All of the above plus uncertainties in the fitting parameters:** the total cross section σ_{tot}, the ratio of the real to the imaginary parts of the scattering amplitude ρ.
   - **Background**
   - **Geometrical acceptance and tracking efficiencies**
   - **Triggering (TAC) efficiencies**

8.1 UNCERTAINTIES AFFECTING THE DETERMINATION OF KINEMATIC VARIABLES $|t|$ AND φ

8.1.1 UNCERTAINTIES IN THE TRANSPORT MATRIX ELEMENT L_{eff}

The effective length transport matrix element L_{eff}, Eq. (95), is the major term in the transport matrix. It represents the magnification of the scattering angle θ. The uncertainty in the determination of the value of L_{eff} is deduced from the uncertainty of the magnetic field strength of the Q_2 and Q_3 focusing magnets, which is a result of the calibration of their magnet current measurements. A correction to the magnet field strength was determined by analyzing the position and angle of the elastic events falling in the overlapping acceptance region of the horizontal and vertical Roman pots. An overall correction was applied to the magnetic field strength of the Q_2 and Q_3 quadrupoles of the order of 0.5%. This results in a 1.5% uncertainty in the value of L_{eff}. The next step is to determine how the uncertainty in L_{eff} propagates to the uncertainty in $|t|$.

Simplified transport matrix equations, which relate scattering angles θ_x^{IP} and θ_y^{IP} with x and y positions at the detection region, are given in Eq. (108). This approximation of Eqs. (95) is allowed only when transport matrix elements a_{11}, a_{13}, a_{14} and a_{31}, a_{32}, a_{33}, respectively, have very small values:

$$\begin{aligned} x &\approx L_{eff}^{x} \cdot \theta_x^{IP} \\ y &\approx L_{eff}^{y} \cdot \theta_y^{IP}. \end{aligned} \tag{108}$$

Furthermore, $\sigma_{L_{eff}}$ is an uncertainty in L_{eff} and L_{eff}^{x} and L_{eff}^{y} are, by approximation, the same. The polar angle is then given by:

$$\theta \approx \sqrt{(\theta_x^{IP})^2 + (\theta_y^{IP})^2} \approx \frac{\sqrt{x^2 + y^2}}{L_{eff}} \tag{109}$$

Errors in detection positions and L_{eff}, namely σ_x, σ_y and $\sigma_{L_{eff}}$, propagate to the error in scattering angle θ as follows:

$$\begin{aligned} \sigma_\theta^2 &= \sigma_{\theta_{x,y}}^2 + \sigma_{\theta_{L_{eff}}}^2 \\ \sigma_{\theta_{x,y}}^2 &= \left(\frac{\delta\theta}{\delta x} \cdot \sigma_x\right)^2 + \left(\frac{\delta\theta}{\delta y} \cdot \sigma_y\right)^2 \\ \sigma_{\theta_{L_{eff}}}^2 &= \left(\frac{\delta\theta}{\delta L_{eff}} \cdot \sigma_{L_{eff}}\right)^2. \end{aligned} \tag{110}$$

With a little bit of algebra, by using Eqs. (109) and (110), the propagated uncertainty in the scattering angle θ due to the uncertainty in the transverse positions x, y and the uncertainty in θ due to the uncertainty in L_{eff} can be obtained (see Eq. (111)):

$$\begin{aligned} \sigma^2_{\theta_{x,y}} &= \frac{\sigma^2}{L^2_{eff}} \\ \sigma^2_{\theta_{L_{eff}}} &= \frac{(\sigma \cdot \sigma_{L_{eff}})^2}{L^2_{eff}}. \end{aligned} \tag{111}$$

Consequently, by starting with the simplified equation for the four-momentum transfer squared ($-t = p^2\theta^2$) and its derivative with respect to θ scattering angle ($\Delta(-t) = 2p^2\theta \cdot \Delta\theta$), one can obtain the uncertainty in momentum transfer squared t due to the transverse positions x, y and L_{eff}:

$$\frac{\Delta(-t)}{-t} = \frac{2p^2\theta \cdot \Delta\theta}{p^2\theta^2} = \frac{2\Delta\theta}{\theta}, \tag{112}$$

where

$$\Delta\theta = \frac{\sigma_\theta}{\sqrt{2}} \tag{113}$$

is the error on the average scattering angle $\theta_{\text{ave}} = \frac{\theta_{\text{East}} + \theta_{\text{West}}}{2}$, assuming that errors on θ_{East} and θ_{West} are uncorelated.

Using Eq. (111) we get:

$$\frac{\Delta\theta}{\theta} = \frac{\sigma_{\theta_{x,y}}}{\sqrt{2}\theta} = \frac{\sigma_{L_{eff}}}{\sqrt{2}L_{eff}}. \tag{114}$$

The uncertainty in L_{eff} is 1%, $\sigma_{L_{eff}}/L_{eff}$ is 0.01. Therefore, the uncertainty in t due to the uncertainty in the value of L_{eff} is 1.4%.

8.1.2 UNCERTAINTIES IN ROMAN POT ALIGNMENT/GEOMETRY AND BEAM RELATED UNCERTAINTIES

The error in t due to the spatial uncertainty, σ_x and σ_y, or in other words the error in t-scale due to the uncertainty in geometry or alignment of the Roman pot detectors used in this experiment is given with:

$$\frac{\Delta(-t)}{-t} = \frac{2p^2\theta\Delta\theta}{p^2\theta^2} = \frac{2p\Delta\theta}{p\theta} = \frac{2p\Delta\theta}{\sqrt{-t}} = \frac{2p\sigma_\theta}{\sqrt{2}\sqrt{-t}} = \frac{\sqrt{2}p\sigma_\theta}{\sqrt{-t}}, \tag{115}$$

where σ_θ is given in Eq. (111). σ represents the uncertainty in the alignment/geometry. The alignment of the detectors was established initially by

using the survey information and then by introducing corrections using a study of elastic events which fall in the overlapping acceptance region of horizontal and vertical Roman pots, as described in [77]. The need to precisely know the positions of detectors with respect to the beam center comes from the fact that the reference point for the scattering angle is the beam center itself. On the other hand, the position of the beam center is not well known. Other parameters of the beam are unknown also, i.e. the beam transverse position at the IP (x_0, y_0). Additionally, it is very difficult to separate the beam angular divergence from the beam crossing angle. Therefore, the final correction to the survey alignment was applied to take into account all the above-mentioned geometrical unknowns and uncertainties, including also the survey errors. The corrections were determined by simulating the transport of elastically scattered protons through the RHIC magnets. The effect of the magnet apertures on the trajectories of the elastically scattered protons was studied and compared to the data. A comparison between simulation and the data, mainly of the distributions and their acceptance boundaries, led to "correction" shifts to the proton positions at the detection point of $(\Delta x_{\text{East}}, \Delta y_{\text{East}}) = (2.5, -1.5)$mm in Yellow (East) beam Roman pot stations only. The uncertainty of this correction is about 400 μm which, together with Eq. (115), leads to the uncertainty in t due to geometry of about $0.002/\sqrt{-t}$.

8.1.3 SYSTEMATIC UNCERTAINTY DUE TO THE BEAM ANGULAR DIVERGENCE

The uncertainty in the t-scale is mostly due to the beam angular divergence. To calculate the uncertainty in the t-scale from the angular beam divergence we can start from using the expression for the momentum transfer squared t:

$$-t = p^2\theta^2. \tag{116}$$

Taking the first derivative with respect to θ, the uncertainty on t due to beam angular divergence is then:

$$\delta(-t) = 2p \times \sqrt{t} \times \delta(\theta), \tag{117}$$

where the beam momentum $p = 100.2$ GeV/c and $\delta(\theta) = 54$ μrad based on the study of the elastic event distributions $\delta(\theta)$, calculated as a weighed average (all runs) of the σ of the $\delta(\theta)$ distribution of each elastic arm. This gives a value for $\delta(t)$ due to

the beam angular divergence of

$$\delta(t) \approx 0.011 \left[\frac{\text{GeV}}{\text{c}}\right] \times \sqrt{t}. \tag{118}$$

8.2 UNCERTAINTIES AFFECTING THE SLOPE OF THE FORWARD PEAK B

8.2.1 BACKGROUNDS

The origins of the backgrounds in this experiments are related to several sources such as beam-gas interactions, particles that originate from the beam halo or inelastic events. If these events are not excluded from the analysis sample, they may affect the extracted nuclear slope B value. In order to prevent this from happening, the co-linearity condition was used during the data selection procedure. The χ^2 analysis removes a large portion of non-elastic events (see Chapter 5.1.11).

Additionally, during the estimate of the t-ranges used for fitting of the extracted elastic t-distributions, regions of low-t were avoided due to the presence of so called "hot spots" or in other words, regions highly populated with events that originated from the beam halo.

8.2.2 UNCERTAINTIES IN THE FITTING PARAMETERS: ρ AND σ_{tot}

The least squares fit for the nuclear slope parameter B uses nominal values for ρ and σ_{tot}. Our estimates of uncertainties related to variations in these parameters are found to be $\frac{\delta B}{\delta \rho} = 16$ (c^2/GeV^2) and $\frac{\delta B}{\delta \sigma_{tot}} = -.016$ (c^2/GeV^2)/mb, respectively. Consequently, changes in ρ and σ_{tot} of about 10% results in negligible changes in slope parameter B.

8.2.3 UNCERTAINTIES RELATED TO TRIGGERING LOGIC (TAC)

The largest contribution to the uncertainty of the slope parameter B comes from the trigger timing cut-off. Understanding of TAC logic mechanism is of importance for the slope extraction. The TAC cut-off, or in other words, decrease in triggering efficiency, biases our experimental data and consequently our nuclear slope parameter B [12].

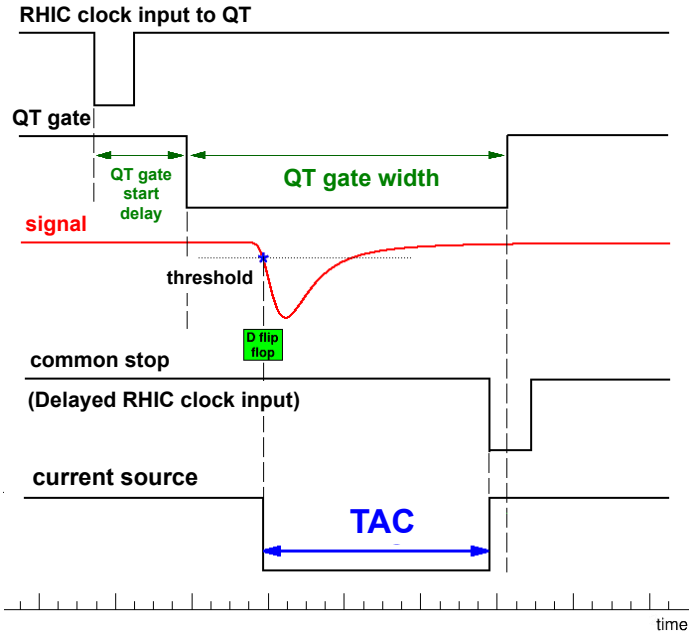

(a) Example of a leading edge PMT signals with respect to the QT gate start [12].

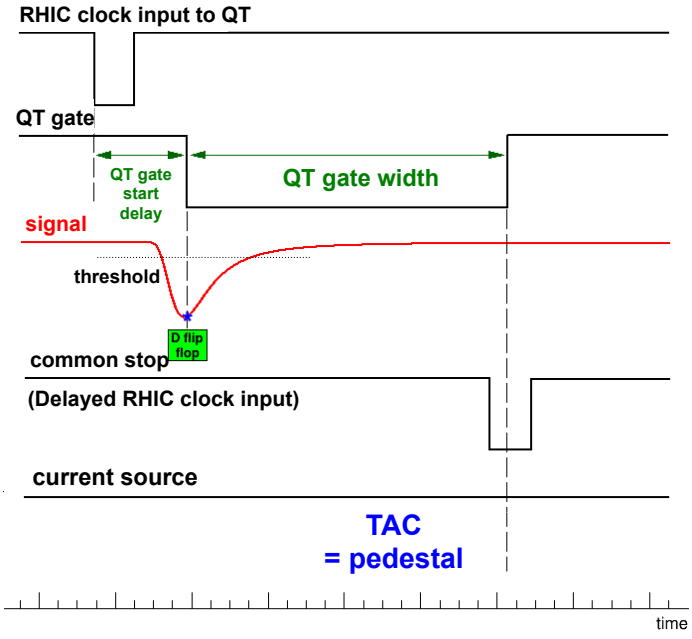

(b) Example of a trailing edge (early arrival) PMT signals with respect to the QT gate start [12].

FIG. 56. Working principle of the QT and TAC electronics. Images curtesy of R. Sikora [12].

The triggering system is described in Chapter 3. It consisted of one scintillator, two photomultiplier tubes and QT and TAC boards [12], for controlling our trigger logic settings. Figs. 56(a) and 56(b) illustrate timing settings during "*pp*2*pp* at STAR" Run9. The general idea behind the trigger setup is following:

1. QT gate is started by RHIC clock input.
2. PMT signal arrival and check whether the signal is above threshold.
3. D flip-flop device checks for the timing of arrival of the PMT signal i.e. whether the signal was on the leading or the trailing edge.
4. If the PMT signal was on the leading edge, discriminator fires and current source starts charging a capacitor.
5. Collected charge is converted into TAC value.

A very important property of the triggering mechanism is that even though PMT signals are "level triggered" they go through a "D flip-flop" device which passes them through only if the triggering point lays on their leading edge. Thus, in the case of an early arrival of the PMT signals with respect to the gate starts, even at the moment of the gate openings and even if they were above the set threshold, the source would not fire and charge a capacitor and TAC will be assigned the pedestal value (see Fig. 56(b)).

Due to early PMT signal arrivals with respect to the gate starts, i.e. early collisions or shifted vertex etc., certain fraction of events were not triggered and were, therefore, lost which decreased detection/tracking efficiency of our Roman pot system.

Fig. 57 shows one example of the typical TAC signal distributions for the two PMTs of one Roman pot detector package. The TAC trigger levels setup in RHIC Run9 are presented in Chapter 5.1.9. Pre-set TAC ranges in Run9 were $100 \leq \mathrm{TAC_{i,j}} \leq 1700$ and $\mathrm{ADC} \geq 5$ for ether of the PMTs of one Roman pot detector package. All the events that fall into this range were accepted. However, one can observe "cut-offs" in the distribution at the levels above $\mathrm{TAC_{i,j}} \geq 1200$ and a portion of events in which first of the PMTs had appropriate trigger levels and the second did not (events on Fig. 57 with $\mathrm{TAC_{i,j}} \leq 100$).

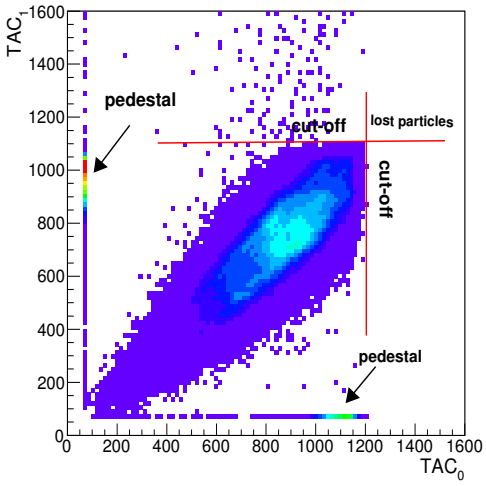

FIG. 57. TAC values from the two PMTs of one Roman pot package.

As previously described events that had early PMT signals were automatically assigned pedestal values ($TAC_{i,j} \leq 100$) and if this happened for both PMTs, these events were lost. This loss will have direct impact on the detecting efficiency and hence our reconstructed t-distributions and nuclear parameter B.

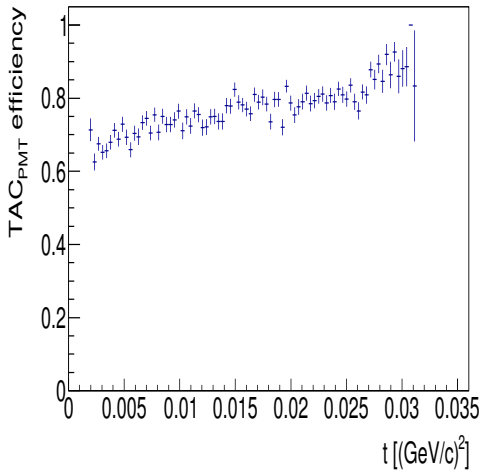

FIG. 58. TAC efficiency for one Roman pot package (preliminary). Image curtesy of R. Sikora, [12].

A qualitative study of this effect was performed [12]. This study is based on a GEANT4 Monte Carlo simulation of the Roman pot triggering system. An early estimate on trigger efficiencies related to TAC "cut-offs" show that low-t ranges are more influenced by this effect, Fig. 58.

A quantitative estimate of the uncertainty in nuclear parameter slope B from this study and in the fitting ranges according to Table 15 is about 10%. However, from Fig. 58, [12] it is clear that this uncertainty in B will not be symmetric. It is estimated that the nuclear parameter slope B is less likely to take smaller values from what is presented in Eq. (119).

8.2.4 UNCERTAINTY RELATED TO t-DEPENDENT CUTS ON φ

An independent analysis of the data was performed using different selections of hits and elastic events. In particular, a t-dependent cut on φ was applied, which allowed an increase in the t range and the number of accepted elastic events. This systematical effect is tightly related to the TAC trigger inefficiency. Thus, selecting wider φ cuts changes the B slope values. Obtained parameter slope values from both analyses agree within systematical TAC trigger errors.

8.3 THE EVALUATION OF THE SYSTEMATIC UNCERTAINTIES OF THE SLOPE PARAMETER B BASED ON MONTE CARLO SIMULATIONS

The evaluation of the systematic errors due to the uncertainty in beam emittance, vertex positions and spread, beam transport matrix elements, and incoming beam angles was based on Monte Carlo simulations. These simulations used the geometry of the experimental setup and efficiency of the detectors as an input. The largest source for the systematic error was the uncertainty of the initial colliding beam angles.

In order to estimate systematic uncertainties from this largest single source, upper limits on the initial beam angles obtained from the data were used and the possible shift of the t-distribution scale was studied. The horizontal component of a possible initial angle has a negligible effect on the t-distribution, while the vertical component leads to an uncertainty in the absolute value of t for the reconstructed protons. This resulted in an uncertainty on the fitted slope parameter of about 1.5% which agrees within statistical errors.

The Monte Carlo simulation used for the estimate of systematic errors due to

above effects follows these steps:

1. **Generation:**

   - **Random generation of t, φ values together with vertex position and its spread, z_0 and σ_{z_0} values.** The four momentum transfer squared $|t|$ was generated from both uniform and also form distributions determined by the equation for the differential elastic cross-section (see Eq. (34)) with ρ, σ_{tot} and B parameters fixed to the expected values obtained from extrapolation of all available experimental data. Simulated $|t|$ range was between 0.001 GeV$^2/c^2$ and 0.04 GeV$^2/c^2$. The φ angle was generated as a uniform random distribution of numbers between 0 and 2π. Vertex positions z_0 and σ_{z_0} were generated as normal distributions with requirement to match experimental vertex shifts and spread.

   - **Calculating scattering angles from generated t and φ distributions and smearing of calculated angle values using the angular beam divergence value from RHIC Run9.** Angular beam divergences were varied by changing eminence values between $\pi \leq \varepsilon \leq 15\pi$.

     $\sigma_\theta(\varepsilon)$-angular beam dvergence,
     $\theta^{IP} = \sqrt{t}/p^2$,
     $\theta_x^{IP} = \text{atan}(\tan\theta\cos\varphi) + \text{Gauss}(0, \sigma_\theta(\varepsilon))$
     $\theta_y^{IP} = \text{atan}(\tan\theta\sin\varphi) + \text{Gauss}(0, \sigma_\theta(\varepsilon))$

   - **Addition of crossing angles, calculating "generated" x_0 and y_0 beam shifts.**

     $\theta_{x,y}^{IP}(\text{tot}) = \theta_{x,y}^{IP}(\text{scattering}) + \theta_{E,W}(\text{crossing})$
     $x_0^{gen} = z_0 \cdot \tan\theta_x^{IP}(\text{tot})$
     $y_0^{gen} = z_0 \cdot \tan\theta_y^{P}(\text{tot})$

   - **Recalculation of transport matrix elements based on vertex z_0 positions.**

     $a_{12} = a_{12} + z_0 \cdot a_{11}$
     $a_{14} = a_{14} + z_0 \cdot a_{13}$
     $a_{32} = a_{32} + z_0 \cdot a_{31}$

$$a_{34} = a_{34} + z_0 \cdot a_{33}$$

- **"Propagation" of scattering angles and positions to the Roman pot detection point while checking $Q_2^{(E;W)}$ and $Q_3^{(E;W)}$ acceptances.**

$$\begin{bmatrix} x^{RP} \\ \theta_x^{RP} \\ y^{RP} \\ \theta_y^{RP} \end{bmatrix} = TM^{gen}_{(W;E)/(H;V)} \begin{bmatrix} x_0 \\ \theta_x^{IP} \\ y_0 \\ \theta_y^{IP} \end{bmatrix}$$

2. **Reconstruction:**

- **Additional smearing of reconstructed positions at the detection point to simulate uncertainty of detected particle positions.** Δx_{RP} and Δy_{RP} are kicker and alignment corrections and $\sigma_{x;y}^{RP}$ is the position uncertainty. This detected position uncertainty was determined from the experiment and was set to be about 400μm while kicker and alignment corrections were set as in the experiment.

$$x'_{RP} = x^{RP} + \text{Gauss}(\Delta x_{RP}, \sigma_{x;y}^{RP})$$
$$y'_{RP} = y^{RP} + \text{Gauss}(\Delta y_{RP}, \sigma_{x;y}^{RP})$$

- **Calculation of scattering angles at the IP using reconstruction TM coefficients: $A_{x;y}$, $B_{x;y}$, $C_{x;y}$, $D_{x;y}$.** Scattering angles at the IP were reconstructed using the equations below and generated crossing angles were subtracted. Transport matrix coefficients were calculated by the use of slightly changed transport matrices to simulate the uncertainties in transport matrix elements. The difference was 1% in leading terms. Furthermore, an uncertainty in (x_0^{rec}, y_0^{rec}) was introduced to incorporate any scattering angle miscalculation that may have occurred due to the lack of knowledge of the beam positions at the IP in the reconstruction procedure.

$$\theta_x^{IP}(rec) = A_x \cdot x'^{RP} + B_x \cdot y'^{RP} + C_x \cdot x_0^{rec} + D_x \cdot y_0^{rec}$$
$$\theta_y^{IP}(rec) = A_y \cdot y'^{RP} + B_y \cdot x'^{RP} + C_y \cdot y_0^{rec} + D_y \cdot x_0^{rec}$$

3. **Uncertainties estimates:** The uncertainties of individual effects such as the beam emittance, vertex positions and spread, beam transport matrix elements, and incoming beam angles or any of their combinations are estimated in the t-space by plotting $\Delta t/t_{gen}$ vs. t_{gen}, where $\Delta t = t_{rec} - t_{gen}$. As previously

described, the resulting uncertainty of all effects above and in the range of t given in Table 15, was estimated to be of the order of up to 1.5% which is illustrated on Fig. 59.

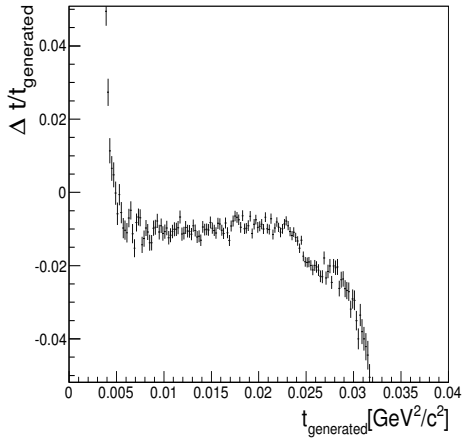

FIG. 59. Resulting uncertainty due to the uncertainty in beam emittance, vertex positions and spread, beam transport matrix elements, and incoming beam angles.

The total systematic error was calculated by adding in quadrature all the above described systematic errors. As previously described, the major contributions to overall uncertainty of this work are due to triggering logic and the choice of t-dependent φ ranges of the selected elastic data sample. Total systematic and total (syst. + stat.) errors are presented in Chapter 9.

CHAPTER 9

SUMMARY AND CONCLUSIONS

We present here the measurement of the slope parameter B in forward proton-proton elastic scattering obtained by the "Physics With Tagged Forward Protons At STAR", formerly known as the "*pp*2*pp* at STAR" experiment at the Relativistic Heavy Ion Collider (RHIC) in the squared four-momentum transfer range $0.006 \leq |t| \leq 0.02$ GeV$^2/c^2$ at $\sqrt{s} = 200$ GeV/c.

The "*pp*2*pp* at STAR" experiment is designed to measure polarized pp elastic scattering and diffractive dissociation at RHIC in the squared four-momentum transfer range $4 \times 10^{-4} \leq |t| \leq 1.3$ GeV^2/c^2 and $50 \leq \sqrt{s} \leq 500$ GeV/c. The measurements of elastic scattering in the non-perturbative regime of QCD at RHIC allows us to probe the exchanged mediators of the force, the *Pomeron* and its odd C-parity partner, the *Odderon*. This experiment addresses one of the main unsolved problems in particle physics: long range QCD and confinement.

The slope parameter B in the squared four-momentum transfer range $|t| \leq 0.05$ GeV^2/c^2 is sensitive to the exchange process and its $\sqrt{s}$-dependence allows us to distinguish among various QCD based models of hadronic interactions. Furthermore, observation of the B slope parameter in pp collisions at the RHIC energies will allow comparison with some interesting features of B observed in the case of $p\bar{p}$ elastic scattering. It is of interest to see the B behavior in the RHIC energy range and compare the values of B for the cases of pp and $p\bar{p}$ elastic scattering. This interest is due to the fact that $|t|$ distributions of the pp and $p\bar{p}$ elastic scattering become less steep as $|t|$ increases from 0.02 to 0.20 GeV^2/c^2 which was not observed at higher energies.

At RHIC the two protons collide at six interaction regions. Since the elastic scattering angles are very small, scattered protons stay within the beam pipes of the accelerator. Their trajectories are determined by the accelerator "optics" until they reach the detectors which measure their positions. The coordinates of proton positions are related to the scattering angles at the IP by the beam transport equations, Eqs. (95). The optimum condition for this experiment is to minimize the dependence of the measured coordinates on the unknown collision vertex which

is called "parallel to point focusing". By tuning the accelerator optics, this desired condition is achieved, which simplifies Eqs. (95).

The data presented here were recorded during several days of "*pp*2*pp* at STAR" Run9 (run of 2009). The squared four-momentum transfer range was $0.006 \leq |t| \leq 0.02$ GeV$^2/c^2$ at $\sqrt{s} = 200$ GeV/c.

The identification of recorded elastic events was based on a co-linearity condition and thus, it required simultaneous detection of two co-linear protons on either side of the interaction point. To achieve this, the use of co-linear Roman pot detectors was needed. Roman pots are cylindrical vessels carrying four silicon micro-strip detectors. They can be inserted inside beam pipes without disturbing the accelerator vacuum allowing four silicon detectors to be positioned very close to the proton beam orbits. The layout and description of our detector system is shown in Chapter 3.

In the time span of the "*pp*2*pp* at STAR" Run9 about 30 million elastic triggers were recorded. To reduce the contamination of the elastic event sample with tracks from background particles we applied a range of selection criteria which reduced the event sample, leaving about 22 million elastic events. For each event the squared four-momentum t and azimuth φ were calculated and then averaged. A restriction of the φ range and the dN/dt distribution corrections using Monte Carlo methods led to a uniform geometric acceptance in a limited t-range. The determination of the slope parameter B is confined to the t regions given in Table 15.

Least squares fits were performed to the distributions of Figs. 51 to 55 using Eq. (106) with B and a normalization constant as free parameters. Since the total cross section σ_{tot} and ρ parameters have not been measured in this study, we have used values from fits to the existing pp and $p\bar{p}$ data. We used $\sigma_{tot} = 51.6$ mb [9] and $\rho = 0.13$ [10], which agree with the predictions from other models [87], [86], [88] and [89].

We report our measurement of the nuclear slope parameter B obtained from the RHIC Run9 in the squared four-momentum transfer range $0.006 \leq |t| \leq 0.02$ GeV^2/c^2 at $\sqrt{s} = 200$ GeV/c to be:

$$B = 14.0 \pm 0.2 \text{ (stat.)} \begin{matrix} +1.4 \text{ (syst.)} \\ -0.2 \text{ (syst.)} \end{matrix} (\text{GeV/c})^{-2}. \tag{119}$$

This result is presented in Fig. 60 together with the first slope parameter result reported by the "*pp*2*pp*" collaboration in 2004 [13] and the world data on elastic pp and $p\bar{p}$ scattering.

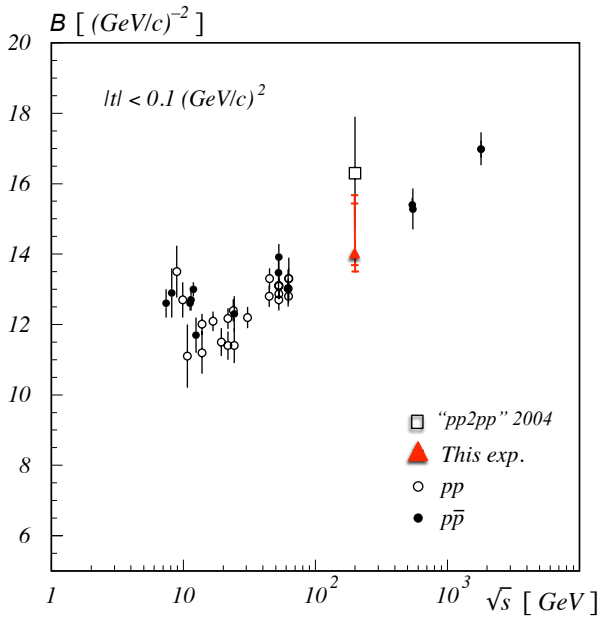

FIG. 60. Nuclear slope parameter B for this experiment (red triangle) compared to the world pp and $p\bar{p}$ data set. The asymmetric error displayed for our result includes both statistical and systematic uncertainties, which have been computed by a quadrature sum. The open square represents the "$pp2pp$" result from 2004 [13].

Evaluation of the systematic errors due to the vertex positions and spread, uncertainty in beam emittance, beam transport matrix elements, and incoming beam angles was based on Monte Carlo simulations (see Chapter 8). The major contributions to the overall uncertainty of this work are due to the timing of PMT signals [12] and the choice of a t-dependent φ range of the selected elastic data sample and the uncertainty of the initial colliding beam angles. The total systematic uncertainty was calculated by a quadrature sum of all the above systematic errors. Total systematic and total (syst. + stat.) errors are presented in Fig. 60.

TABLE 17. Systematic errors in B-nuclear slope parameter (δB) due to systematic uncertainties in beam emittance ($\delta\varepsilon$), vertex position and spread (δx_0, δy_0, δz_0 and $\delta\sigma_{z_0}$), beam transport matrix elements (δL_{eff}), beam crossing angles ($\delta\theta^{IP}_{cross.}$), and timing of PMT signals (δTAC_{PMT}). The total systematic experimental uncertainty has been computed by a quadrature sum.

δB	$\frac{c^2}{\mathrm{GeV}^2}$
$\delta\varepsilon$	
δx_0, δy_0	
δz_0, $\delta\sigma_{z_0}$	± 0.2
δL_{eff}	
$\delta\theta^{IP}_{cross.}$	
δTAC_{PMT}	$+1.4$
Total Syst.	$+1.4$
	-0.2

The "Physics With Tagged Forward Protons At STAR" experiment is entering its Phase-II* ($*$ - initial stage of the "*pp2pp* at STAR" Phase-II). In this new experimental phase wider kinematic coverage is expected to be achieved. The new, redesigned vertically oriented Roman pot detectors will be mounted each at 15.2 m and 17.3 m which will allow high luminosity sampling, clean trigger and tight constraint in exclusivity of the event and parallel running with other experiments of the STAR detector with collaboration. Some of the physics processes to be covered with Phase-II* are spin dependent elastic processes up to the "dip" region, central exclusive diffraction (double *Pomeron* exchange), polarized ^{3}He + p and other processes.

BIBLIOGRAPHY

[1] T. Obrebski, *Energy minimum cuts analysis*, Brookhaven National Laboratory STAR Collaboration Technical Note (unpublished) (2010).

[2] H. Cheng and T. T. Wu, *Expanding Protons: Scattering at High Energies* (The MIT Press, 1987).

[3] G. Antchev *et al.* (TOTEM collab.), Europhys. Lett. **101** (2013).

[4] G. Antchev *et al.* (TOTEM collab.), Phys. Rev. Lett. **111** (2013).

[5] V. Barone and E. Predazzi, *High Energy Particle Diffraction* (Springer-Verlag, 2002).

[6] L. Adamczuk *et al.*, Phys. Lett. B **719**, 62 (2013).

[7] N. Guler, *Performance Characterization Of The Silicon Microstrip Detectors Of PP2PP Experiment*, Master's thesis, University of Texas at Arlington (2001).

[8] R. Sikora, *Simulation of Trigger Efficiency and Bias in 2009*, Brookhaven National Laboratory STAR Collaboration Technical Note (unpublished) (2013).

[9] A. Donnachie and P. V. Landshoff, Phys. Lett. B **296**, 227 (1992).

[10] C. Augier et al. (UA4/2 collab.), Phys. Lett. B **315, 316**, 448, 503 (1993).

[11] S. Bültmann, *Status of the Analysis of Elastically Scattered Protons*, Brookhaven National Laboratory STAR Collaboration Technical Note (unpublished) (2003).

[12] R. Sikora, *TAC properties and efficiency in pp2pp 2009 data*, Brookhaven National Laboratory STAR Collaboration UPC group presentation (unpublished) (2013).

[13] S. Bültmann *et al.* (pp2pp collab.), Phys. Lett. B **579**, 245 (2004).

[14] H. Abramowitz, H. Brtels, L. Frankfurt, and H. Jung, *Diffractive hard scattering*, Summary report of the Working Group on Diffractive Hard Scattering in *Future Physics at HERA* (HERA, 1996).

[15] T. Regge, Nuovo Cim. **14**, 951 (1959).

[16] G. Chew and S. Frautschi, Phys. Rev. Lett. **8**, 41 (1962).

[17] V. N. Gribov, Zh. Eksp. Teor. Fiz. **41**, 667 (1961).

[18] J. C. Collins, D. E. Soper, and G. Sterman, Perturbative Quantum Chromodynamics (1989).

[19] R. G. Newton, Am. Phys. J. **44**, 639 (1976).

[20] R. Feynman, *QED: The Strange Theory of Light and Matter* (Princeton University Press, 1985).

[21] D. Bernard *et al.* (UA4 collab.), Phys. Lett. B **198**, 583 (1987).

[22] R. Cahn, Z. Phys. C **15**, 253 (1982).

[23] P. Collins, *An Introduction to Regge Theory and High Energy Physics* (Cambridge University Press, Cambridge, 1977).

[24] I. Y. Pomeranchuk, Sov. Phys. JETP **7**, 499 (1958).

[25] A. Sommerfeld, *Partial Differential Equations In Physics* (Academic Press., 1949).

[26] F. Carlson, Ph.D. thesis, Upsala (1914).

[27] R. Forshaw, *Quantum Chromodynamics and the Pomeron* (Cambridge University Press, The Pitt Building, Trumpington Street, Cambridge CB2 1RP, UK, 1997).

[28] R. Peierls and L. Foldy, Phys. Rev. **130**, 1585 (1963).

[29] L. Łukaszuk and B. Nicolescu, Lett. Nuovo Cim. **8**, 405 (1973).

[30] D. Joynson, E. Leader, C. Lopez, and B. Nicolescu, Nuovo Cim. **30A**, 345 (1975).

[31] V. N. Gribov, V. D. Mur, I. Y. Kobzarev, L. B. Okun, and V. S. Popov, Sov. J. Nucl. Phys. **12**, 699 (1971).

[32] T. Chou and C. Yang, Phys. Lett. B **128**, 457 (1983).

[33] T. Chou and C. Yang, Phys. Lett. B **244**, 113 (1990).

[34] J. Soffer, C. Bourrely, and T. T. Wu, Phys. Rev. D **19**, 3249 (1979).

[35] J. Soffer, C. Bourrely, and T. T. Wu, Nucl. Phys. B **247**, 15 (1984).

[36] J. Soffer, C. Bourrely, and T. T. Wu, Z. Phys. C **37**, 369 (1988).

[37] A. Donnachie and P. V. Landshoff, Phys. Lett. B **123**, 345 (1983).

[38] A. Donnachie and P. V. Landshoff, Nucl. Phys. B **231**, 189 (1984).

[39] A. Donnachie and P. V. Landshoff, Nucl. Phys. B **244**, 322 (1984).

[40] T. T. Wu and C. Yang, Phys. Rev. **137**, 708 (1965).

[41] N. Byers and C. Yang, Phys. Rev. **142**, 976 (1966).

[42] T. Chou and C. Yang, Phys. Rev. Lett. **20**, 1213 (1968).

[43] T. Chou and C. Yang, Phys. Rev. Lett. **25**, 1072 (1970).

[44] T. Chou and C. Yang, Phys. Rev. D **19**, 3268 (1979).

[45] J. Soffer, C. Bourrely, and T. T. Wu, Phys. Lett. B **252**, 287 (1990).

[46] H. Cheng and T. T. Wu, Phys. Rev. **182**, 1852, 1868, 1873 (1969).

[47] H. Cheng and T. T. Wu, Phys. Rev. Lett. **24**, 1456 (1970).

[48] H. Cheng and T. T. Wu, Phys. Rev. D **1**, 1069, 1083 (1970).

[49] P. V. Landshoff and J. C. Polkinghorne, Nucl. Phys. B **28**, 225 (1971).

[50] U. Amaldi *et al.*, Phys. Lett. B **44**, 112 (1973).

[51] U. Amaldi, M. Jacob, and G. Matthiae, Ann. Rev. Nucl. Sci. **26**, 385 (1976).

[52] E. Predazzi, Riv. Nuovo Cim. **6**, 217 (1976).

[53] M. Bozzo *et al.* (UA4 collab.), Phys. Lett. B **136**, 217 (1984).

[54] M. Bozzo *et al.* (UA4 collab.), Phys. Lett. B **147**, 392 (1984).

[55] G. J. Alner *et al.* (UA5 collab.), Z. Phys. C **32**, 133 (1986).

[56] N. A. Amos *et al.* (E710 collab.), Phys. Lett. B **243**, 158 (1990).

[57] N. A. Amos *et al.* (E710 collab.), Phys. Lett. B **247**, 127 (1990).

[58] F. Abe *et al.* (CDF collab.), Phys. Rev. D **50**, 5518; 5535; 5550 (1994).

[59] R. M. Baltrusaitis *et al.*, Phys. Rev. Lett. **52**, 1380 (1984).

[60] M. Honda *et al.*, Phys. Rev. Lett. **70**, 525 (1993).

[61] H. A. Bethe, Ann. Phys. **3**, 190 (1958).

[62] G. West and Y. Yennie, Phys. Rev. **172**, 1413 (1968).

[63] N. H. Buttimore, E. Gotsman, and E. Leader, Phys. Rev. D **18**, 694 (1978).

[64] A. Breakstone *et al.*, Nucl. Phys. B **248**, 253 (1984).

[65] G. Barbiellini, Phys. Lett. B **39**, 663 (1972).

[66] M. Giffon, R. S. Nahabetian, and E. Predazzi, Z. Phys. C **36**, 67 (1987).

[67] M. Giffon, R. S. Nahabetian, and E. Predazzi, Phys. Lett. B **205**, 363 (1988).

[68] M. Harrison, S. Peggs, and T. Roser, Ann. Rev. Nucl. Part. Sci. **52**, 425 (202).

[69] K. Ackermann *et al.* (STAR collab.), Nucl. Instrum. Meth. A **499**, 624 (2003).

[70] S. Bültmann *et al.* (pp2pp collab.), Nucl. Instrum. Meth. A **535**, 415 (2004).

[71] STAR collab., STAR Collaboration web page.

[72] R. Yarema *et. al.*, *A Beginners Guide to the SVXIIE* (Fermilab TM–1892, 1995).

[73] C. J. S. Damerell, in *Proceedings of the 1995 SLAC Summer Institute on Particle Physics*, SLAC-R-494 (SLAC, 1995).

[74] W. R. Leo, *Techniques for Nuclear and Particle Physics Experiments* (Springer-Verlag, 1987).

[75] H. Wiedemann, *Particle Accelerator Physics I: Basic Principles and Linear Beam Dynamics* (Springer-Verlag, 1999).

[76] A. Drees, *Analysis of Vernier Scans during the PP2PP run9 (pp at 100 GeV/beam)*, Brookhaven National Laboratory STAR Collaboration Technical Note (unpublished) (2011).

[77] D. Plyku, *Spin Dependence In Polarized Proton-Proton Elastic Scattering At RHIC*, Ph.D. thesis, Old Dominion University (2013).

[78] I. Alekseev *et al.*, *Brookhaven National Laboratory (BNL) Collider Accelerator Department Report No. XXX, Run09 pC Polarimeter Analysis*, Brookhaven National Laboratory STAR Collaboration Technical Note (unpublished) (20XX).

[79] S. Bültmann, *Roman pot positions during Run09 spreadsheet*, Brookhaven National Laboratory STAR Collaboration Technical Note (unpublished) (2009).

[80] S. Tepikian, Brookhaven National Laboratory STAR Collaboration Technical Note (unpublished) (2010).

[81] I. Alekseev, L. Koroleva, B. Morozov, and D. Svirida, "*Roman pots alignment at run 2009*," (2011), Brookhaven National Laboratory STAR Collaboration Technical Note (unpublished).

[82] D. Plyku, *Technical Note on Survey Alignment of the Silicon Strip Detectors used in the Roman Pots at STAR during RHIC 2009 Run*, Brookhaven National Laboratory STAR Collaboration Technical Note (unpublished) (2012).

[83] K. Yip, *Analysis Note for the A_N and r_5 using 2009 pp2pp data*, Brookhaven National Laboratory STAR Collaboration Technical Note (unpublished) (2010).

[84] T. Obrebski, *Characterization of Silicon Microstrip Detectors in PP2PP experiment at RHIC*, Engineering Thesis in Technical Physics, Warsaw University of Technology (2010).

[85] (Geant4 collab.), GEANT4 simulation toolkit.

[86] B. Z. Kopeliovich, I. K. Potashnikova, B. Povh, and E. Predazzi, Phys. Rev. D **63** (2001).

[87] M. M. Block, Nuc. Phys. B (Proc. Suppl.) **71**, 378 (1999).

[88] V. V. Ezhela *et al.*, Phys. Rev. D **65** (2002).

[89] J. Soffer, C. Bourrely, and T. T. Wu, Eur. J. Phys. C **28**, 97 (2003).

VITA

Ivan Koralt
Department of Physics
Old Dominion University
Norfolk, VA 23529

Education:

- Ph.D., Department of Physics, Old Dominion University, Norfolk, VA, December 2013
- M.Sc., Department of Physics, Old Dominion University, Norfolk, VA, May 2007
- B.Sc., Faculty of Physics, University of Belgrade, Belgrade, Republic of Serbia, March 2005

Typeset using LaTeX.